NATIONAL CENTRE
FOR NUCLEAR RESEARCH

DOCTORAL THESIS

Radiological characterization of low- and intermediate level (LL/IL) radioactive waste

Author:
Patrycja DYRCZ

Supervisors:
Łukasz ŚWIDERSKI, NCBJ
Matteo MAGISTRIS, CERN

A thesis submitted in fulfillment of the requirements
for the degree of Doctor of Philosophy

in the

Department Radiation Detectors and Plasma Diagnostics Division (TJ3)

March 7, 2022

Declaration of Authorship

I, Patrycja DYRCZ, declare that this thesis titled, "Radiological characterization of low- and intermediate level (LL/IL) radioactive waste" and the work presented in it are my own.
I confirm that:

- This work was done wholly or mainly while in candidature for a research degree at the National Centre for Nuclear Research.
- Where any part of this thesis has previously been submitted for a degree or any other qualification at the National Centre for Nuclear Research or any other institution, this has been clearly stated.
- Where I have consulted the published work of others, this is always clearly attributed.
- Where I have quoted from the work of others, the source is always given. With the exception of such quotations, this thesis is entirely my own work.
- I have acknowledged all main sources of help.
- Where the thesis is based on work done by myself jointly with others, I have made clear exactly what was done by others and what I have contributed myself.

Signed:
_____

Date:
_____

NATIONAL CENTRE FOR NUCLEAR RESEARCH

Abstract

Radiological characterization of low-and intermediate level (LL/IL) radioactive waste

Patrycja DYRCZ

In the framework of maintenance, upgrades and dismantling activities of particle accelerators, a number of activated components are removed from the accelerator complex and require radiological characterization before their disposal as radioactive waste. This thesis introduces a methodology for the radiological characterization of radioactive waste produced in the particle accelerators at the European Organization for Nuclear Research (CERN). In particular, we focus on the characterization of Low level/Intermediate level (LL/IL) metallic waste, in view of its disposal after melting.

The aim of the characterization is the identification of the radionuclides produced inside the waste packages, along with the evaluation of their activity concentration. The characterization relies on extensive analytical calculations, which allow us to predict what radionuclides can be produced due to interactions between the incident particles and the accelerator structures and their surroundings. The predicted radionuclides can be classified as Easy-to-measure (ETM), Difficult-to-measure (DTM) or Impossible-to-measure (ITM). The ETM radionuclide activity concentrations are evaluated via gamma spectrometry measurements of the waste items, the activities of DTM radionuclides by experimental scaling factors (using representative samples of the waste) and the activities of ITM radionuclides by analytical scaling factors.

The radiological characterization presents several challenges. Items of waste which are candidates for elimination as LL/IL have dose-rate levels higher than 100 μSv/h, a radiation level which is challenging in terms of radiation protection during the phases of handling and measurement. In addition, these waste items often exhibit highly heterogeneous activity distributions. Hence, it can be difficult to obtain accurate results from *In-Toto* gamma spectrometry, especially if the analyses are performed under the simplistic assumption that the activity distribution is uniform. In order to overcome such difficulties, we propose a novel Non-Destructive Assay (NDA) technique that estimates the uncertainties introduced by this assumption. We use geometry model optimization to quantify the expected activity concentration values to the best of our knowledge using multi-line and multi-count consistency constraints. The thesis also describes the quantification of activity concentration levels of DTM and ITM radionuclides. The scaling factor formalism relies on an existing activity

correlation established between the Key Nuclide (KN) and DTM radionuclides from a set of samples representing the waste population. Therefore, the Difficult-to-measure radionuclides activity concentrations of a given waste item or package belonging to this population can be evaluated using the geometric mean scaling factor value from the sample's log normal distribution. The entire process to establish the scaling factors for the DTM radionuclides may be long and challenging, in order to collect a sufficient number of samples that represent the waste population. In the case of Impossible-to-measure radionuclides, we apply the analytical Correlation factor (CF) from the analytical activation calculations.

In addition, we propose a new methodology that predicts the total beta-gamma specific activity based on the average dose rate measurements for LL/IL waste produced at CERN in an operationally efficient manner for waste packages production purposes. The methodology is validated using gamma spectroscopy techniques with a geometry model optimization formalism.

The thesis describes the characterization methodology in full details, along with practical examples and benchmarks. At the moment of writing, such methodology has already been approved by French National Agency for Radioactive Waste Management (ANDRA) and it is being applied to the first batch of LL/IL waste to be disposed of. We expect that this methodology can be successfully applied to radioactive waste produced in other particle accelerators outside CERN.

NATIONAL CENTRE FOR NUCLEAR RESEARCH

Streszczenie

Radiological characterization of low-and intermediate level (LL/IL) radioactive waste

Patrycja DYRCZ

W ramach prac konserwacyjnych, modernizacyjnych czy też demontażowych akceleratora cząstek, usuwane są różnego rodzaju komponenty, między innymi te, które zostały aktywowane. W przypadku aktywowanych materiałów wymagane jest przeprowadzenie charakterystyki radiologicznej pod kątem ich eliminacji jako odpadów promieniotwórczych. W niniejszej pracy przedstawiono metodologię charakterystyki radiologicznej odpadów promieniotwórczych wytwarzanych w akceleratorach cząstek w Europejskiej Organizacji Badań Jądrowych (CERN). W szczególności koncentrując się na charakterystyce odpadów metalicznych nisko i średnio aktywnych (LL/IL) przeznaczonych do eliminacji po uprzednim ich stopieniu.

Celem charakteryzacji jest identyfikacja radionuklidów oraz ocena stężenia ich aktywności w danych odpadach. Charakteryzacja ta opiera się na szeroko zakrojonych obliczeniach analitycznych, które pozwalają przewidzieć, jakie radionuklidy mogą powstać w wyniku interakcji między zderzającymi się cząstkami a wnętrzem akceleratora, jak również jego otoczeniem. Spodziewane radionuklidy można sklasyfikować jako tzw. łatwo mierzalne (Easy-to-measure, ETM), trudno mierzalne (Difficult-to-measure, DTM) oraz niemożliwe do zmierzenia (Impossible-to-measure, ITM). Poziom aktywności radionuklidów ETM ocenia się na podstawie wykonanych pomiarów spektrometrycznych promiemiowania gamma danego odpadu radioaktywnego. W przypadku radionuklidów DTM, ich poziom aktywności szacuje się za pomocą doświadczalnej techniki tzw. "scaling factor". Natomiast, poziom aktywności ITM radionuklidów jest oceniany za pomocą analitycznych współczynników skalowania "scaling factor".

Charakterystyka radiologiczna niesie za sobą wiele wyzwań. Odpady, które kwalifikują się do eliminacji jako LL/IL charakteryzują się poziomem mocy dawki przewyższajacym 100 μSv/h. Taki poziom promieniowania stanowi wyzwanie dla ochrony radiologicznej w trakcie postępowania z odpadami, np. podczas wykonywania pomiarów. Ponadto, odpady te cechują się niejednorodnym rozkładem aktywności. W związku z tym uzyskanie dokładnych wyników z *In-Toto* spektrometrii promieniowania gamma może być trudne, zwłaszcza jeśli analizy są przeprowadzane przy założeniu, że rozkład aktywności jest jednorodny. Aby przezwyciężyć takie trudności, proponujemy nowatorską technikę, polegającą na nieniszczącym oznaczeniu zawartości aktywości radionuklidu (Non-Destructive Assay, NDA). Zadaniem

tej techniki jest oszacowanie niepewności wynikających z założenia o jedorodnym rozkładzie aktywności w odpadach. Technika ta wykorzystuje optymalizację modelu geometrycznego, tak aby określić ilościowo oczekiwane wartości stężenia aktywności zgodnie z dostępnymi informacjami na temat danego odpadu, polegając na spojności emisji wielu promieni gamma (multi-line) oraz pomiarów wykonanych wielokrotnie (multi-count). W pracy przedstawiono również sposób określnia ilościowego stężenia aktywności radionuklidów DTM oraz ITM. Formalizm "scaling factor" zakłada, że istnieje korelacja aktywności między głównym emiterem gamma (Key Nuclide, KN) a trudno mierzalnym (DTM) bazując na zebranych próbkach, które reprezentują populację odpadów. Zatem poziom aktywności radionuklidów DTM danego odpadu należącego do populacji można oszacować za pomocą wartości "scaling factor", a dokładniej średniej geometrycznej rozkładu logarytmicznie normalnego. Proces wyznaczenia "scaling factors" dla radionuklidów DTM może być długi i trudny, ze względu na konieczność zebrania wystarczającej liczby próbek reprezentujących populację odpadów LL/IL. W przypadku radionuklidów niemożliwych do zmierzenia (ITM) stosuje się współczynnik analitycznej korelacji (Correlation factor, CF) uzyskanej dzięki obliczeniom analitycznym przeprowadzonych dla aktywacji radioizotopów w zespole akceleratorów cząstek.

Ponadto w tej dysertacji przedstawiono nową metodykę, która ma służyć oszacowaniu całkowitej aktywność właściwej beta-gamma emitrów w oparciu o uśrednione pomiary mocy dawki dla odpadów LL/IL wytwarzanych w CERN w sposób sprawny operacyjnie w trakcie formowania opakowań odpadowych. Metodologia ta jest weryfikowana za pomocą technik spektroskopii gamma z formalizmem optymalizacji modelu geometrycznego.

Praca ta opisuje szczegółowo metodologię charakteryzacji, wraz z praktycznymi przykładami oraz analizami porównawczymi. W trakcie realizowania niniejszej pracy, opisana powyżej metodologia została zatwierdzona przez Krajową Agencję Gospodarki Odpadami Promieniotwórczymi (French National Agency for Radioactive Waste Management, ANDRA). Przedstawioną metodologię zastosowano dla pierwszej partii odpadów LL/IL przeznaczonych do eliminacji. Dodatkowo, uważa się, że tę metodologię można z powodzeniem zastosować do odpadów promieniotwórczych wytwarzanych w innych akceleratorach cząstek poza CERN.

Acknowledgements

I would like to express my deep gratitude to my supervisors Dr. Matteo Magistris (CERN) and Dr. Łukasz Świderski (NCBJ) for the guidance and continuous encouragement through out my studies. Their advice has always been precise and useful.
My thanks also go to Dr. Nabil Menaa (CERN) for his guidance in the radiological analyses, which benefited the quality of the thesis.
Concerning the MAST pilot elimination project at CERN, I would like to acknowledge the continuous support and stimulating discussions with Luca Bruno, Renaud Charousset, Gerald Dumont, Matteo Magistris, Nabil Menna, and Maeva Rimlinger.
I would like to thank all my present and previous colleagues from my section at CERN (HSE-RP-CS) for their support over the last $3^1/_2$ years. Especially, Thomas Frosio, Biagio Zaffora and Richard Harbron.
Last but not least, I would like to thank my family and fiends for their constant support, believing in me, and pushing me to become a better scientist and person.

Patrycja Dyrcz

Contents

List of Figures

List of Tables

List of Acronyms

AD Antiproton decelerator.

ALARA As Low As Reasonably Achievable.

ALICE A Large Ion Collider Experiment.

ANDRA French National Agency for Radioactive Waste Management.

ATLAS A Toroidal LHC ApparatuS.

AVG-DR Average Dose Rate.

BLM Beam Loss Monitoring.

BME Boltzmann Master Equation.

CERN European Organization for Nuclear Research.

CF Correlation factor.

CLT Central Limit Theorem.

CMS Compact Muon Solenoid.

DA Destructive Assay.

DPM Dual Parton Model.

DTM Difficult-to-measure.

ECDF Empirical Cumulative Distribution Function.

ETM Easy-to-measure.

EW Exempt waste.

FMA Faible et Moyenne Activité.

FOM Figure of Merit.

FWHM Full Width Half Maximum.

GINC Generalized Intra-Nuclear Cascade.

GURU Geometry Uncertainty Reduction Utility.

HL-LHC High-Luminosity LHC.

HPGe High Purity Germanium.

IAEA International Atomic Energy Agency.

ICR Input Count Rate.

IL Intermediate level.

IRAS Indice Radiologique d'Acceptabilité en Stockage.

ISO International Organization for Standardization.

ISOCS In Situ Object Counting System.

ISOLDE Isotope mass Separator On-Line facility.

ISR Intersecting Storage Ring.

ITM Impossible-to-measure.

IUE ISOCS Uncertainty Estimator.

KN Key Nuclide.

LEIR Low Energy Ion Ring.

LHC Large Hadron Collider.

LHCb Large Hadron Collider beauty experiment.

LHCf Large Hadron Collider forward experiment.

LL Low level.

LSC Liquid Scintillation Counter.

MAST Melting of Activated STeel.

MCA Multi-Channel Analyzer.

MDA Minimum Detectable Activity.

MoEDAL Monopole and Exotics Detector at the LHC.

NDA Non-Destructive Assay.

n–TOF Neutron Time-of-Flight.

PDF Probability Density Function.

PEANUT PreEquilibrium Approach to Nuclear Thermalization.

PS Proton Synchrotron.

PS Booster Proton Synchrotron Booster.

ROI Regions Of Interests.

RWTCS Radioactive Waste Treatment Centre and Storage.

SE Coating threshold (Seuil d'enrobage).

SF Scaling factor.

SHERPA SHEaR Process Assessment.

SPS Super Proton Synchrotron.

TFA Très Faiblement Actifs.

TOTEM TOTal Elastic and diffractive cross section Measurement experiment.

VLL Very low level.

List of Symbols

L_C Critical Limit.

L_D Detection Limit.

Introduction

The operation of high-energy particle accelerators like the ones at the European Organization for Nuclear Research (CERN) leads to the unavoidable production of radioactive materials. The production of radioactive waste is caused by the interaction of particles with matter, which can induce radioactivity in the accelerator components.

If the activated material cannot be reused or recycled, it needs to be disposed of in dedicated final repositories. The radioactive waste produced at CERN is disposed of in France or Switzerland in accordance with the existing elimination pathways following the tripartite agreement between CERN, France and Switzerland (Host States). Prior to the disposal of radioactive waste, one needs to perform the radiological characterization in order to verify the waste acceptability in the final repositories. The radiological characterization process consists of a series of radiation measurements, complemented by analytical calculations, which determine the radionuclide inventory and quantify the radionuclide activities and radiotoxicity inside the waste item (or package).

The objective of this thesis is the development of a new characterization process for Low level/Intermediate level (LL/IL) waste produced at CERN in view of its elimination at the French national repository managed by the French National Agency for Radioactive Waste Management (ANDRA[1]). In particular, we focus on the radiological characterization of metallic waste from particle accelerators for disposal after melting. Melting of metallic radioactive waste offers a number of advantages: volume reduction, immobilization of contamination (if present) and radioactivity homogenization. The radiological characterization of the melted waste is relatively simple, as it can be based on sampling techniques. One sample collected during melting is then representative of the entire batch of metal being melted. However, prior to the melting process (shipping to the melting facility), the radiological characterization that is performed at CERN on the primary metallic waste is associated with a number of challenges.

The major outcome of the present work is the development of a radiological characterization methodology of LL/IL waste produced at CERN. As part of this, we need to address several challenges. One is the radiological characterization of massive metallic waste, that includes items >1 ton. These massive items may exhibit self-absorption and heterogeneous activity concentrations within the waste, which requires developing an *In-Toto* gamma spectrometry with

[1] Agence Nationale pour la gestion des Déchets RAdioactif

multiple counts. The dose rate level above 100 μSv/h at contact is also challenging for radiation protection aspects when handling and processing the waste. The high dose rate levels also present difficulties for the design of the counting geometry, which minimises the dead time during the acquisition in order to meet the Minimum Detectable Activity (MDA) requirements. The determination of the geometry modelling parameters in the spectrometry analysis can be difficult, because they are not well known and certain geometries are complex to model. The waste may have a heterogeneous activity distribution due to activation mechanisms, self-attenuation or density variation. In addition, our objective is to establish a simple, operational and standard methodology. At the same time, we need to quantify the uncertainties associated with the proposed approach. We also need to validate the analytical scaling factors for LL/IL waste, that result from hundreds of activation scenarios that consist of a wide range of irradiation, cooling times and beam energies. The sampling process can be long and challenging, in order to collect representative samples from the waste population. Within this thesis, we have to check whether the scaling factors for Very low level (VLL) are comparable with the LL/IL values, knowing we currently collected a limited number of samples from the LL/IL waste. Additionally, the activity distribution heterogeneity of the waste adds another level of challenges for the sampling process.

This thesis consists of six chapters. Chapter 1 describes the mechanisms that lead to the production of activated material in CERN's accelerator complex. In particular, the mathematical principle of induced radioactivity is introduced.

Chapter 2 gives a general overview of the characterization process steps that are in accordance with the International Atomic Energy Agency (IAEA) guidelines. The chapter ends with a description of the classes of waste currently treated at CERN, with emphasis on LL/IL radioactive waste.

Chapter 3 describes the concepts needed to estimate the radionuclide inventory, quantify their activities and test their correlation. In this Chapter, we present the dedicated methods that are based on both the analytical calculations and experimental data. In particular, the radionuclide inventory is established based on extensive Monte Carlo and analytical calculations. According to the IAEA, the radionuclide within the radionuclide inventory can be classified as Easy-to-measure (ETM), Difficult-to-measure (DTM) and Impossible-to-measure (ITM). Evaluation of gamma emitter activities via gamma spectrometry is an essential step in the characterization of LL/IL waste. The gamma spectrometry measurements are dedicated to quantifying the activity of gamma emitting (ETM) radionuclides. In order to estimate the activity of DTM radionuclides, first destructive techniques are applied on the collected samples from the waste population. Then, one applies the Scaling factor (SF) method relying on the correlation between radionuclide activity values, namely the correlation between DTM radionuclides and the dominant ETM (referred to as Key Nuclide, KN). The experimental SF for DTM radionuclides is based on the statistical analysis of over several hundred samples of radioactive waste at CERN. For ITM radionuclides with activity levels that are systematically below the detection threshold,

or for which it was not possible to establish an experimental correlation with their respective KN, the SF is calculated analytically. At the end of this Chapter, the radiological characterization process developed at CERN for LL/IL waste is described.

Chapter 4 provides an overview of the gamma spectrometry measurement qualification in order to estimate the ETM radionuclide activities. Due to waste geometry and heterogeneous activity distribution, we introduce a novel Non-destructive Assay technique that investigates the uncertainties of the measured activities. In particular, one gives the results that are based on the Figure of Merit (FOM) that rely on the multi-count and multi-line activity consistencies.

Finally, Chapter 5 presents the predicted radionuclide inventory and the corresponding SFs needed to estimate the activity of DTM and ITM radionuclides in the primary metallic waste prior to its elimination. The first part provides the experimental validation of ETM radionuclides, given by the *In-Toto* gamma spectrometry measurements. Subsequently, the validation of the experimental and analytical SFs for DTM and ITM radionuclides is provided respectively. We also show the statistical analysis needed to investigate the distribution of the SFs for pairs of DTM and KN radionuclides. The end of this Chapter demonstrates the application of the developed radiological characterization within this thesis, giving several examples of waste packages prepared for the elimination via melting. It summarizes the estimation of the total beta-gamma activities in the waste package with associated uncertainties. In addition, the qualification of the gamma spectroscopy results are presented in order quantify the impact of assuming uniform activity distribution of the gamma emitters within the waste.

The last Chapter presents the main stages of the design and implementation of the characterization process, in order to radiologically characterize the LL/IL metallic waste produced at CERN.

Chapter 1

The production of radioactive waste at CERN

The European Organization for Nuclear Research (CERN) is a laboratory where "scientists are probing the fundamental structure of the universe". The organization was founded in 1954 and located on the border between Switzerland and France. Currently, CERN has 23 members states. Within the mandate of the organization is the study of the basic constituents of matter,the fundamental particles. For the last 60 years, researchers have been studying the properties of particles by colliding them and then observe their interactions. The generation of radiation is unavoidable when particles collide in high energy particle accelerators like the Large Hadron Collider (LHC). The present thesis focuses on the study of the CERN accelerator complex in terms of the interaction of particles with matter that induces radioactivity in the accelerator structure and its surroundings, thereby producing radioactive waste.

Section 1.1 describes the CERN's accelerator complex. The concept of beam dynamics and loss mechanisms are explained with the typical spectra encountered in CERN's accelerators in Sections 1.2 and 1.3. The general activation formula is given in Section 1.4.

1.1 CERN's accelerator complex

CERN's accelerator complex consists of a large number of powerful machines that accelerate particles. The largest accelerator is the Large Hadron Collider (LHC), which started up in 2008. At present the LHC accelerates particles up to 6.5 TeV per beam.

The task of CERN's accelerator chain is to accelerate particles to increasingly higher energies. Each accelerator in the sequence boosts the energy of a beam of dedicated particles, then injects the beam into the next accelerator in the chain. During the operation of the accelerators, particles interacting with matter might lead to the activation of the machine components. Induced radioactivity is caused by direct interactions of the primary beam (or of a shower of secondary particles) with matter. The induced radioactivity depends on the type of accelerator and its irradiation conditions including location of the beam losses, irradiation and cooling times [87]. Table 1.1 shows the main parameters for CERN's accelerators: the nominal kinetic energy for protons beams, accelerator's length and start-up date [30].

Table 1.1: The accelerator machines at CERN.

Accelerator	Energy/Momentum	Length	Commissioned
Linac 2	50 MeV	30 m	1978
Linac 4	160 MeV	86 m	2016
PS Booster	1.4 GeV	157 m	1972
PS	25 GeV/c	628 m	1959
SPS	450 GeV/c	7 km	1976
LHC	7 TeV	27 km	2008

Figure 1.1[2] presents a schematic view of the accelerator complex at CERN. It shows the facilities at CERN with the type of accelerated particles, the circumference of each accelerator, as well as running experiments.

[2] ©2016-2020 CERN, https://cds.cern.ch/record/2197559, 7 January 2020.

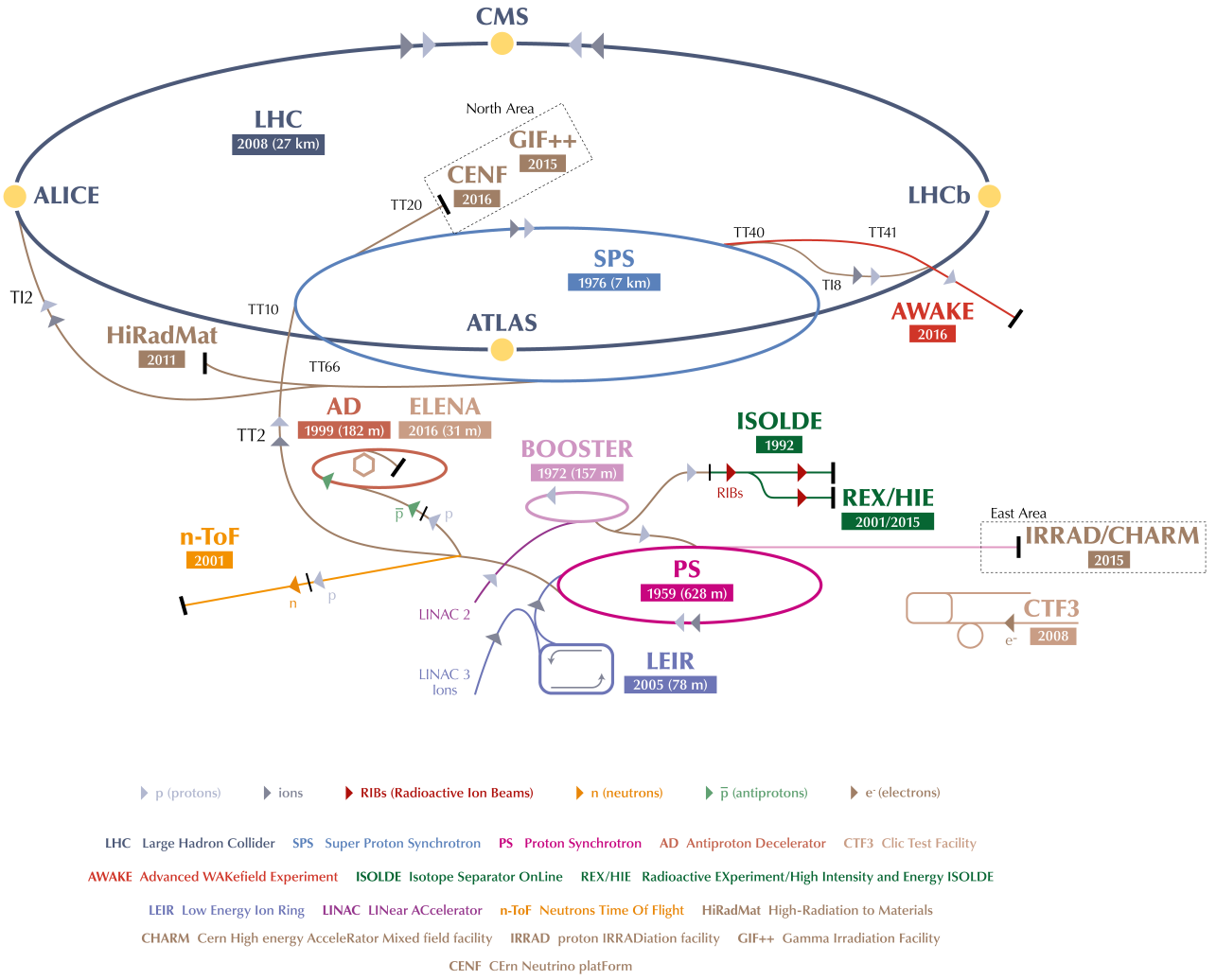

Figure 1.1: The CERN accelerator complex [97].

The accelerating process starts with linear accelerators: protons are accelerated in Linac2, Linac4 and heavy ions in Linac3.

Linac2

Linear accelerator (Linac2), the first accelerator in the chain, which accelerates protons up to 50 MeV. Hydrogen gas is injected into one end of Linac2. Proton sources are obtained by applying an electric field. Due to the stripping of electrons from hydrogen atoms, only protons enter into the accelerator. Protons pass through the 30 m of the Linac2, and gain 5 % in mass. Linac2 was replaced by Linac4 after 40 years of service in 2018.

Linac3

The purpose of the Linac3 is to accelerate heavy ions, such as lead (Linac3 uses $\sim$500 miligrams of lead during a two week operation time). This accelerator was started in 1994. Currently, the Linac3 provides lead ions to the Low Energy Ion Ring (LEIR), which prepares them for entering into the Proton Synchrotron, Super Proton Synchrotron, and finally the LHC. Linac3 is expected to be in use until at least 2022.

Linac4

Linear accelerator 4 (Linac4) is 86 m long and is located 12 m underground. Linac4 is a key element in the High-Luminosity LHC (HL-LHC) project to increase the luminosity of the LHC during the following decades. The new design allows the boosting of negative hydrogen ions H^- to higher energies (160 MeV). The aim of Linac4 is to accelerate particles entering into the Proton Synchrotron Booster. The process in this accelerator is divided into four steps: first acceleration using radio-frequency quadrupoles up to 3 MeV, then to 50 MeV by drift tube linacs. Next by coupled-cavity drift tube linacs to reach the energy of 100 MeV, and finally to 160 MeV using the Pi-mode structure. During injection from Linac4 into the Proton Synchrotron Booster (PS Booster) the ions are stripped from their electrons, leaving only protons. An advantage of the machine is the reduction of beam losses at injection. A section of Linac4 is shown in Figure 1.2[3].

[3] © 2020 CERN, https://home.cern/news/news/accelerators/linac-4-reached-its-energy-goal, 7 January 2020.

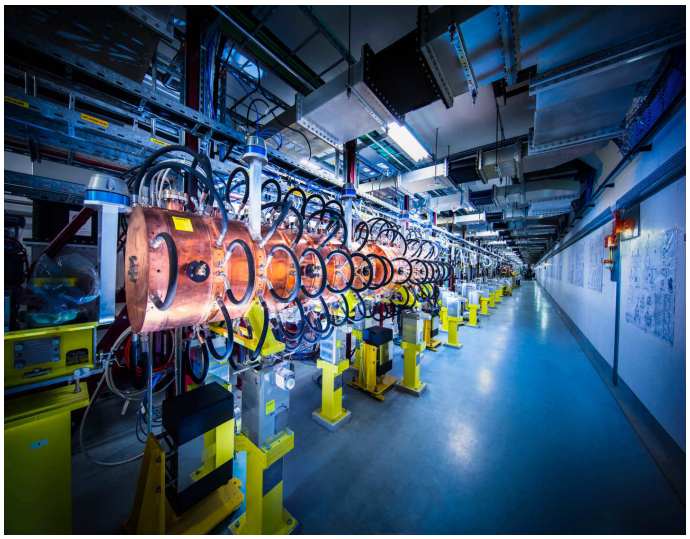

Figure 1.2: The linear accelerator (Linac 4) [30].

Proton Synchrotron Booster, PS Booster

The PS Booster is a machine in the accelerator's chain made up of four superimposed synchrotron rings, which accelerate protons up to the energy 1.4 GeV.

Proton Synchrotron, PS

The Proton Synchrotron (PS), with a circumference of 628 m, is able to accelerate both protons and heavy ions. The PS operates up to 25 GeV and then delivers the protons to the Super Proton Synchrotron, the second largest accelerator in the CERN's complex. Figure 1.3[4] presents the section of PS machine.

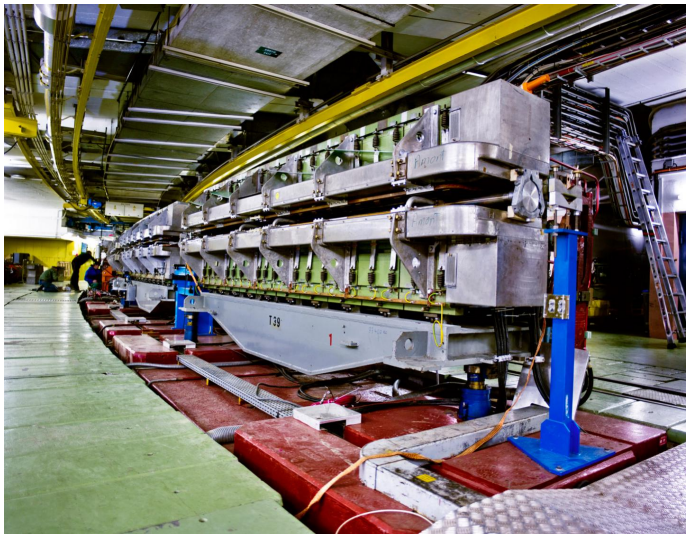

Figure 1.3: View of the PS [30].

[4] ©2012-2020 CERN, https://cds.cern.ch/record/1997189, 7 January 2020.

Super Proton Synchrotron, SPS

This accelerator consists of 1317 electromagnets kept at room temperature, including 744 dipoles to bend the beams around the ring. It is 7 km long. The particles entering from the Proton Synchrotron into the Super Proton Synchrotron (SPS) reach energies up to 450 GeV. The SPS provides beam to LHC and the NA61/SHINE, NA62 and the COMPASS experiments. Additionally, the accelerator is able to handle many different types of particles including sulphur and oxygen nuclei, electrons, positrons, protons and antiprotons [30].

Large Hadron Collider, LHC

The most important parameters for physicists are the beam energy and the number of interesting collisions processes, whose probability varies with collision energy. The Large Hadron Collider is the last element in CERN's accelerator chain. In the LHC, under nominal operating conditions, each proton beam has 2808 bunches, with each bunch containing about 10^{11} protons. The LHC has a circumference of 27 km, located at depth of 100 m, on the border of Switzerland and France. The LHC is the most powerful accelerator ever built, and its design energy per beam is 7 TeV for protons. For lead ions, which have many protons, the maximum collision energy 1150 TeV. The particles are transferred from SPS to the LHC both in a clockwise and an anticlockwise direction. A beam might circulate for more than 10 hours, travelling more than 10 billion kilometres [7].

There are seven experiments installed at the LHC:

1. A Large Ion Collider Experiment (ALICE);
2. A Toroidal LHC ApparatuS (ATLAS);
3. Compact Muon Solenoid (CMS);
4. Large Hadron Collider beauty experiment (LHCb);
5. Large Hadron Collider forward experiment (LHCf);
6. TOTal Elastic and diffractive cross section Measurement experiment (TOTEM);
7. Monopole and Exotics Detector at the LHC (MoEDAL).

The HL-LHC project was announced in 2013. The purpose of HL-LHC is to increase luminosity (which is an important indicator of the performance of an accelerator) by a factor of 10. Higher luminosity allows us to gather more data to observe rare events [3].

The CERN's accelerator complex also includes the Antiproton decelerator (AD), the Neutron Time-of-Flight (n–TOF) and the Isotope mass Separator On-Line facility (ISOLDE).

Antiproton decelerator, AD

The antiproton decelerator was installed in 2000 and provides low-energy antiprotons for studies on antimatter. The protons come from the PS and they are decelerated into a block of metal, generating antiprotons. The objective of the AD is to tame antiprotons with different energies, moving randomly in all directions and turn them into a low-energy beam that can be used to produce antimatter.

Neutron facility, n–TOF

The neutron time-of-flight facility was commissioned in 2001. To produce neutrons, a pulsed beam of protons with a momentum of 20 GeV/c from the PS hits a lead spallation target. Every proton yields about 300 neutrons. The n–TOF is a pulsed neutron source coupled to a 200 m flight path designed to study neutron-nucleus interactions for neutron kinetic energies ranging from a few meV to several GeV.

The Isotope mass separator on line device, ISOLDE

The aim of the ISOLDE facility is to produce a large variety of radioactive ion beams for many different experiments in the fields of nuclear and atomic physics, studying the vast territory of atomic nuclei, including the most exotic species [5]. The proton sources is delivered into the ISOLDE by the PS Booster.

1.2 Beam dynamics and beam losses

In this section, the layout and principles of a synchrotron are described, as an example of a typical accelerator. We will use this example to introduce the concepts of beam dynamics and eventually beam losses.

A particle passes through a circular storage ring periodically with high frequency. To keep the particle focused and in a designed, fixed orbit, we have to assemble focusing and bending magnets (dipoles and quadrupoles) [118].

The objective of the accelerating cavities is to increase the particle momentum by using an electric field whose orientation switches in phase with the position of the particle.

As shown in Figure1.4, in a synchrotron, the beam is generally forwarded to the experimental hutch.

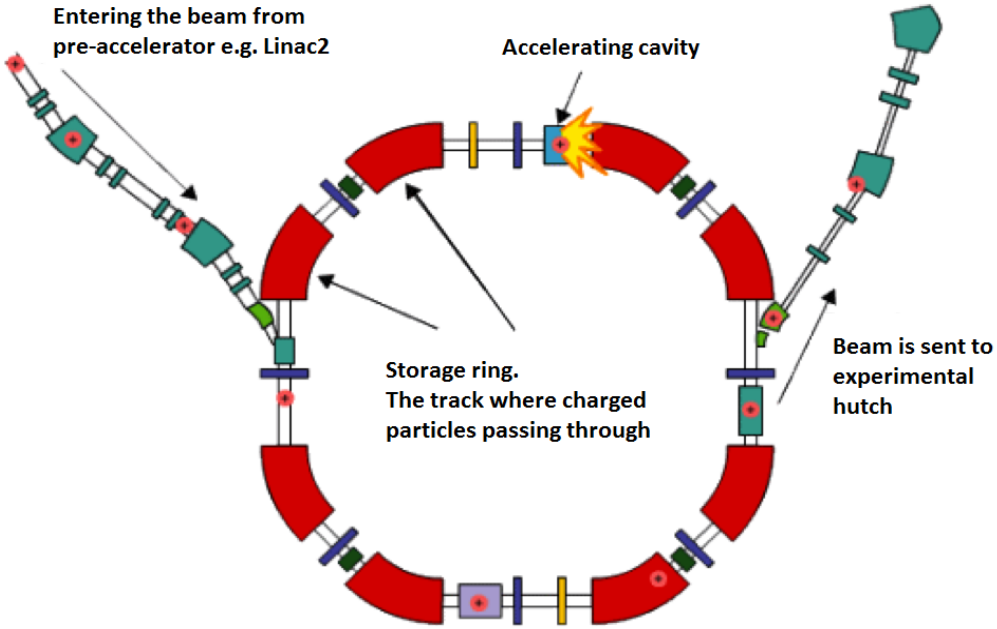

Figure 1.4: Example of a synchrotron layout with a pre-accelerator, a circular storage ring (including accelerator cavities) and an extraction line to an experimental hutch [79].

1.2.1 Beam dynamics

Theoretically, all particles in an accelerator are expected to move on the designed orbit. Bending magnets provide a magnetic field which steers particles along the circular orbit. However, magnets are not perfect, and most particles will have lateral momentum, which can lead to deviation of particles trajectories from the ideal orbit. Figure 1.5 shows the ideal circular orbit (continuous line) and real particle trajectory (dotted line) with its transverse coordinates x and y.

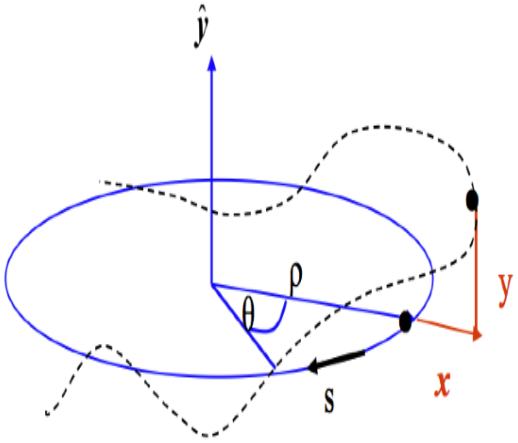

Figure 1.5: Designed orbit (blue line) and real particle trajectory (black dots) with coordinates x and y used in particle beam dynamics; the longitudinal coordinate s moves around the accelerator with the particle considered. [79].

To keep the particles close to the design orbit we have to assemble magnets, which generate a magnetic field. Taking into account the influence of the properties of those magnets, we can describe the equation of motion of a particle by the differential equation given in (1.1) [79][69].

$$x” + Kx = 0. \tag{1.1}$$

The restoring constant K varies around the accelerator and depends on the longitudinal displacement s. K(s) with the lattice period L (where L can be the circumference of the accelerator) will be a periodic function, that is K(s+L)=K(s). Therefore we need to solve the Hill's equation for K, varying as a function of s (see Equation 1.2).

$$\frac{d^2x}{ds^2} + K(s)x(s) = 0 \tag{1.2}$$

The general solutions of Equation 1.2 are shown in Equations 1.3 and 1.4. [120]

$$x = \sqrt{\beta(s)\epsilon}cos[\phi(s) + \phi_0] \tag{1.3}$$

$$x' = \left[\frac{\beta'(s)}{2}\right]\sqrt{\frac{\epsilon}{\beta(s)}}cos[\phi(s) + \phi_0] - \sqrt{\frac{\epsilon}{\beta(s)}}sin[\phi(s) + \phi_0] \tag{1.4}$$

In Equations 1.3 and 1.4, $\phi(s)$ is the phase of the oscillation, ϵ describes the space occupied by the particle in the transverse phase space, β(s) modulates the transverse size of the beam and ϕ_0 represents an integration constant determined by initial conditions.

The trajectory of the particle in phase space turn after turn is an ellipse, as shown in Figure 1.6 where the orientation and the shape is defined by the β(s) function and its derivative $\alpha = \frac{\beta'(s)}{2}$, where the area covered is constant [5].

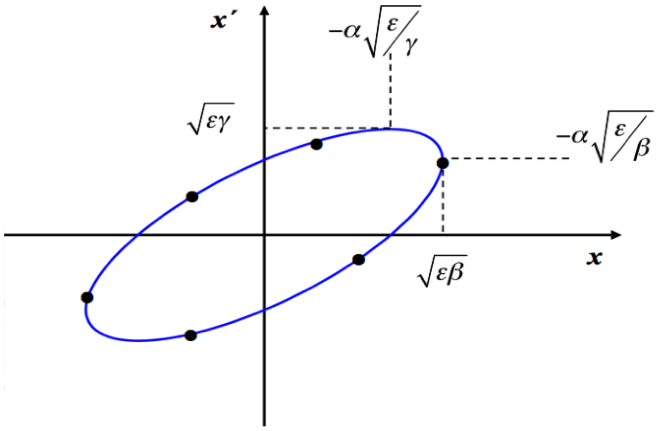

Figure 1.6: The phase space ellipse of particle motion in the x-x' plane [79] [69].

[5] In accelerator physics the area of the ellipse is given by A=$\pi \cdot \epsilon$ [121]

1.2.2 Beam losses

There are many different mechanisms causing beam losses in accelerators, such as for example, beam-residual gas interactions or beam instability [66][101]. Regular beam losses can lead to scattering of protons with protons from the same bunch, as well as with residual gas molecules (H_2, CO, H_2O etc.), which might be present in the beam pipe of an accelerator. There are several possibilities for scattering on residual gas molecules including [84]:

1. Coulomb scattering;
2. Multiple Coulomb scattering;
3. Elastic and inelastic scattering.

Particles perform oscillations around the defined synchronous particle, which always has the same desired phase ϕ_s, and the nominal energy E_s. Usually, the bunch of particles fill a part of the bucket area, which is the region of stable motion. To avoid beam losses, the particle distribution needs to fit into the bucket. Figure 1.7 shows that the bucket area shrinks when the beam begins to accelerate.

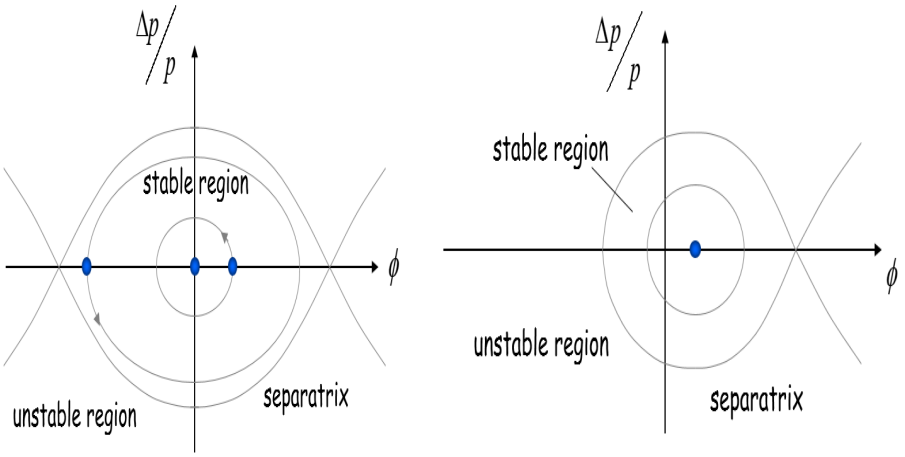

(a) without acceleration. (b) with acceleration.

Figure 1.7: The separatrix separates the phase stable region from the region where particles follow unstable trajectories. The pictures display the phase space for synchrotron oscillation with and without acceleration [111].

The bucket area is called RF acceptance and it is measured in electronvolts. The RF acceptance depends on the ϕ_s, reaching the maximum at ϕ_s= 0 or ϕ_s=π (the beam is not accelerated). Higher RF acceptance can be accomplished by increasing RF voltage. In the particle bunch transfer (bucket-to-bucket) from one accelerator to another some discrepancies can appear in phase if particle beam arrives with smaller momentum. In case of too small RF acceptance, some of the transferred particles will not be accelerated further. As a consequence, those particles will be lost [79].

Based on the design energy limits in CERN's accelerator complex and power limits, the particle loss per machine is shown in Table 1.2 [121] that is approximately inversely proportional to the machine's energy beam.

Table 1.2: Estimated particle losses in CERN's machines for the design power loss of 1 W/m. [121].

Accelerator	Energy/Momentum	Particle loss (s^{-1})
Linac4	160 MeV	$\sim 3.9 \cdot 10^{10}$
PS Booster	1.4 GeV	$\sim 4.5 \cdot 10^{9}$
PS	14 GeV/c	$\sim 4.5 \cdot 10^{8}$
SPS	450 GeV/c	$\sim 1.6 \cdot 10^{7}$
LHC	7 TeV	$\sim 8.9 \cdot 10^{5}$

The Beam Loss Monitoring (BLM) system is one of the essential elements for the protection of LHC accelerator complex at CERN. The purpose of BLM is the prevention of damage to magnets; in addition, the system helps in the identification of loss mechanisms by measuring the beam loss pattern. Detectors are assembled along the accelerators. For instance, Figure 1.8[6] presents the layout of BLM detectors in the SPS facility.

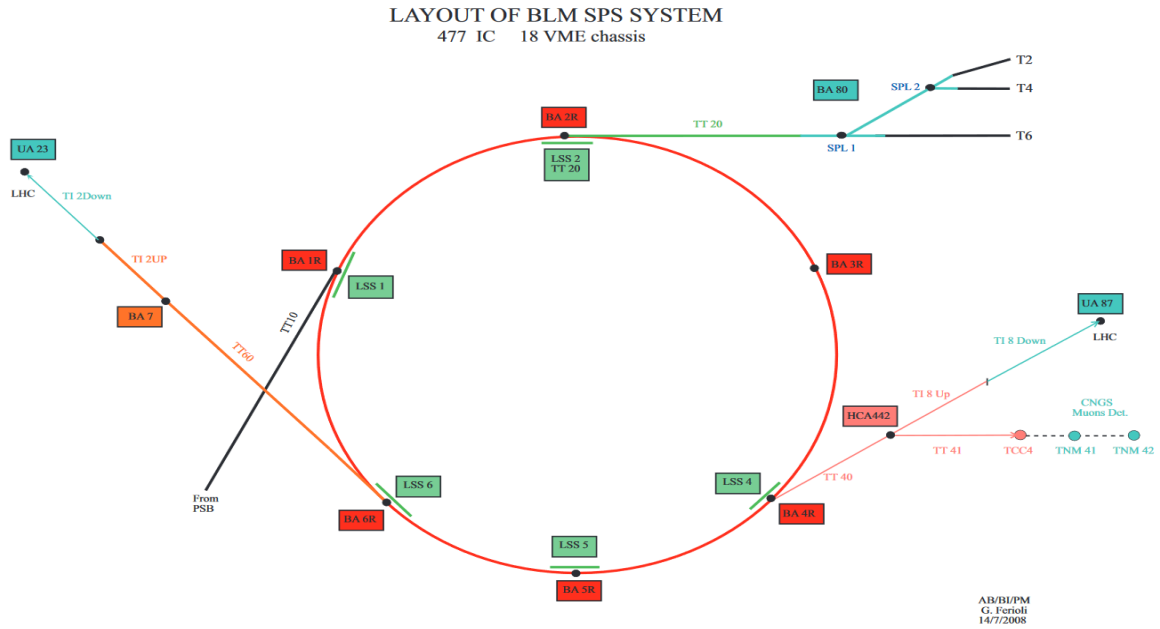

Figure 1.8: SPS, Beam Loss Monitoring (BLM) detectors layout.

[6] SPS beam loss monitoring layout, `https://ab-div-bdi-bl-blm.web.cern.ch/ab-div-bdi-bl-blm/CPS_SPS_BEAM_LOSS/BLM_SPSLAYOUT.pdf`, 7 January 2020.

176 Beam losses in the SPS are measured using ionization chambers filled with nitrogen gas at room
177 temperature. Lost particles pass through a gas, and gas is ionized thereby producing ion electron
178 pairs. The current generated in the electrodes is proportional to the number of lost particles [77].

1.3 Particle spectra

CERN's accelerators are heterogeneous in terms of type and energy of particles that they accelerate or store for collision. Therefore, they are characterized by a wide range of different radiation fields, that can induce radioactivity in the components of the machines.

This section describes electromagnetic and hadron showers, which are the physical processes behind the generation of a radiation field in a high-energy particle accelerator. Primary particles can lose their energy by ionizing the material (accelerator components) or induce new nuclear reactions resulting in the production of secondary particles. Electromagnetic showers are created by electrons, positrons and photons. For electrons and positrons the dominant process at high energies is bremsstrahlung and for photons the dominant process is pair production. Electrons and positrons lose energy when traversing a material. They are decelerated when deflected in the nuclear electric field of atomic nuclei, as a consequence photons are emitted. [119][86][100]

Hadron showers consist of inelastic interactions (strong interactions) of protons, neutrons and heavy ions and the material, producing secondary hadrons. The secondary hadrons interact inelastically to produce a further hadron generation and so forth. When the energy of the primary beam exceeds the pion[7] production threshold (which is around 290 MeV) in nucleon-nucleon interactions, the production of mesons starts to be significant. Mesons decay into photons, electrons and positrons leading to an increase of electromagnetic fraction [58]. A schematic depiction of an hadron shower is shown in Figure 1.9.

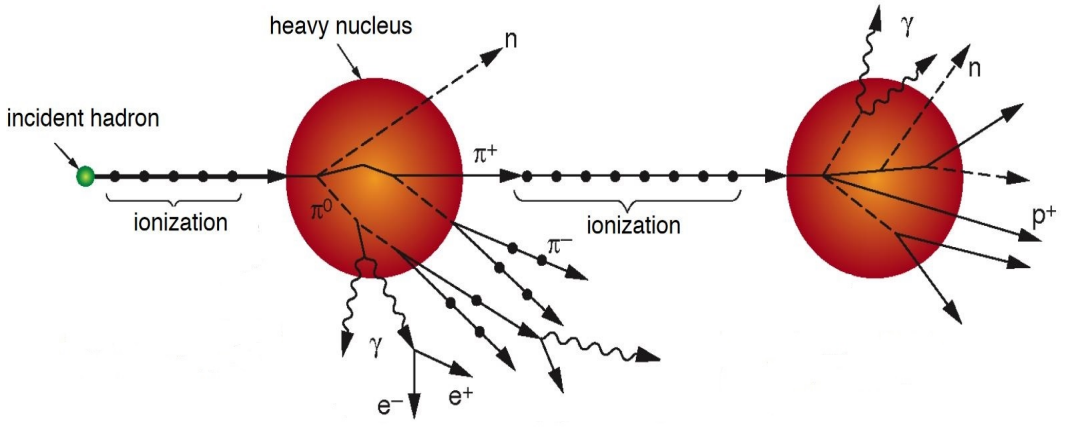

Figure 1.9: Example of hadronic interactions. Components of the nucleus have enough energy to interact with each other and produce, for instance, pions. Particles escaping from the nucleus can interact with another nucleus. The energy carried by hadrons is deposited into electromagnetic (e^+,e^-, γ, π^0) and non-electromagnetic (n, p, π^+, π^-) components [83].

[7] Pions are the lightest hadrons. They are produced with a high concentration in nuclear collisions. Charged pions are unstable, however, they typically re-interact in a material before decaying due to their sufficient mean range. On the other side, neutral pions with a much shorter life-time and range mostly decay into a γ pair [85]

A significant fraction of particles in the hadronic shower are neutrons. The neutrons lose their energy in collision with the material. As a result, neutrons can decay (happens rarely) or get captured by an atomic nucleus, and then gamma rays are emitted [119].

The FLUKA Monte Carlo code [41][39][59] enables the calculation of any particle spectra for a specific area as well as associated beam losses. Studies presented in [47] have shown that for radiological characterization aspects it is not necessary to provide a vast number of spectra. It is more efficient to group them in terms of similar activation mechanism, for a relative number of neutrons, protons and pions (positive and negative) per cm^2 in a function of energy.

ActiWiz [1] is a software that allows the estimation of the radiological inventory for a given radiation environment at CERN. ActiWiz includes simplified activation scenarios depending on the following parameters: energy, localization, material composition, irradiation and cooling time. To assess the activity and radionuclide production ActiWiz uses spectra calculated using the FLUKA Monte Carlo code (a detailed description of ActiWiz is in Section 3.2.2).

As an example, Figures 1.10 and 1.11 show two particle fluence spectra. Proton and pions distribution are very similar in shape and absolute value [115].

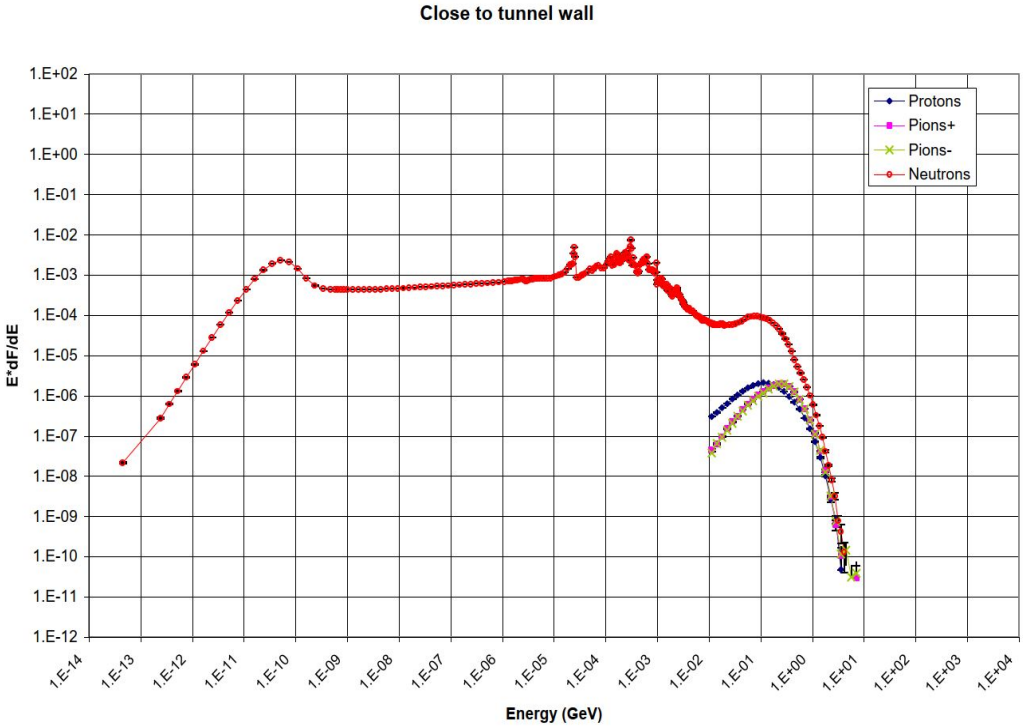

Figure 1.10: Actiwiz. Particle spectra for 400 GeV/c proton beam impacting on an iron cylinder and for a position close to the tunnel wall . (Plots courtesy of H. Vincke and C. Theis, CERN).

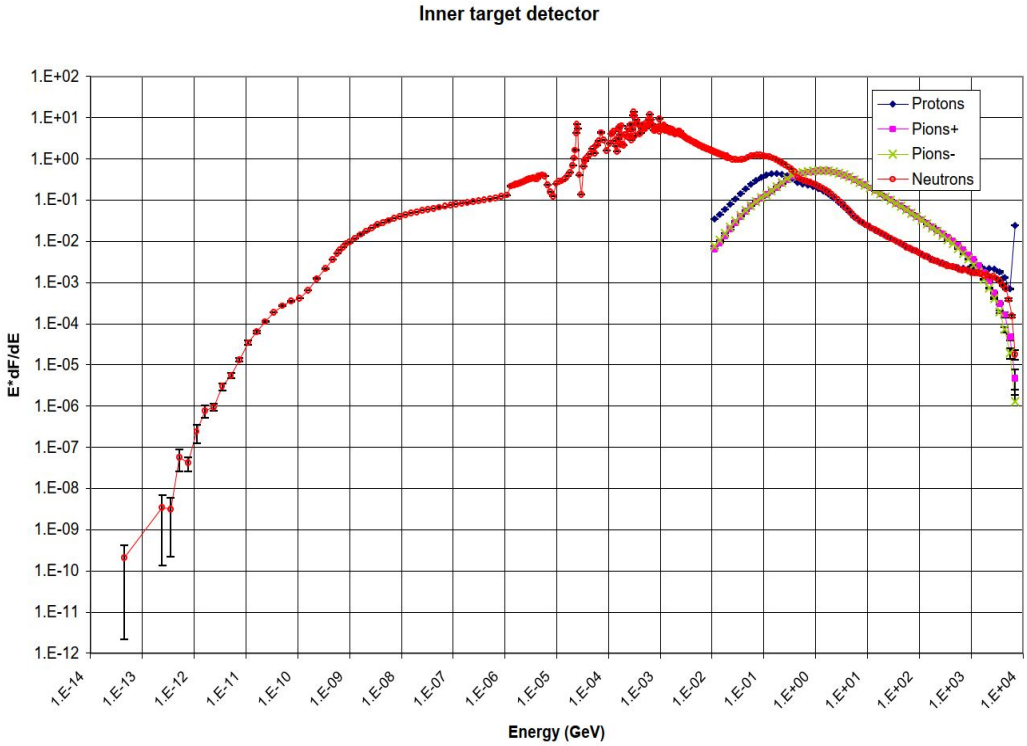

Figure 1.11: Actiwiz. Particle spectra, for 7 TeV/c proton beam impacting on an iron cylinder and for a position at the beam impact point. (Plots courtesy of H. Vincke and C. Theis, CERN).

1.4 Induced radioactivity

This section describes the production of induced radioactivity in particle accelerators. When incident particles with a given flux[8] interact with the nuclei of an accelerator component, neutrons, protons and other nuclear fragments may be emitted. These interactions can lead to converting the struck nucleus to that of a different, radioactive or stable isotope. The probability of producing a particular isotope depends on the composition of the material and the type and energy of the incident particle [110]. Nuclear interactions are characterized quantitatively by a cross-section, σ. The cross-section represents the probability of the interaction between a nucleus and a particle's flux and is defined by Equation 1.5 [35]

$$\sigma = \frac{N}{iN_T x}, \tag{1.5}$$

where σ is a cross-section in square centimetre (cm^2), *N* is the number of interactions in the whole material occurring per unit time (s^{-1}), *i* is total particle current in (s^{-1}), N_T is the number of atoms per cubic centimetre of the material (cm^{-3}), *x* is a material thickness in cm.
If the cross-sections are known, it is possible to determine the activity per gram as a function of the flux Φ received. Assuming that the accelerator's components have been exposed to a flux Φ during an irradiation time t_i , then the number of radioactive atoms *v* created per gram is [9]

$$\begin{aligned} n_v(t_i) &= \Phi \frac{N_A}{A_T} \sigma_{T,v} \int_0^{t_i} exp[-\lambda(t_i - \tau)] d\tau \\ &= \Phi \frac{N_A}{A_T} \sigma_{T,v} \frac{1}{\lambda} (1 - exp[-\lambda t_i]), \end{aligned} \tag{1.6}$$

where N_A is Avogadro's number and A_T is atomic mass of the material.
The cooling time, t_c is the time which has elapsed since the end of the exposure. Therefore n_v will have decreased as shown in Equation 1.7

$$n_v(t_i, t_c) = \Phi \frac{N_A}{A_T} \sigma_{T,v} \frac{1}{\lambda} (1 - exp[-\lambda t_i]) exp[-\lambda t_c]. \tag{1.7}$$

[8] Flux Φ is defined as a number of particles incident component with a surface cm^2 in unit time sec.
[9] We consider particular cross-section $\sigma_{T,v}$, where particle flux strike a material T, v describe the produced isotope.

The time behaviour of the activation process during irradiation time and the subsequent cooling time after the end of the exposure is presented in Figure 1.12.

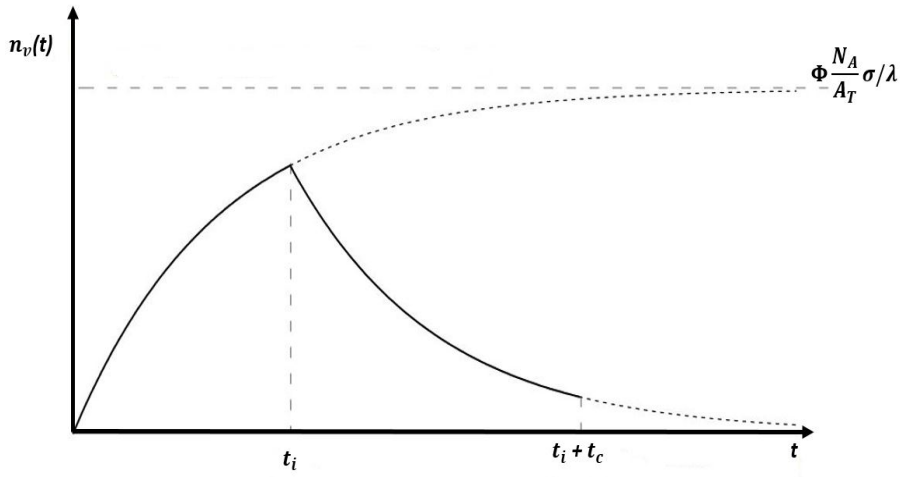

Figure 1.12: Time dependence of the activation and the decay of a radionuclide. Adapted from [29]

To obtain the activity, that is the instantaneous disintegration rate of an isotope, we differentiate the amount of n_v with respect to t_c and change the sign. The formula is the so-called "activation formula":

$$-\frac{dn_v}{dt_c} = \Phi \frac{N_A}{A_T} \sigma_{T,v}(1 - exp[-\lambda t_i])exp[-\lambda t_c]. \tag{1.8}$$

The total specific activity **A** in Bq/g of the material is the sum of the specific activities of the singular isotopes *v* producible.

$$\mathbf{A} = -\sum_v \frac{dn_v}{dt_c} = \Phi \frac{N_A}{A_T} \sum_v \sigma_{T,v}(1 - exp[-\lambda t_i])exp[-\lambda t_c]. \tag{1.9}$$

This is a simplified formula (Equation 1.9) and the complete one for all types of nuclear reactions can be found [62].

Chapter 2

Management of radioactive waste

The production of radioactive waste is unavoidable when operating high-energy particle accelerators like the ones at CERN. The main fraction of radioactive waste produced derives from machine upgrades, maintenance operations and dismantling. At CERN, the radioactive waste management team handles all the phases from the production to the disposal at the radioactive waste repository.

The purpose of this chapter is to present the concept of waste characterization at CERN. Waste characterization is performed prior to disposal to verify the acceptability of the waste in the final repositories. According to the tripartite agreement signed in 2010 by CERN, Switzerland and France [21], radioactive waste generated during the activities of accelerators complex is disposed via the existing elimination pathways at the host state's final repositories.

The data collected in the characterization process should include information concerning the radionuclide inventory and specific activities, physical and chemical properties of the waste. Section 2.1 presents the waste classification in terms of activity content and half-lives of radionuclides with a complementary approach called categorization, which includes different waste processing options. In addition, we describe possible key parameters that might be used in the characterization process. Section 2.2 focuses on the distinction between new and legacy waste. Section 2.3 describes the classes of waste currently treated at CERN. Within the scope of this thesis; low- and intermediate level radioactive waste currently stored at CERN is presented in Section 2.4.

2.1 Classification and categorization of radioactive waste

The radioactive waste produced at CERN's accelerator complex comes in a variety of radionuclide amounts and physical state. Waste can be classified based on its radioactivity level and the half-lives of produced radionuclides within the waste item according to the recommendations of International Atomic Energy Agency (IAEA). Figure 2.1 shows a conceptual scheme of the waste classification.

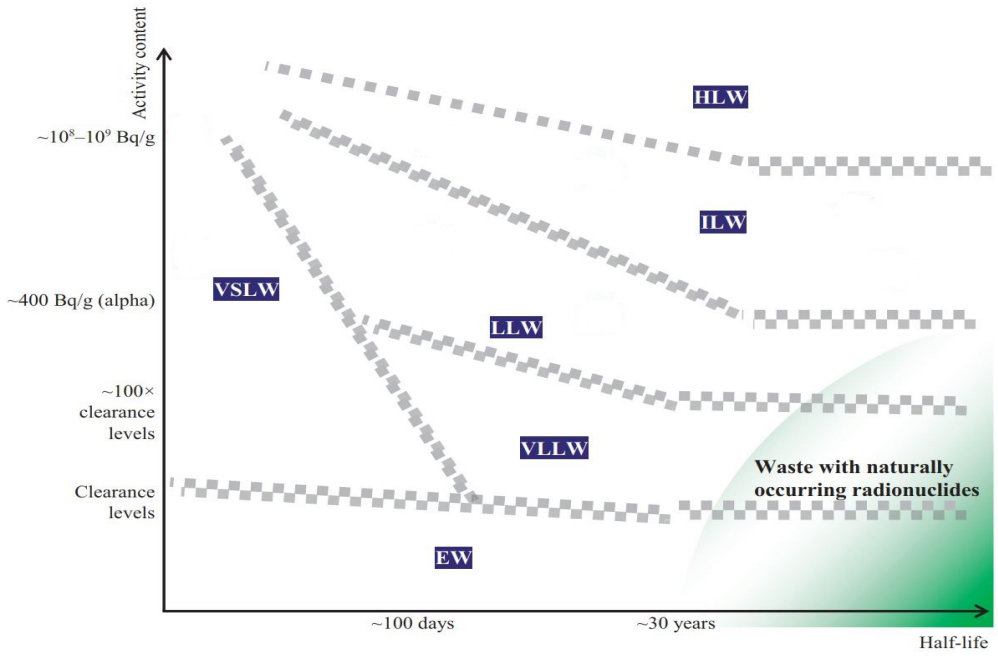

Figure 2.1: Waste classification scheme in terms of activity content[10](specific or total activity) and the half-life of the radionuclide. Distinguished main waste classes, such as EW (Exempt waste) that can be cleared from regulatory control, VSLW (very short-lived waste), VLLW (very low level waste), LLW (low level waste), ILW (intermediate level waste) and HLW (high level waste) [17].

In Figure 2.1, the horizontal axis represents the typical half-lives of the radionuclides contained in the waste, which can range from very short (days) to long time spans (dozens of years). In accordance with the radioactive waste safety rules presented in the General Safety Guide [17], radionuclides with the half-lives below 100 days are classified as very short-lived whereas those with the half-lives below approximately 30 years as a short-lived. Considering the main characteristics of metallic radioactive waste generated at CERN (see Section 2.3.3), the radionuclide inventory includes short-lived radionuclides such as ^{55}Fe with a half-life 2.7 years, ^{60}Co with a half-life 5.3 years and long-lived radionuclides, e.g., ^{63}Ni with a half-life approximately 100 years.

[10] According to IAEA glossary, the term 'activity content' covers activity concentration, specific activity and total activity, and it is used because of the general heterogeneous nature of radioactive waste

Following the vertical axis of Figure 2.1, the level of activity content starts from negligible to very high. For example, waste containing only small amounts of certain radionuclides may meet the criteria for clearance, exemption or exclusion from regulatory control for radiation protection purposes [13] and therefore might belong to Exempt waste (EW) category.

The classification is based on the radioactivity concentration and half-lives of radionuclides. The categorization of waste is a complementary approach, which includes other waste properties, such as origin, physical state, type of waste and processing options[11].

In particular, IAEA categorizes waste as unconditioned or conditioned [15]. Figure 2.2 shows the operational process of those two categories.

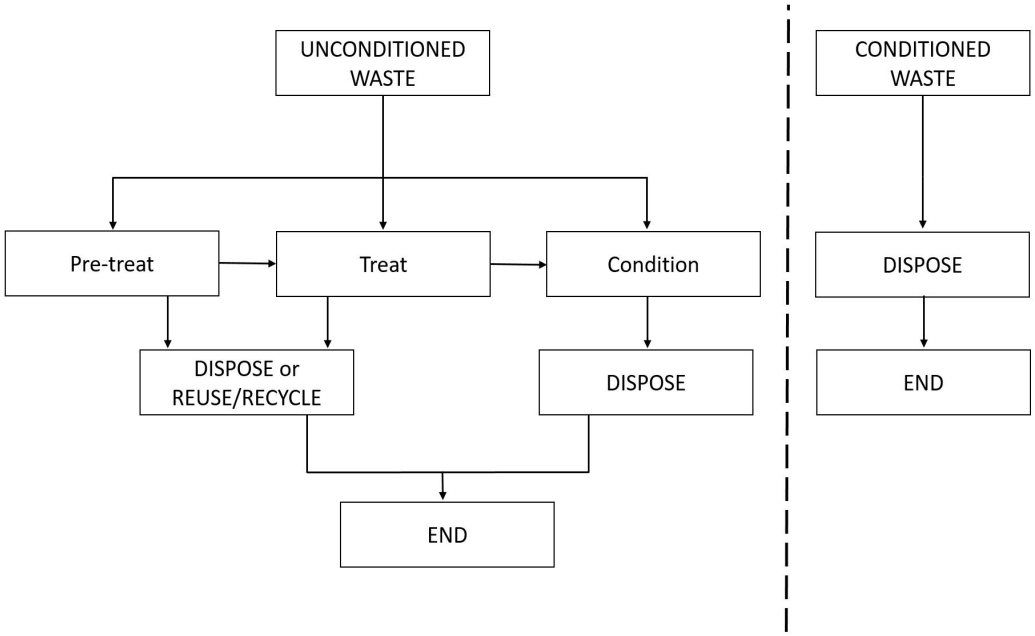

Figure 2.2: Waste categorization overview; indication of potential disposal options. Adapted from [15].

Unconditioned waste is defined as a raw, pretreated and treated. The pre-treatment may include operations, such as collection or segregation, chemical adjustment and decontamination of waste. One result of the pre-treatment may be a reduction in the amount of waste that would be subject to further processing and disposal.

The pre-treatment operation might rely on the collection and the segregation of waste. In particular, radioactive waste at CERN, with an estimated dose rate greater than 100 μSv/h is segregated in dedicated shielded areas in the Radioactive Waste Treatment Centre and Storage (RWTCS).

The treatment operation concept based on the changing of the radioactive waste characteristics by reduction of waste volume, removal of radionuclides from the waste and change of waste

[11] By the waste processing we determine any operation that change the characteristics of waste, including pre-treatment, treatment and conditioning [11].

composition, for instance by evaporation and change of form or composition by a chemical process. Volume reduction of solid waste by compaction is widely used in waste treatment. As an example, we might include a common operation adapted at CERN, which relies on the usage of an industrial press-shears [121].

In addition, LL/IL metallic waste stored at RWTCS will be subjected to melting in the future. The objective of this treatment is the volume reduction of waste items. Melting of the LL/IL metallic waste results in the homogenization of the activity and accumulation of this activity within produced ingots for instance and generation of secondary waste, like ash or accumulation of residues within the filter system.

Operations for conditioned waste lead to the production of waste packages[12] that are appropriate for handling, transport or disposal. In general, conditioning operations may require immobilization of the waste in a matrix. Common materials applied in the immobilization process for stabilization of radioactive waste within the package might be bitumen and polymers [12].

CERN has the capacity to pre-treat, treat, measure and package radioactive waste. Waste produced at CERN prior to the disposal facility does not require immobilization or stabilization processes. Nevertheless, its elimination due to the lack of waste conditioning facilities at CERN, all radioactive waste is sent to final repositories for conditioning and disposal as required.

IAEA lists key parameters that can be used to characterize radioactive waste [14]. A summary is presented in Table 2.1.

Table 2.1: Key parameters that might be used in the characterization process [26].

	Unconditioned waste	**Conditioned waste**
Radiological properties	- Total activity and activity concentration of radionuclides	- Total activity
	- Origin of the activity (contamination or activation)	- Radionuclide composition
	- Surface dose rate	- Surface contamination
Physical properties	- Physical state	- Size and weight
	- Volume, mass and dimensions of waste items	- Structural and dimensional stability
	- Volatility, miscibility etc.	
Chemical properties	- Toxicity	- Chemical stability
	- Chemical composition	- Homogeneity
	- Combustibility and flammability	- Fire resistance
Biological properties	- Potential biological hazard	
	- Infectious/pathogenic	

[12] The waste package is defined as a product that includes the waste itself, any container and internal barriers. The waste package need to be prepared in accordance with requirements for handling, transport, disposal [28]

Key parameters that we consider to apply during the characterization process of LL/IL waste at CERN includes the activity of waste items, physical and chemical properties such as physical state, volume, mass, dimensions and chemical composition. We focus on metallic waste, mainly made of steel, aluminium and copper. These key parameters can be used to establish whether waste items need to be melted and later on sent to the disposal facility or if they can be sent directly to the dedicated disposal facility.

2.2 Legacy and new radioactive waste

According to IAEA, if radioactive waste is generated with a traceability system in place, waste is considered as "new". The major feature of this category of waste is that the characterization can be accurate because the history of the waste is known.Conversely, legacy waste is defined as waste generated without a complete traceable characterization system in place. For this waste, the characterization process is more intensive and expensive, due to systematic and extensive measurements.

The notion of new and legacy waste generated at CERN is the following. We have kept traceability for virtually all radioactive waste. However, legacy (or historical) waste represents the waste produced and stored before an elimination pathway was available. Therefore, the waste was not sorted or treated adequately, and reworking is needed when the pathway is defined. For new waste, the elimination pathway is defined and consequently, we can sort and treat the waste directly with the right procedures.

The purpose of the present thesis is to propose a characterization strategy for legacy waste, focusing on metallic LL/IL waste produced at CERN. A more detailed description of LL/IL waste is given in section 2.3.3.

2.3 Radiological classification of radioactive waste

Radioactive waste and activated material produced at CERN is either disposed of in France or Switzerland in accordance with the existing elimination pathways. The following Sections 2.3.1 and 2.3.2 present the radiological acceptance criteria for the already established elimination pathways at CERN: the clearance from regulatory control of non-radioactive waste and the disposal of Very low level (VLL) waste. Moreover, we present the radiological criteria used for the new radiological characterization process of the LL/IL waste (see Section 2.3.3) which is being established at CERN. Indeed, the aim of the present thesis is to propose and to implement a radiological characterization process for LL/IL waste.

2.3.1 Clearance waste

In Switzerland, the clearance from regulatory control can be achieved, if it can be demonstrated by measurements and calculations, that the material is non-radioactive according to the Swiss Radiation Protection Legislation described in [16] [19]. In particular, the material needs to fulfill all the following criteria:

1. **Surface contamination (CS)**, which is the sum of the following activities: the non fixed activity, which can be removed from a surface by wiping or washing and the fixed activity, which can be removed during future use. For example, the CS of Co-60 needs to be below or equal to 3 Bq/cm^2.

2. **Specific activity** shall be lower than the clearance limit (limite de libération (LL) in French), such that the material is no longer subject to authorization and therefore to surveillance. For instance, the LL value given for Co-60 is 0.1 Bq/g.

3. **Dose rate** ($\dot{D}$), which is an operational quantity used to estimate the exposure of a person to radiation. The ambient equivalent dose rate at 10 cm distance from the material surface shall be lower than 0.1 μSh/h.

2.3.2 Very low level radioactive waste

VLL waste in France is identified as Très Faiblement Actifs (TFA) waste. In order to verify if waste can be disposed as VLL waste in the French final disposal facility, French National Agency for Radioactive Waste Management (ANDRA), which is responsible for guaranteeing safe management solutions for all French radioactive waste has defined a factor Indice Radiologique d'Acceptabilité en Stockage (IRAS), for a waste package, given by Equation 2.1

$$IRAS = \sum_i \frac{a_i}{AL_i}, \tag{2.1}$$

where a_i is the specific activity of radionuclide i and AL_i expresses the level of the radiotoxicity hazards[13] of the radionuclide i, and it is defined as follows (Equation 2.2):

$$AL_i = 10^{Class_i}, \tag{2.2}$$

where the $Class$ of radionuclide i expresses its level of radiotoxicity hazards. The $Class$ varies from 0 (high radiotoxicity) to 3 (low radiotoxicity). The list of radionuclides with corresponding classes can be found in [23]. If a radionuclide i exceeds its declaration threshold, it must be declared and included in the IRAS computations.

A computation of weighted IRAS allows verifying the acceptability of a batch of packages of radioactive waste, where M_k is the weight of the k package and $IRAS_k$ is the IRAS value of the k package.

$$\langle IRAS \rangle = \frac{\sum_k M_k \cdot IRAS_k}{\sum_k M_k}. \tag{2.3}$$

The acceptance criteria for a batch of packages of radioactive waste is $\langle IRAS \rangle \leq 1$.

Considering the maximum acceptable IRAS factor of 10 for each waste package of VLL radioactive waste, an operational sorting criterion regarding the dose rate threshold for the identification of VLL radioactive waste has been established (see [89]). The calculations are based on establishing the correlation of the contact dose rate and the maximum activity of the dominant gamma emitter (Co-60) for the IRAS factor of 10. These calculations and the benchmarks demonstrate that the waste with the maximum dose rate lower than 100 μSv/h can be considered as candidates for disposal as VLL waste.

2.3.3 Low– and intermediate radioactive waste

LL/IL waste in France is identified as Faible et Moyenne Activité (FMA) waste. This class of waste covers approximately 11% of waste in mass stored at CERN. LL waste usually has a limited amount of long-lived radionuclides. If long-lived radionuclides are present, they often have relatively low levels of activity concentration. Figure 2.1 also shows that LL waste covers the range of short-lived radionuclides with high activity concentration. Conversely, IL waste may contain predominantly long-lived radionuclides; thus this waste requires disposal at greater depths [17].

The classification of a waste as LL/IL does not depend only on the activity concentration. ANDRA specifies the acceptance criteria of LL/IL waste in the technical note [22].

In order to accept loose LL/IL waste inside containers without stabilization in the short-lived disposal facility in France, waste needs to fulfil several requirements, namely:

[13] Radiotoxicity hazards may be due to the ability of the radionuclide to produce damage or injury, by virtue of its emitted radiations, when incorporated in the surface or body [4]

- the specific activity of each radionuclide in the waste package shall be less than a Coating threshold (Seuil d'enrobage) (SE);

- the sum of specific activities confining threshold of all beta and gamma emitters shall be less than $3.7{\cdot}10^4$ Bq/g;

- the specific activity of each alpha emitter with a half-life $\leq$ 31 years shall be less than $3.7{\cdot}10^3$ Bq/g;

- the sum of specific activities of all alpha emitters with half-lives $\leq$ 31 years shall be less than $3.7{\cdot}10^4$ Bq/g.

To guarantee the radiological safety for packaging, transport or disposal, we have to follow rules to avoid radiotoxicity hazards. In a case of exceeding one of the given specific activity values, as presented above, we have to implement additional coating or internal barrier for packaging or transporting the waste items. Table 2.2 presents activity limits for short-lived radionuclides. The complete list can be found in [22]

Table 2.2: Activity limits for LL and IL short-lived radionuclides with half-lives $\leq$ 31 years .

Radionuclide	**Declaration threshold [Bq/g]**	**Coating threshold (SE) [Bq/g]**	**Maximum acceptable limit [Bq/g]**
H-3	10	$7.4{\cdot}10^4$	$2{\cdot}10^5$
Na-22	1	$2{\cdot}10^4$	$1.3{\cdot}10^8$
Mn-54	10	$3.7{\cdot}10^4$	$3.6{\cdot}10^8$
Fe-55	10	$3.7{\cdot}10^4$	$6.1{\cdot}10^9$
Co-60	10	$3.7{\cdot}10^3$	$1.3{\cdot}10^8$

169 Long-lived radionuclides with half-lives > 31 years are accepted in French short-lived disposal
170 facility within given limits, as determined in Table 2.3

Table 2.3: Activity limits for LL and IL long-lived radionuclides with half-lives > 31 years [22].

Radionuclide	**Declaration threshold [Bq/g]**	**Coating threshold (SE) [Bq/g]**	**Maximum acceptable limit [Bq/g]**
Be-10	$1.0{\cdot}10^{-4}$	-	$5.1{\cdot}10^{3}$
C-14	1	$3.7{\cdot}10^{3}$	$9.2{\cdot}10^{4}$
Cl-36	$1.0{\cdot}10^{-2}$	-	5
Ca-41	$1.0{\cdot}10^{-4}$	-	$3{\cdot}10^{5}$
Ni-59	$1.0{\cdot}10^{-1}$	$3.7{\cdot}10^{3}$	$1.1{\cdot}10^{5}$
Ni-60	1	$3.7{\cdot}10^{3}$	$3.2{\cdot}10^{6}$

2.4 LL/IL waste stored at CERN

Radioactive waste generated at CERN is temporarily stored at Radioactive Waste Treatment Centre and Storage (RWTCS) located in the former Intersecting Storage Ring (ISR) tunnel. The layout of the RWTCS is presented in Figure 2.3. The estimation of the amount of radioactive waste stored at RWTCS and the prediction of new waste generated in the future at CERN, e.g., during Long Shutdown[14] are given in [49], [88]. The estimated total mass of radioactive waste stored at CERN at the time of writing this thesis, is ∼7300 tons, occupying a volume of 6500 m^3.

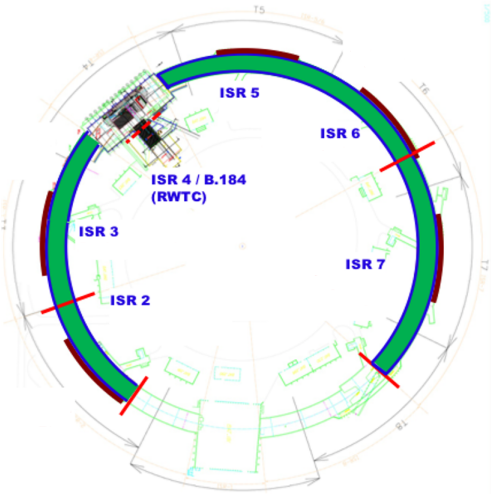

(a) LL and IL waste are stored in octants 5 and 6. A 30 tons crane for handling waste items is also installed.

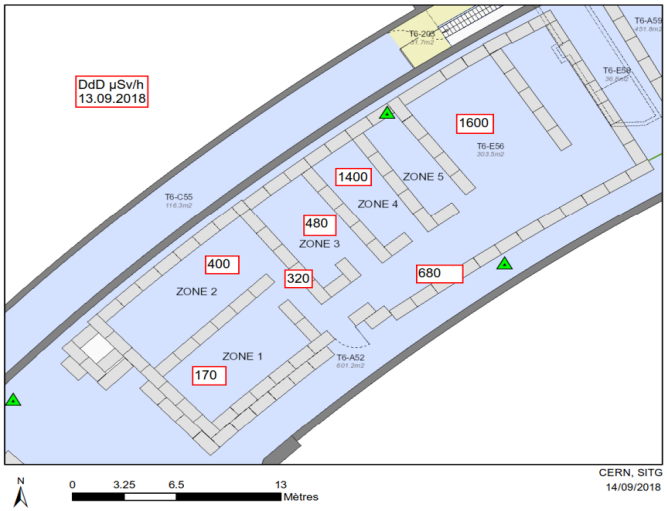

(b) Layout: octant 6 with shielded zones. Dose rate measurements performed on 13/09/2018.

Figure 2.3: RWTCS layout with separated octants.

[14] https://home.cern/news/news/accelerators/new-schedule-lhc-and-its-successor, 23 February 2021

In order to distinguish between VLL and LL/IL, the experimental threshold of the dose rate at 100 μSv/h is set (refer to Section 2.3.2). Out of 627 tons of stored waste in dedicated shielded areas at RWTCS, 242 tons of waste with the dose rate greater than 100 μSv/h are considered as LL/IL candidates. In particular, these waste items were typically produced during dismantling campaigns performed 10–30 years ago, and stored in the shielded areas at RWTCS due to lack of any elimination pathways.

The majority of stored LL/IL waste is made of steel, aluminium and copper. They vary according to levels of dose rate, activity distribution, apparent density, contamination risk and origin.

Representation of waste stored at RWTCS, such as pipes, ion pumps, 1.5 m^3 containers filled with metallic waste and beam supporting structures is depicted in Figures 2.4a–2.4d. The apparent density of this waste ranges from 0.08 g/cm^3 to 7 g/cm^3 and the weights are from 20 kg up to 2700 kg. The metallic waste mainly origin from SPS and PS accelerators.

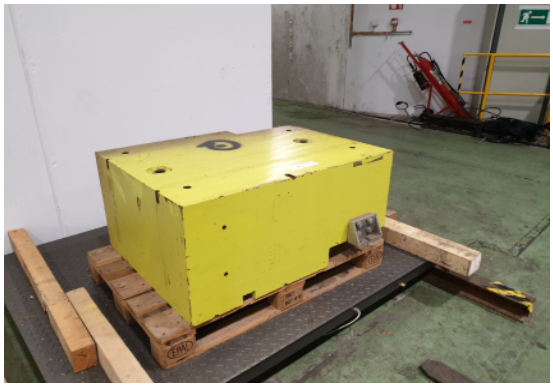

(a) 2.5 tons supporting structure. The highest dose rate is 400 μSv/h.

(b) Pipe with length $>$ 2 meters and thickness 2 mm. The average dose late for selected pipes is from 60 to 150 μSv/h.

(c) Ion pump made of metallic non-magnetic and magnetic materials. The highest dose rate measured is $<$1 mSv/h

(d) 1.5 m^3 containers with metallic waste.

Figure 2.4: Examples of waste items selected in the shielded area of RWTCS.

Chapter 3

Radionuclide inventory and estimation of activity concentrations

In this chapter, we introduce concepts to assess the radioactivity of activated waste at CERN. In order to be disposed of in dedicated disposal facilities, the radioactive waste needs to be classified. Such classification requires the estimation of the activity concentrations of identified radionuclides. Within the scope of this thesis, we seek to estimate the radionuclide activity values of LL/IL radioactive waste according to the acceptance criteria of LL/IL waste in the short-lived disposal facility in France, as presented in Section 2.4. In order to achieve this objective, we develop dedicated methods that are based on both analytical calculations and experimental data. This characterization methodology is generally introduced in Section 3.1.
The following Section 3.2 describes the analytical calculations; the Monte Carlo methods and calculation tool used for radiological characterization purposes.
In addition, the detailed description of the experimental methods in order to quantify the waste activity values can be found in Section 3.3. A summary of the radiological characterization workflow is presented in Section 3.5.

3.1 Characterization methodology

There are two general calculation methodologies that can be applied for estimating the radioactivity of radioactive waste, the point and the range methods [72]. The point method is dedicated to calculations for single items, or waste generated in a small quantities. This method features high accuracy, because of the uniform properties and known history of the waste (including irradiation time t_i). In CERN's accelerator complex, the point method could be applied to targets irradiated at the ISOLDE facility. CERN also features another type of waste, whose radioactivity levels depend on multiple parameters, such as material composition and localization in the accelerator complex. In the range method, those input parameters are used in the calculations. If the activated components installed in CERN accelerators have the same material composition and irradiation conditions, then the ratio of produced radionuclides at the same position for those components is constant. The range method can then provide the average activity and distribution of such activated items. A typical range method applicable in the radiological characterization process is the correlation method. The concept of the Correlation factor (CF) is similar to Scaling factor (SF) method (detailed information can be found in Section 3.4). A combination of these two concepts (CF and SF methods) is deployed in the radiological characterization of LL/IL waste at CERN.

The radionuclide inventory can vary within waste, due to variations in chemical composition and particle spectra. According to the reference [14], we classify radionuclides as Easy-to-measure (ETM), Difficult-to-measure (DTM) or Impossible-to-measure (ITM).

ETM radionuclides are gamma-emitting nuclides, whose radioactivity levels can be measured directly by Non-Destructive Assay (NDA) means. The dominant identified gamma emitter is referred to as Key Nuclide (KN). The KN is used in evaluating the activity concentration of Difficult-to-measure. The KN needs to fulfill several criteria. Its radioactivity should be correlated with the DTM nuclides and have a relatively long half-life, with respect to the cooling times of interest. Additionally, the KN should have similar production mechanisms as the DTM nuclides [73].

DTM is a nuclide whose radioactivity is difficult to measure directly from the outside of a waste by NDA techniques. It requires complex destructive techniques, involving chemical and radiochemical treatments on the collected samples. The DTM nuclides include pure beta-emitting nuclides and those emitting low energy photons. Some of them are classified as ITM since they do not lend to Destructive Assay (DA) techniques. Therefore, the ITM nuclides such as alpha-emitting or low-energy X-emitting nuclides can be quantified via simulations or calculations using the analytical code ActiWiz [1], which relies on the extensive Monte Carlo simulations using FLUKA [37].

3.2 Activation calculations and simulation codes

In this section, we introduce the Monte Carlo and analytical calculation methods and tools dedicated for radiological characterization purposes.
The Monte Carlo code FLUKA[15] [41][39][59] is intended to simulate the transport and interaction of hadronic and electromagnetic particles from a few keV up to 10000 TeV in arbitrary materials [57]. The calculation software ActiWiz [115] is intended to estimate the radiological hazards of irradiated materials in the CERN's accelerator complex.

3.2.1 Monte Carlo code FLUKA

To simulate physical systems, Monte Carlo methods should describe the system in terms of a Probability Density Function (PDF). Hence, if the density function of a system is known, the simulations can generate random numbers following this density distribution. The outcome of such a simulation should be in accordance with the mathematical or physical theory that describes a given physical system [92].
The FLUKA code is a general purpose Monte Carlo code used extensively at CERN for calculations of particle transport and interactions with matter.
FLUKA is capable of predicting induced radioactivity in a given material and geometry, including nuclide production and radioactive decay as well as transport of residual radiation. In particular, FLUKA allows estimation of the time evolution of produced nuclides with an exact analytical implementation of the Bateman equations describing activity build-up and radioactive decay for arbitrary irradiation profiles [38][59].
All nuclear interactions depend on the particle energy and are described in the FLUKA code by various physics models. The FLUKA hadronic interactions are handled using the PreEquilibrium Approach to Nuclear Thermalization (PEANUT) code from threshold of 20 MeV (for neutrons) up to several dozen of TeV. The PEANUT includes the Dual Parton Model (DPM)[50] and Glauber-Gribov cascade of high-energy interactions (up to 20 TeV), a very detailed Generalized Intra-Nuclear Cascade (GINC) as well as pre-equilibrium emission model. Additionally, PEANUT features models for evaporation, fragmentation, fission and gamma deexcitation.
The ion interactions are described by the Boltzmann Master Equation (BME) for energies below 0.1 GeV/nucleon, the rQMD-2.4 in the energy range between 0.1 GeV/nucleon and 5 GeV/nucleon, and the DPMJET3 for energies above 5 GeV/nucleon [105]. In FLUKA, the transport of neutrons with energy below 20 MeV is handled by the multi-group algorithm based on evaluated cross section data, such as ENDF/B, JEF, JENDL, etc. With the multi-group transport technique, the energy range of interest is divided into a number of discrete intervals called "energy groups". Each group is identified by a number increasing with decreasing energy. The energy range of the library starts from 0.01 meV up to 20 MeV[38][59].

[15] https://fluka.cern, 30 March 2021

The Fluka input consists of more than 70 parameters (see the list [59]). In order to generate the FLUKA input file, we need to implement commands that define the radiation source, the geometry layout, materials (chemical compositions and densities), requested results (called scorings) and optional settings, e.g. energy cut-offs, for both transport and production.
Thanks to the FLUKA Monte Carlo code capabilities, any particle spectra for any areas in the CERN's accelerator complex can be calculated. The obtained particle spectra can then be subsequently used in ActiWiz as described in the following section.

3.2.2 ActiWiz

ActiWiz [1] is a software tool developed at CERN to assess and compare the radiological hazard of materials exposed in the CERN accelerator's complex. All ActiWiz scenarios (as provided in the ActiWiz default libraries)are based on a vast amount of FLUKA simulations. ActiWiz allows rapid estimation of radionuclide production yields without implementing complex input files with a Monte Carlo code using FLUKA [115].
The new generation of ActiWiz (version 3) is not limited to predefined radiation fields. ActiWiz version 3 can use arbitrary particle fluence spectra as an input and independently calculate the nuclide production terms without further Monte Carlo calculations.
Nuclide inventories can be determined as a function of randomly sampled parameters including the material chemical composition, the beam energy, the position of exposure in the accelerator as well as the irradiation and cooling times. The combination of a set of those random variables represent a so-called scenario **S** [113]. From a mathematical point of view the **S** is a mixed multivariate random variable (or a vector) and can be written as follows [121]:

$$\mathbf{S} = (CC, E, P, t_i, t_c). \tag{3.1}$$

Where:

CC - chemical composition;

E - beam energy;

P - material position in accelerator;

t_i - irradiation time;

t_c - cooling time.

subsequently, ActiWiz's nuclide inventory generated from the set of mixed multivariate random variable, needs to be compared with regulatory or acceptance limits (e.g.clearance limit) or conversion functions (e.g. dose equivalent or inhalation dose). The following sections describe in detail the components of Equation 3.1.

3.2.2.A Material chemical composition

This section introduces the first input parameter, material chemical composition of the activated waste item. The chemical composition, of a given material, is crucial to evaluate the production rates of the radionuclides, when it is exposed radiation beam losses in the accelerator. The knowledge of the exact elemental composition of the legacy waste stored at CERN might be limited due to the unavailability of a traceability system in place at the time of the waste generation. Additionally, the quantity of impurities can be below the detection limits of the common instruments used at CERN to evaluate the chemical composition (above 50 to 100 ppm for most elements).

Gathering information about elemental composition can be done via direct measurements or based on the literature, national and international standards, like [25]. The collected data can be either in the format of a single value or of a statistical distribution.

The radiological characterization carried out at CERN uses the chemical compositions from a material catalogue [61]. The catalogue is based on information collected from the original suppliers' data and values from European and international standards for materials that are used to build accelerator components and structures. This material catalogue consists of 69 chemical elements and 66 compounds. To establish a representative radionuclide inventory of legacy metallic LL/IL waste generated at CERN's accelerator complex, the chemical compounds are grouped into three main families: steel, aluminium and copper. The list of major chemical compounds for those materials is presented in Table 3.1.

Table 3.1: The list of typical chemical compositions used at CERN accelerators. These compositions are also implemented in the ActiWiz simulations to access the produced radionuclide inventory of the LL/IL waste. Values in parenthesis are given as weight fractions.

Material	Composition of materials in reference concentration
Aluminium 6060	Al (98.375), Mg (0.475), Si (0.45), Fe (0.2), Zn (0.15), Cu (0.1), Mn (0.1,), Ti (0.1), Cr (0.05)
Steel 304L	Fe (67.0825), Cr (18.5), Ni (11.25), Mn (2.0), Si (1.0), Co (0.1), C (0.03), P (0.0225), S (0.015)
Copper OFE	Cu (99.99), S (0.0018), Bi (0.001), Pb (0.001), O (0.0005), Cd (0.0001), Hg (0.0001), Zn (0.0001)

In reality, the exact amount of impurity and trace elements will vary considerably among different waste items following a probability distribution. This feature is described in [72]. A basic approach for setting the distribution shape is shown in Table 3.2.

Table 3.2: Approach of setting basic type of distribution of chemical element concentrations. Adapted from [72]

Chemical element condition	Main elements	Impurity elements	Trace elements
	Controlled in a certain range of concentration	Controlled with un upper limit of concentration	Non-controlled
Basic approach	Main chemical elements of materials which are manufactured in specific factories under lot-based quality control. Their contents are controlled within the target range specified by national industrial standards of material, and their concentration ranges are comparatively narrow.	Chemical elements which are reduced or controlled in a certain manufacturing process as impurity elements contained in manufactured materials. Their contents are controlled below comparatively low control values, and the concentration distribution of each element is able to reflect its concentration distribution in nature.	Chemical elements which are not controlled. The content of each element reflects its concentration distribution appearing in nature.
Reference concentration distribution of each chemical element	Normal distribution	Log-normal distribution	Log-normal distribution

The setting of the concentration distribution conditions, of each chemical element, can be divided into four cases [72] according to the available element analysis data.

- A sufficient and representative element analysis data are collected for radioactive waste. The concentration distribution condition can be set by using the average values, standard deviation or maximum/minimum values of each element.

- The element analysis data are relatively sparse for radioactive waste. Setting of the concentration distribution condition can be made by applying values being the upper limits of the confidence intervals obtained from data for each element.

- Most of the element analysis data is below the detection limit. It is possible to estimate the chemical element concentration either assuming the average concentration and standard deviation from detected values or using the the concentration distribution in a range below the detection limit. For example, we can assume that the average is determined by assuming maximum detected value located at $+2\sigma$ value of the concentration distribution and standard deviation is evaluated from the same element data in the nature.

- The element analysis data contain only detection limit values. It is possible either to use detection limit values to evaluate averages and standard deviation values, or set a concentration distribution in a range below the declaration limit, or estimate from radiochemical analysis results if the irradiation conditions are known by varying the composition values to match the measured nuclide inventory.

Example 1 provides the reader with an example of the expected radionuclides generated under specific irradiation conditions. It provides an outline of the list of possible radionuclides generated with their contribution to the total radioactivity for the selected materials. Measuring the radionuclide inventory and precisely defining the activation scenario allows reconstructing the chemical composition.

Example 1 *Using ActiWiz, we exposed Steel 304L, Aluminium 6060 and Copper OFE to the radiological environment of CERN's accelerator complex. The activation occurs at the beam impact area (see Table 3.4), the materials are irradiated for 20 years and they are left to decay for 10 years after the irradiation time. The list of major radionuclides produced with their % contribution to the total activity (>1%) from ActiWiz calculations is presented in Table 3.3*

Table 3.3: Radionuclide inventory generated for irradiated Steel 304L, Aluminium 6060 and Copper OFE [61] at the beam impact area. The irradiation time is 20 years, the time which has elapsed since the end of the exposure is 10 years.

Radionuclide	Contribution to the total activity in %		
	Steel 304L	Copper OFE	Aluminium 6060
H-3	78.04	80.00	95.38
Fe-55	18.71	3.14	0.07
Co-60	0.81	6.32	0.01
Sc-44	0.76	0.24	0.01
Ti-44	0.76	0.24	0.01
Ar-39	0.32	0.19	
Na-22	0.20	0.08	4.46
Ni-63	0.12	9.59	0.02
P-32	0.06	0.05	
Si-32	0.06	0.05	
Mn-54	0.04	0.01	
V-49	0.04	0.01	
K-42	0.04	0.04	
Ar-42	0.04	0.04	
C-14	0.01	0.01	0.03
Ni-59		0.01	

In addition, an extensive example of the techniques used to establish the elemental concentration distribution in cathodic copper can be found in [121] (Chapter 2). Similar procedures can be applied for other materials when constructing elemental compositions for activation studies.

3.2.2.B Material position and beam energy in the accelerator (*P*), (*E*)

The ActiWiz code version 3 has implemented the activation positions representing the CERN's accelerators including the Linac 4, the PS Booster, the PS, the SPS and the LHC. The composition of the radiation field depends on the position of the material with respect to the beam loss point. As presented in Figure 3.1, the bulky iron cylinder geometry setup allows estimation of the activation in the case of beam impacts on a massive objects like magnets. On the other side, the iron cylindrical target geometry focuses on the impact on the target, resembling beam losses on objects providing little self-absorption like collimators. The positions considered in ActiWiz are divided into seven typical irradiation locations described in Tables 3.4 and 3.5.

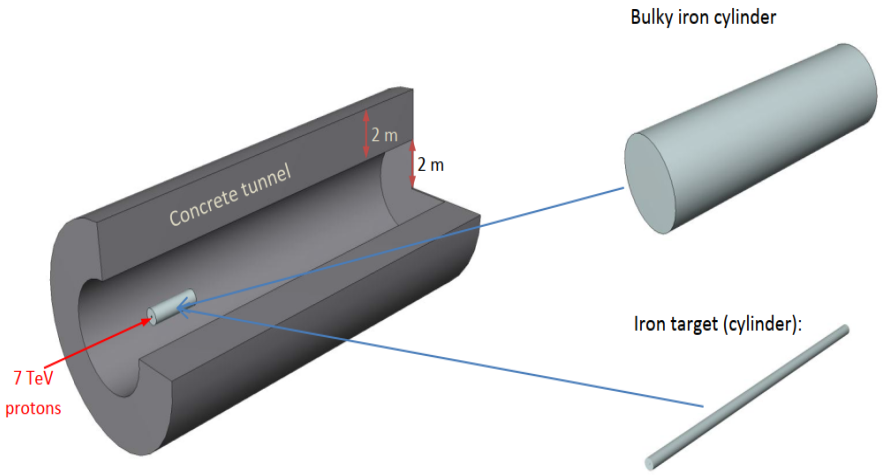

Figure 3.1: Simulation geometry used to calculate the material activation at various locations. There are two beam impact objects: a two meter long bulky cylinder with a radius of 50 cm and a two meter long cylindrical target with a radius of 3 cm [61].

The radiological environment in CERN's accelerator complex can be represented in total by 42 possible combinations of the parameter values of energy (*E*) and position (*P*) in the random vector scenario **S**.

Table 3.4: Irradiation locations for the bulky material (e.g. magnets) [61] and [121].

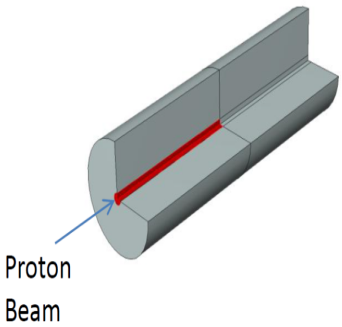

1. The red cylinder represents the beam impact area (BeamImpact). The irradiation situation can be used to characterize the activation of the material hit directly by beam.

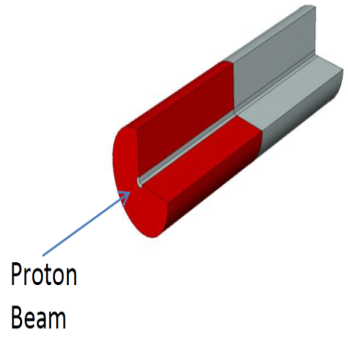

2. The red hollow cylinder (3 cm <r <50 cm) represents the bulky material surrounding the beam impact points. The irradiation situation can be used to characterize the activation massive materials located close to objects intercepting protons from the beam line (WithinBulky).

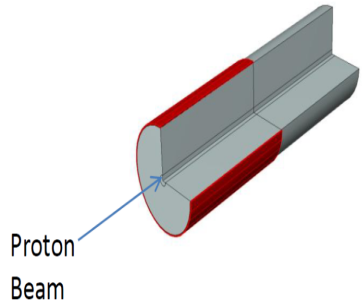

3. The red hollow cylinder (50 cm <r <51 cm) is placed adjacent to the bulky material surrounding the beam impact points. This irradiation situation is important for all LHC equipment which is located laterally to the LHC magnets (AdjBulky).

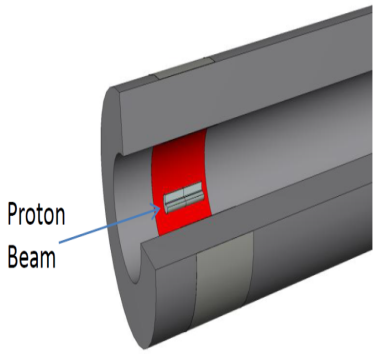

4. The red thin hollow cylinder (199 cm <r <200 cm) is close to the tunnel wall at the lateral distance from the beam line of two meters. The scoring volume is used to characterize the activation of materials in radiation fields occurring close to the concrete tunnel wall (e.g. cable trays) (ClosewallBeamOnBulky).

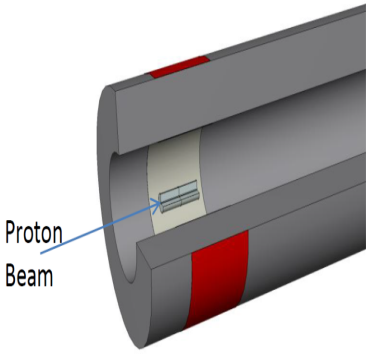

5. The red hollow cylinder is located behind two meters of massive lateral concrete shielding. This irradiation situation can be applied for material activation behind thick lateral concrete walls which shield radiation from beam impacts (BehindWall).

Table 3.5: Irradiation locations for the beam-on-target (e.g. collimators) [61] and [121].

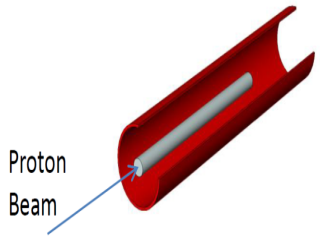

6. The red hollow cylinder with thickness of 1 cm. This irradiation situation is used for the activation calculations considering location at a lateral distance of 10 cm to the target. Such a geometry configuration is important for materials located close to unshielded beam line equipment of small lateral extension (10cmTarget).

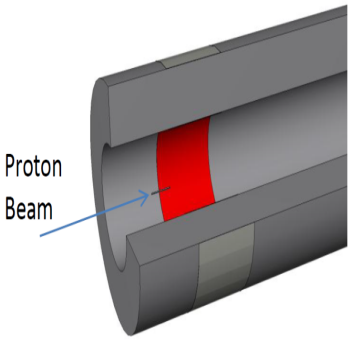

7. The red hollow cylinder is located close to the concrete tunnel walls at the lateral distance of two meters from the beam line axis. The situation can be used to describe all equipment located adjacent to the tunnel wall in the area of beam equipment with small lateral extension (CloseWallBeamOnTarget).

Example 2 *In this example, we simulated the exposure of Steel 304L to a 400 GeV/c proton beam, which corresponds to the SPS accelerator. The activation occurs at the following locations: the beam impact point, close to the concrete tunnel wall, behind the massive concrete shielding, adjacent to the bulky material and within the bulky material surrounding the beam impact area. The Steel 304L was irradiated for 20 years and decayed for 5 years after the end of the irradiation.*

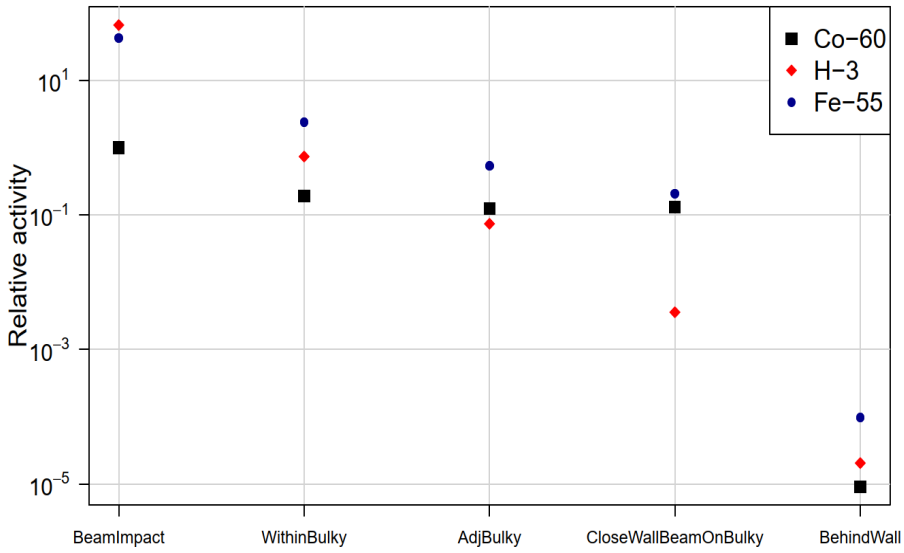

Figure 3.2: The differences between activity concentrations for activation caused by beam losses in bulky material type (e.g. magnets). All activity values are normalized to the highest activity value of Co-60. The activation scenario is generated for a 400 GeV/c proton beam impacting on a steel cylinder. Irradiation time is 20 years and cooling time is 5 years. The relative activity values include the estimated particle losses (see Table 1.2) for CERN's machines.

As presented in Figure 3.2, the activity concentration between two extreme locations of activation at the beam impact area and behind massive concrete shielding varies by five or six orders of magnitude for the radionuclides Co-60, H-3 and Fe-55.

194 ***Example 3*** *This example shows the distribution of relative radioactivity for different proton*
195 *energies beam in CERN's accelerator complex for two positions, at the beam impact and behind*
196 *walls for Steel 304L. The irradiation profile is set to 20 years of irradiation and 5 years of*
197 *cooling times. This is a consequence of the variation of the particle fluencies across different*
198 *irradiation positions and nuclear cross section for various energies.*

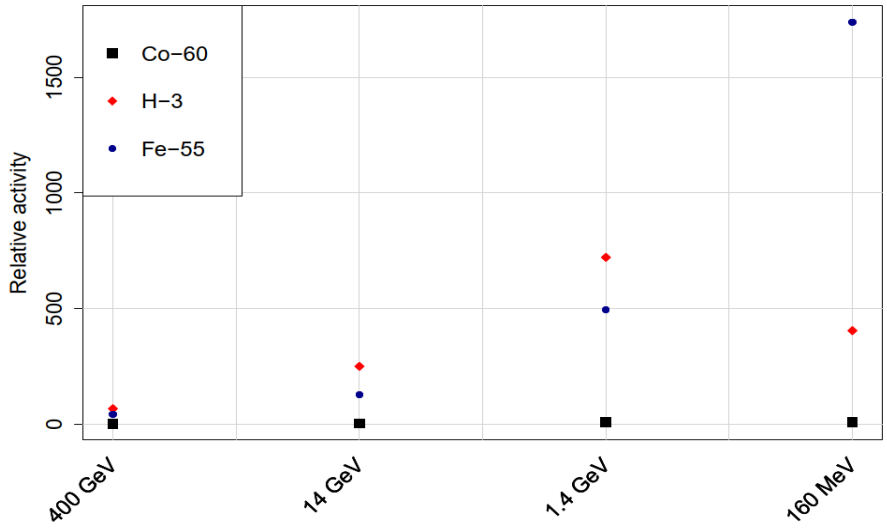

(a) The irradiation simulation at the beam impact area. The relative activity values are normalized to the corresponding Co-60 activity value obtained using the highest energy beam of SPS 400 GeV/c.

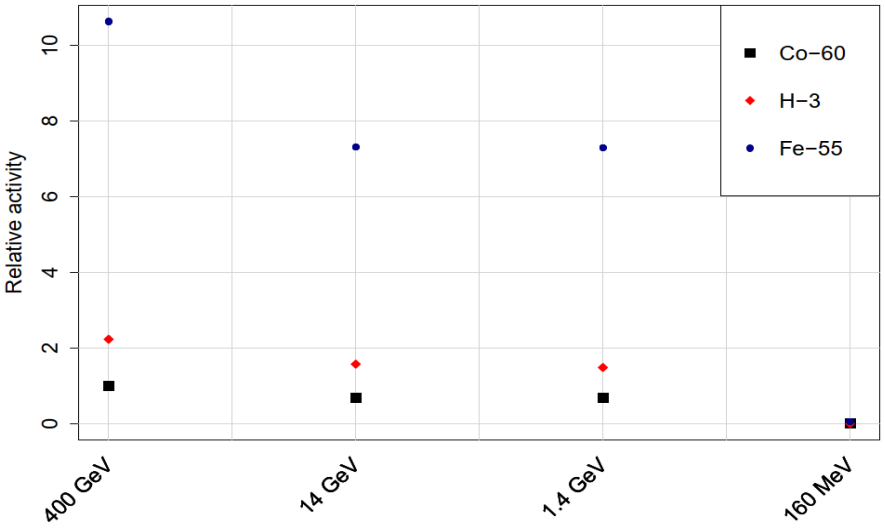

(b) The irradiation simulation behind the thick lateral concrete walls.The relative activity values are normalized to the corresponding Co-60 activity value obtained using the highest energy beam of SPS 400 GeV/c.

Figure 3.3: Activity concentration in terms of different energy beam in the accelerators: SPS, PS, PS Booster and linear accelerator Linac 4. The relative activity values includes the estimated particle losses (see Table 1.2) for CERN's machines.

3.2.2.C Irradiation and cooling time (t_i), (t_c)

The irradiation and cooling times are introduced in Section 1.4 dedicated to the induced radioactivity.

One can write the scaling factor as a function of cooling time, where $a_{DTM}(0)$ and $a_{KN}(0)$ are initial activity values for DTM and Key Nuclide (KN).

$$SF(t_c) = \frac{a_{DTM}(t_c)}{a_{KN}(t_c)} = \frac{a_{DTM}(0) \times exp\left(-\frac{ln(2)}{T_{1/2}^{DTM}} \times t_c\right)}{a_{KN}(0) \times exp\left(-\frac{ln(2)}{T_{1/2}^{KN}} \times t_c\right)}, \tag{3.2}$$

where $a_{DTM}(t)$ and $a_{KN}(t)$ are the activities of the DTM and KN respectively at the cooling time t. $T_{1/2}^{DTM}$ and $T_{1/2}^{KN}$ represent the half-lives of the radionuclides. We can indicate three main cases for Equation 3.2; the $T_{1/2}^{DTM}$ is either greater than $T_{1/2}^{KN}$ or lower than $T_{1/2}^{KN}$ or the half-lives of these radionuclides are similar. the following Figures 3.4 and 3.5 show the behaviour of the analytical scaling factors of H-3 and Co-60 or Fe-55 and Co-60 for a waste made of steel.

Example 4 *This example illustrates the behaviour of the SFs as a function of the cooling time. The irradiation conditions of the simulation are the following. The irradiation span for Steel 304L is 10 years, the cooling time varies from 1 years up to 30 years for different positions in the accelerator. Additionally, we include a scenario right after the end of irradiation.*

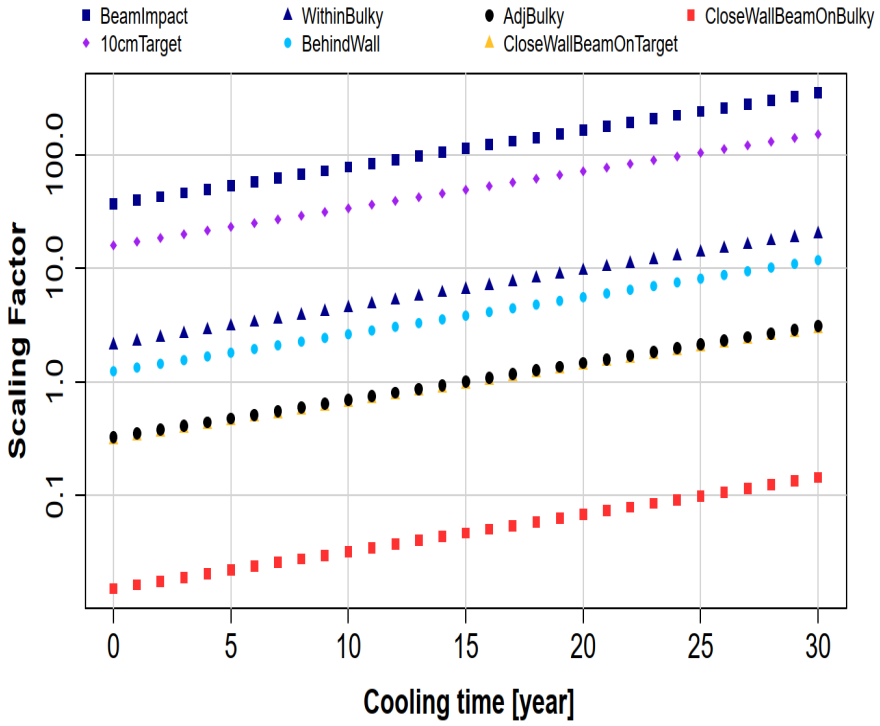

Figure 3.4: Illustration of analytical scaling factors for pairs of radionuclides H-3 and Co-60.

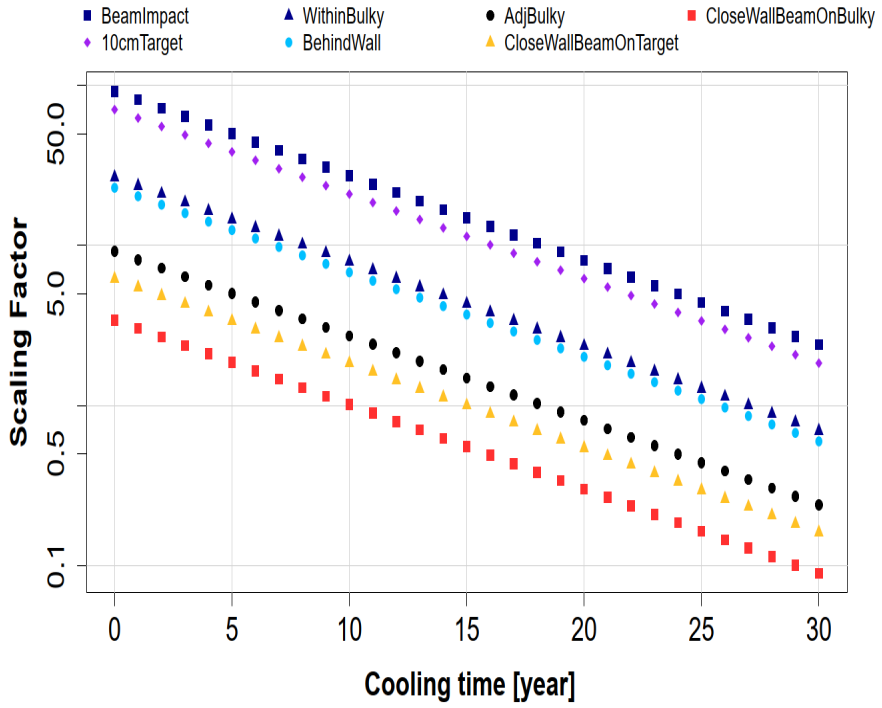

Figure 3.5: Illustration of analytical scaling factors for pairs of radionuclides Fe-55 and Co-60.

When the DTM half-life is greater than the KN value, the SF increases steadily as a function of the cooling time. For a pair of radionuclides H-3 and Co-60 the SF can reach a factor of 350 after 30 years of decay time. Conversely, the half-life of the Fe-55 is lower than the KN,Co-60. Hence, the SF is decreasing steadily as a function of cooling time. Additionally, H-3 and Co-60 SF values can vary maximally by four orders of magnitude due to different positions in the accelerator.

3.3 Experimental methods

As indicated in Section 3.1, the experimental methods deployed at CERN are either non-destructive or destructive. The non-destructive technique is based on direct measurement of waste items using gamma-spectrometry instrumentation. The concept of gamma-spectrometry is presented in Section 3.3.2. Conversely, to be able to estimate the radioactivity of difficult to measure radionuclides, we apply destructive methods, described in Section 3.3.3.

3.3.1 Interaction of radiation with matter

This section provides a basic introduction of the interactions of charged particle and of electromagnetic photons with the active volume of the detector. The objective of this sub-section is to briefly describe the detection mechanisms. [85].

3.3.1.A Charged particle interactions

During the radioactive decay of activated matter, the particles or photons (including gamma rays and X-rays) are emitted and can interact with matter. Each interaction of charged particles may cause the loss of its kinetic energy. The energy transfer from charged particles to the orbital electrons of matter results in collision losses. Whereas the energy transfer of charged particles to the nuclei results in radiative losses [102] The main interactions with matter involving electrons are ionization, excitation and Bremsstrahlung [109].

1. **Ionization** is a process where the orbital electron(s) is (are) removed from an atom, due to Coulomb interactions between the incident electron and orbital electron(s) of the matter.

2. **Excitation** involves the energy transfer from the incident electron to an orbital electron. The energy transfer is less than the binding energy of the orbital electron. This results in moving the orbital electron into a higher energy state rather than ejecting it from the atom.

3. **Bremsstrahlung** occurs when either an accelerated or a decelerated charge particle is deflected by another charged particle, mainly an atomic electron. A kinetic energy loss of the deflected particle varies from zero up to its total kinetic energy and it is converted to electromagnetic radiation (Bremsstrahlung radiation). The probability of this interaction is inversely proportional to the square of mass of the charged particle. Consequently the bremsstrahlung production is typically neglected for charged particles other than electrons and positrons.

3.3.1.B Photons electromagnetic interactions

This sub-section reviews the various types of electromagnetic interactions of photons with matter. Photons are considered indirectly ionizing radiation. They deposit their energy in matter in

two stages [103];

1. Energy is transferred to a charged particle;

2. The charged particle deposits its energy in matter.

Low energy photons interact with orbital electrons while those of higher energy interact with atomic nuclei. Figure 3.6 illustrates the representation of the most probable interaction mechanisms, such as photoabsorption, Compton scattering and pair production.

1. **Photoelectric absorption** is dominant at low photons energy. This effect occurs when the photon interacts with an inner shell electron of an atom. The photon transmit its all energy to the electron. It results in the absorption of the incident photon and the ejection of an orbital electron. The photoelectric absorption probability τ is proportional to $Z^n/E_\gamma^{3.5}$, where the exponent n varies between 4 and 5 for atomic number Z [82].

2. In **Compton scattering** the incident photon transfers only some of its initial energy to the orbital electron. This causes the scattering of the photon by an angle, with respect to its original direction. The Compton scattering probability σ is almost independent of atomic number Z and decreases as the photon energy increases.

3. **Pair production** can occur when the energy of the photon exceeds 1.022 MeV. In pair production, the photon is converted into an electron-positron pair. The positron originating from pair production combines with an electron in matter. The annihilation of the matter electron with the positron produces two photons of 511 keV each that emit in opposite directions. The pair production probability κ increases with atomic number roughly as Z^2.

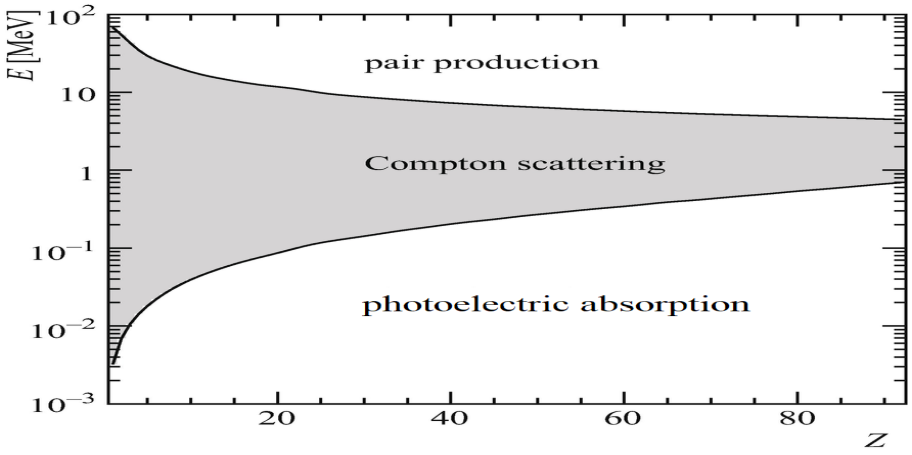

Figure 3.6: Representation of the relative predominance of the three main photon interactions with matter: photoelectric absorption, Compton scattering and pair production as a function of photon energy and atomic number Z [40].

3.3.2 Non-destructive assay technique of the waste: Gamma spectrometry

There are several non-destructive analysis techniques to evaluate the radioactive characteristics of the waste. One of them is gamma spectrometry, which allows identification of radionuclides and their corresponding activity concentrations [71].

Gamma-spectrometry is commonly used to measure the activity of ETM, gamma emitting radionuclides, such as Co-60, Na-22, Mn-54 etc..

The emitted gamma-rays interact with the High Purity Germanium (HPGe) detector. The major interactions leading to the complete or partial transfer energy of gamma-rays are photoabsorption, Compton scattering and pair production (detailed description of each phenomenon can be found in Section 3.3.1) [82].

The probabilities of occurrence of each iteration are shown in Equation 3.3. The sum of these probabilities μ refers to the total attenuation coefficient for gamma-rays interacting with matter.

$$\mu = \tau(photoelectric) + \sigma(Compton) + \kappa(pair). \tag{3.3}$$

In practice, the most useful coefficient is the mass attenuation coefficient. It is defined as a ratio of the total attenuation coefficient μ to the density ρ of the sample [67].

The attenuation principle for gamma rays is described by the following Equation 3.4, where *t* represents the thickness of the material.

$$\frac{I}{I_0} = e^{-(\mu/\rho)\cdot\rho t}. \tag{3.4}$$

The increase of the sample thickness has an impact on the shape of the acquired spectrum. Actually, due to scattering in the sample, the emitted gamma rays loose their energies, which result in a build-up of the Compton continuum of the spectrum. This is more noticeable at lower energies because low-energy gamma-rays are more easily attenuated than high-energy rays. Thus, the ratio of the low-energy photopeak area to the continuum under the peak is reduced [12].

Therefore, the formula shown in Equation 3.4 is replaced by the following:

$$\frac{I}{I_0} = B(t, E_\gamma)e^{-(\mu/\rho)\cdot\rho t}. \tag{3.5}$$

The build-up factor, $B(t, E_\gamma)$ given in Equation 3.5 depends both on the thickness, t of the sample and the energy of the gamma-ray, E_γ.

297 The radioanalytical laboratory at RWTCS is equipped with five ISOCS characterized HPGe, ei-
298 ther fixed or portable detectors. They are manufactured by MIRION Technologies (Canberra)[16].
299 The portable detectors Falcon 5000[17] are frequently used in the radiological characterization
300 process for the elimination of radioactive waste at CERN as well the assessment of the radio-
301 logical risk of material and equipment exiting designated areas. Figure 3.7 [18] depicts the Falcon
302 5000 placed in the dedicated laboratory while acquiring data and its corresponding layout.

Figure 3.7: Falcon 5000 detectors with the readout electronics during acquisition in the radioanalytical laboratory at RWTCS (left). The corresponding detector layout (right). A Geiger-Muller (GM) tube is included for monitoring of the dose rate. A moderated He-3 tube is dedicated to neutron measurements (optional). BEGe Technology Germanium Detector included in HPGe Falcon 5000 enhances the efficiency and resolution at low energies, while preserving a good efficiency in high energy range [31].

303 The following Sub-Sections present in detail the HPGe detector characteristics. Additionally,
304 Sub-Sections 3.3.2.E–3.3.2.I describe the software and corresponding spectroscopy algorithms,
305 used for reliable signal processing and gamma spectral analysis.

306 3.3.2.A Detector and electronics setup

307 The HPGe detector is a high energy resolution detection system commonly used in radioan-
308 alytical laboratories and facilities. The gamma-rays ionize the depleted region of the crystal,
309 generating electron-hole pairs. Due to the fact that a high voltage is applied to the semiconduc-
310 tor, the created electron-hole pairs follow the electric field lines. Hence, they can be collected at
311 the electrodes. The generated charges are then collected by the integral charge-sensitive pream-
312 plifier then processed by the readout electronics. The readout electronics include an integrated
313 Multi-Channel Analyzer (MCA) that digitizes the data from the preamplifier output of the de-
314 tector. Specific digital processing algorithms are applied to the digitized data to perform sig-
315 nal shaping, amplification and generation of the acquisition spectrum. The collected spectrum

[16] https://www.mirion.com/, 9 February 2021
[17] https://www.canberra.com/fr/produits/hp_radioprotection/falcon-5000.html, 9 February 2021
[18] https://mirion.s3.amazonaws.com/cms4_mirion/files/pdf/spec-sheets/falcon-portable-hpge-based-identifier.pdf?1557257239, 9 February 2021

is then transferred and saved in a file (*.cnf) with proprietary format from Mirion Technologies (Canberra). The spectrum is then analyzed and processed by the dedicated gamma spectroscopy algorithms made available by the APEX-Gamma productivity suite integrated with Genie 2000[19].

Figure 3.8 shows the block diagram of the electronic setup for HPGe measurement station.

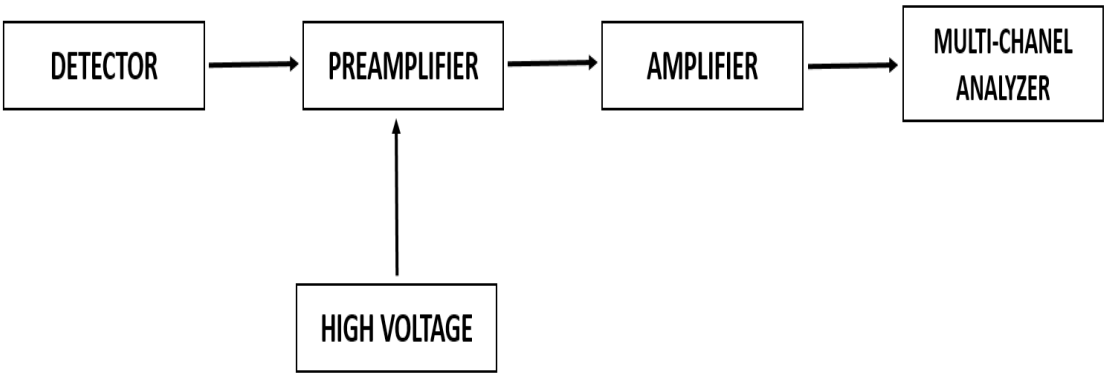

Figure 3.8: A schematic of the simplified electronic system of a gamma spectrometry acquisition station. Adapted from [67].

A reverse-biased high voltage is delivered to the detector via the preamplifier to extend the depleted region of the crystal. Due to the low energy gap in germanium semiconductors, to guarantee the equilibrium between thermal excitation and ionizing radiation that both create electron-hole pairs in depleted region of the crystal, the HPGe detector has to be maintained at low temperatures. Typically, the HPGe detector is cooled down using liquid nitrogen, which has a temperature of 77 K (for fixed detectors), or purely electrical cooling systems (such as Falcon 5000) [31].

The preamplifier is the interface between the detector and the integrated spectroscopy amplifier within the MCA. It collects the charges and converts them into a voltage pulse [32]. The primary function of the amplifier is pulse shaping and matching the dynamic range for the MCA input (detailed description of the functions of the amplifier can be found in [67]).

The height of the integrated pulses from the amplifier is linearly proportional to the sum of created electron-hole pairs produced by the ionizing radiation and consequently to the deposited energy of the interacting particle. This signal is transferred to the MCA, which measures, sorts the heights of pulses and counts them within small voltage ranges or channels. The output of the signal processing step is the histogram containing the number of pulses with energy deposition pertaining to the corresponding channel.

[19] https://www.mirion.com/products/genie-2000-basic-spectroscopy-software, 1 June 2021

The main function of the MCA in a typical gamma spectrometry system is to allow the identification of the radionuclide present in the sample by measuring the height of the pulses and estimating the corresponding activity by counting the number of those pulses. [82].
The APEX-Gamma software utilizes Genie 2000 components for displaying spectra, performing energy, shape and efficiency calibrations, editing nuclide libraries to perform the necessary analysis steps on the collected spectral files [94]. These steps include peak search, Peak area calculations, background subtractions, efficiency calibrations and nuclide identifications and quantifications, Minimum Detectable Activity (MDA) calculations as well as reporting functionalities [24].
Table 3.6 depicts specifications of the Falcon 5000 detector of the radioanalytical laboratory at RWTCS.

Table 3.6: Detector specification and measured performance of Falcon 5000 [93].

Isotope	Co-57	Co-60	Fe-55	Co-57[a]	Cd-109	Cd-109	Cd-109 Ratio
Energy [keV]	122	1332	5.9	6.4	22	88	22:88
FWHM[b] [keV]	0.829	1.657			0.829	0.850	
FWTM[c] [kev]	1.580	3.007			1.580	1.565	
Peak/Compton/Continuum		54.0:1					8.3:1
Efficiency %		22.5					

[a] Substitutes for Fe-55 in some cases where Fe-55 peaks are not well separated
[b] Full Width at Half Maximum
[c] Full Width at Tenth Maximum

3.3.2.B Spectral features caused by interactions in the detector

Photon interactions (see Section 3.3.1)with the detector result in creation of electron-hole pairs, that are source of charge carriers (electrons and holes) in the detector. Those collected carriers cause the preamplifier to produce voltage pulses, whose amplitudes are proportional to the number of electrons and holes collected. Consequently, the number of charged pairs created and collected defines the channel that is incremented. The number of charge pairs collected is proportional to the deposited energy in the detector.
Spectral features caused by events, which occur within the detector are namely [67]:

1. The full energy of the photon is deposited in the detector when the photon undergoes photoelectric absorption. Thus, photoelectric absorption is an ideal process because deposited energy corresponds to the number of count in the full energy peak.

2. Transferred energy to the electron in the collision with incident photon ranging from zero up to maximum predicted by Equation 3.6

$$E_e = \frac{E_\gamma^2}{E_\gamma + \frac{0.511}{1 - \cos\Theta}} \tag{3.6}$$

For a scattering angle of $0°$, the energy transferred to the electron is zero, while for scattering angle $180°$, the energy transferred to the electron is maximum (E_{emax}). The high energy edge of the distribution of Compton continuum that corresponds to the E_{emax} is called a Compton edge.

The multiple Compton events refer to photons that undergo multiple Compton scattering events before escaping from the detector. The energy deposited might be greater than energy corresponding to the Compton edge, but less than the energy of the initial photon.

3. If the incoming photon has energy greater than 1.022 MeV it may produce an electron-positron pair in the detector. The energy deposited in the detector is given by Equation 3.7,

$$E_{pair} = E_\gamma - 1.022MeV. \tag{3.7}$$

The positron originating from pair production deposits energy in the detector and finally combines with an electron in matter in a process of annihilation. The photons resulting from the annihilation process, can both deposit their full energy in the detector. If one of the annihilation photons escapes the detector, then the energy deposited in the detector is [E_γ- 0.511] MeV, which is called the single escape peak (SEP). If both annihilation photons escape the detector, then the energy deposited in the detector is [E_γ- 1.022] MeV. The peak that develops at [E_γ- 1.022] MeV is the double escape peak (DEP).

3.3.2.C Spectral features caused by interactions external to the detector

There are also spectral features caused by interactions external to the detector, including [82]:

1. X-ray fluorescence peaks are caused by the photoelectric absorption in the material surrounding the detector. The inner electron is ejected from the atom. The created vacancy is filled by a higher shell electron, resulting in the emission of a characteristic X-ray. The detection of this X-ray causes a peak to occur in the spectrum, typically less than 105 keV. X-rays may also be detected as a result of electron capture or internal conversion in the source.

2. Backscatter peak is caused by the detection of photons that have undergone a large angle scattering event (Compton scattering) prior to interacting with detectors.

3. Annihilation peak caused by pair production in the surrounding material. The annihilation photons may strike the detector causing a (full energy) peak to occur at 511 keV (the annihilation peak).

3.3.2.D Spectral features and dead time caused by count rate

Section 3.3.2.D depicts the counting rate effects on the acquired spectra and corresponding the dead time behaviour. In the case of low counting rates, the average time between arising pulses is long enough compared to the intrinsic resolving time of the electronics. The generated primary pulse has enough time to regain the processing signal baseline and hence it does not influence the amplitude of the next one. When the counting rate increases, pulses may not have returned to the baseline yet when the following pulses appear or are processed by the electronics. Such situations result in random signals summing and are referred to as pulse pile-up [8].

The random summing is the consequence of two or more gamma rays that might occur simultaneously within the resolving time of the detector electronics circuit [67] . In this case, we do not observe two individual detection events but rather a single pulse with a pulse height equal to the sum of these two individual events.

Figure 3.9 presents a sequence of Cs-137 gamma ray spectra that demonstrate the effect of increased counting rates on the spectra shapes and features.

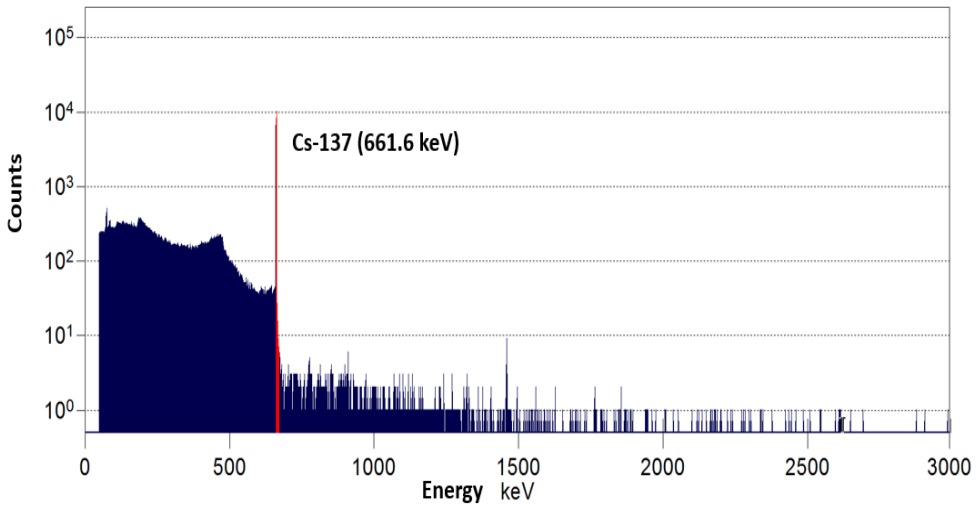

(a) A Cs-137 spectrum accumulated at a relatively low counting rate. The dead time is 4%. The distance source-detector is 4 m, where the registered dose rate at the detector is 1.2 μSv/h for the activity of 300 MBq. Random summing is not observed. The Input Count Rate (ICR) is 2.4×10^3.

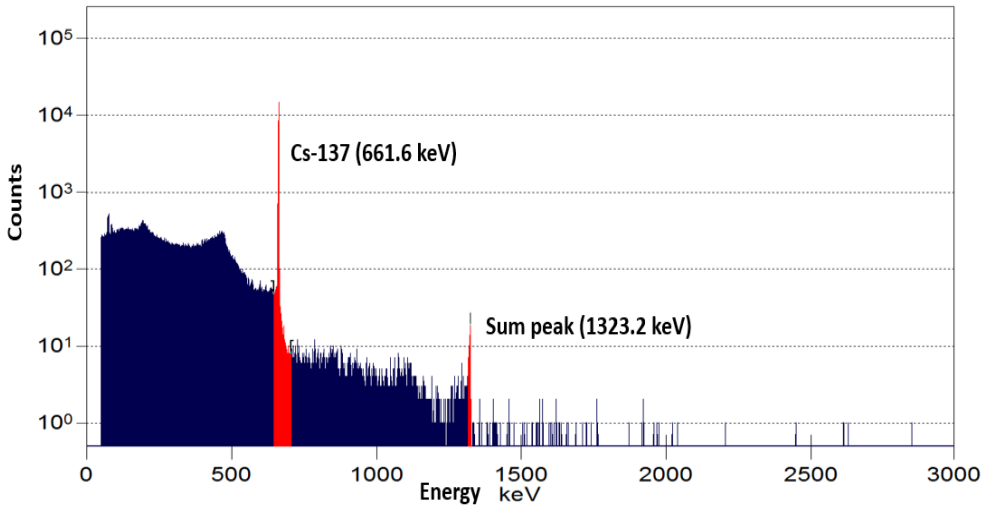

(b) A Cs-137 spectrum accumulated at a relatively medium counting rate. The dead time is 30%. The distance source-detector is 1.5 m, where the registered dose rate at the detector is 9.5 μSv/h for the activity of 300 MBq. The ICR is 2.5×10^4.

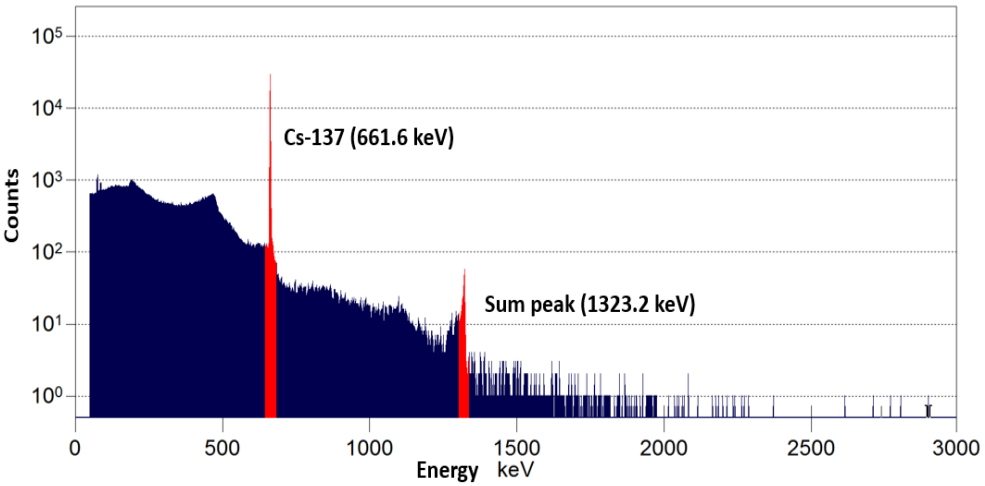

(c) A Cs-137 spectrum accumulated at a relatively high counting rate. The dead time is 55%. The distance source-detector is 1 m, where the registered dose rate at the detector is 18 μSv/h for the activity of 300 MBq. The ICR is 5.3×10^4.

Figure 3.9: The summing effect is observed for two acquisitions of Cs-137 source. A summing peak is at 1323.2=2 · 661.6 keV. For the Cs-137 spectrum taken at a relatively low counting rate, the summing effect is negligible, while the dead time is low 4% as shown in Figure (a).

The energy resolution of a gamma ray peak is optimal for low counting rates. Experiments show that the Full Width Half Maximum (FWHM) increases with increasing counting rates [27].

The gamma spectroscopy measurements carried out in the Calibration Hall at CERN demonstrate the increase of FWHM with increasing counting rates. The measurement setup is shown in Figure 3.10. The acquisitions are performed using the Falcon 5000 detector and a 300 MBq Cs-137 source.

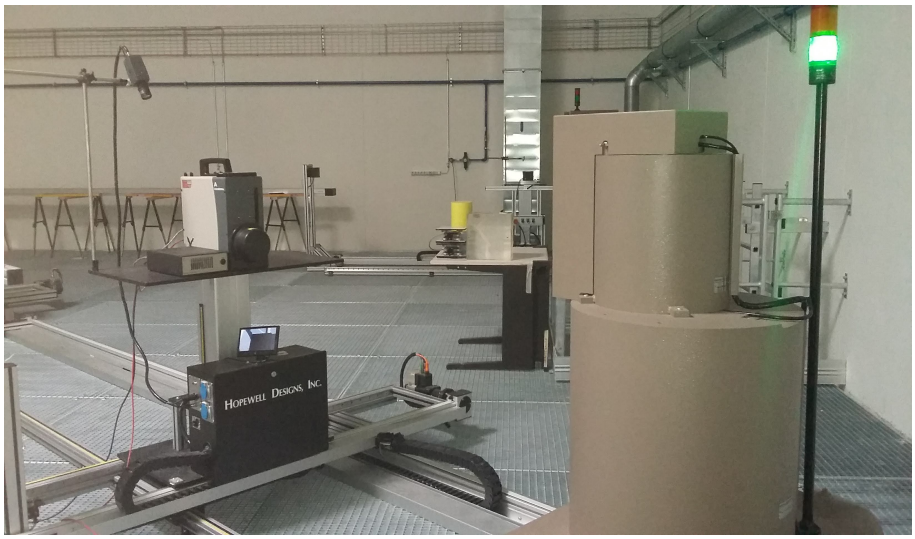

Figure 3.10: The interior of the Calibration Hall. Measurements performed using the Falcon 5000 detector. The measurements are fully driven from the control room, for dose exposure optimization and reduction.

Figure 3.11 shows the average FWHM at 661.6 keV for a Cs-137 source as a function of the corresponding Input Count Rate (ICR). The FWHM varies between 1.48 keV (for the ICR equal to 1.9×10^3) and 1.66 keV (for the ICR equal to 8.3×10^4). The corresponding uncertainties of the mean values are given at 1 σ, both for FWHM and ICR.

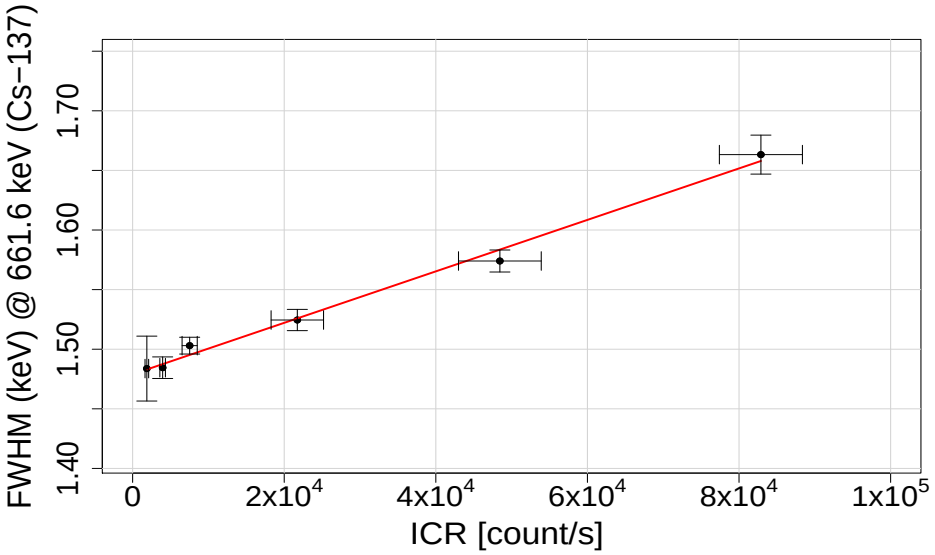

Figure 3.11: FWHM at 661.6 keV for a Cs-137 source as a function of the corresponding ICR using the Falcon 5000 detector. The FWHM spans an interval of approximately 0.2 keV when the ICR increases by one order of magnitude.

In addition, [96] show the FWHM behaviour for various rise times in the case of the Trapezoidal filter. In the electronic setup used in this study, the Falcon 5000 detector Rise Time was set to 5.6 μsec.

Dead time denotes the minimum time interval that is needed to separate two incoming gamma rays to be recorded as two separate pulses by the detector electronic circuit [8]. The gamma spectroscopy acquisition should include dead time correction especially for relatively high counting rates. The correction consists of measuring the dead time by the analyzer electronics and extending the acquisition time accordingly.

The outcome counting rate can be quantified by taking into account a dead time of a given length and model. The dead time behaviour may be determined using Equation 3.8, where m and n represent the recorded count rate and the true interaction rate respectively.

$$deadtime(\%) = \frac{n-m}{n} \times 100\%. \tag{3.8}$$

The common models that represent a dead time behaviour of a counting system are paralyzable and nonparalyzable [82]. For the paralyzable model, true events that occur during the dead time period are not detected as counts, however they are assumed to extend the dead time by another period δ. A paralyzable model can be formulated by the following Equation 3.9, where m is the recorded count rate, n is the true interaction rate (referred as ICR), and δ is the system dead time parameter.

$$m = n \cdot exp(-n \cdot \delta). \tag{3.9}$$

After modification of Equation 3.9 the dead time behaviour as a function of ICR could be as follows,

$$deadtime(\%) = 100\% \cdot [1 - exp(-\delta \cdot ICR)]. \tag{3.10}$$

On the other hand for the nonparalyzable model, the fraction of time when the electronics cannot process pulses (i.e. dead) is fixed. The formula for the true interaction rate is given by Equation 3.11 where all parameters are mentioned before.

$$n = \frac{m}{1 - m \cdot \delta}, \tag{3.11}$$

Equation 3.12 shows a relationship of dead time and ICR,

$$deadtime(\%) = 100\% \cdot [1 - \frac{1}{(\delta \cdot ICR + 1)}]. \tag{3.12}$$

Figure 3.12 presents the dead time behaviour as a function of ICR with associated dead time models based on the the gamma spectroscopy acquisitions carried out in the Calibration Hall at CERN, as described before. The ICR values vary between 4×10^2 and 9.6×10^4.

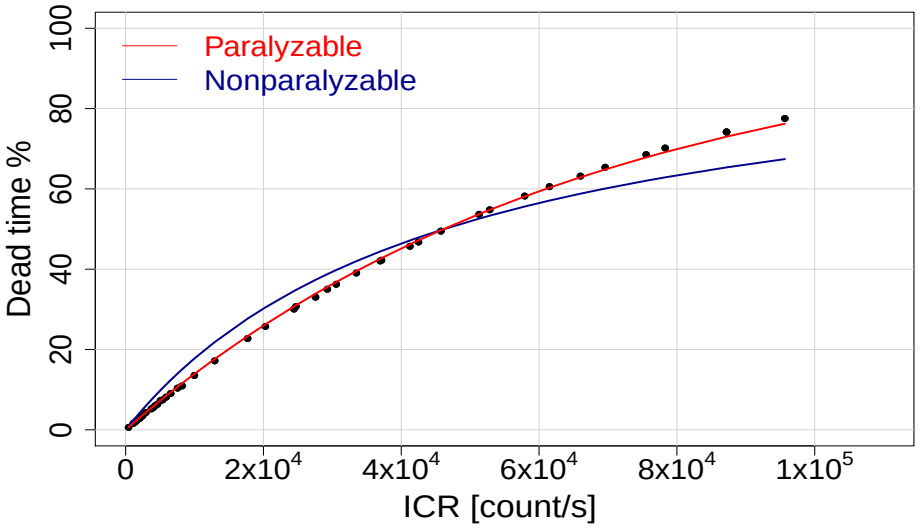

Figure 3.12: The dead time behaviour as a function of ICR with associated paralyzable and nonparalyzable dead time models using Cs-137, Ba-133, and Co-60 sources. The system dead time parameter for the paralyzable and nonparalyzable models are; $\delta_{paralyzable}$ is 1.5×10^{-5} sec with standard error of 4.9×10^{-8} sec and $\delta_{nonparalyzable}$ is 2.2×10^{-5} sec with standard error of 7.3×10^{-7} sec.

For the operational gamma spectrometry measurements of radioactive waste items, we carried out dose rate and dead time measurements at the location of the Falcon 5000 detector and for different distances. The objective is to design a counting geometry that minimises dead times. In order to fulfil this requirement, we need to take into account the available space in the facility (maximizing the item-to-detector distance) during the acquisitions while maintaining MDA that are at least 10% of the VLL declaration thresholds (see Section 2.3). Figure 3.13 shows the dead time as a function of the dose rate at the detector for 17 radioactive waste candidates with masses that range from a dozen kilograms up to several tons, as presented in Section 2.3.2.

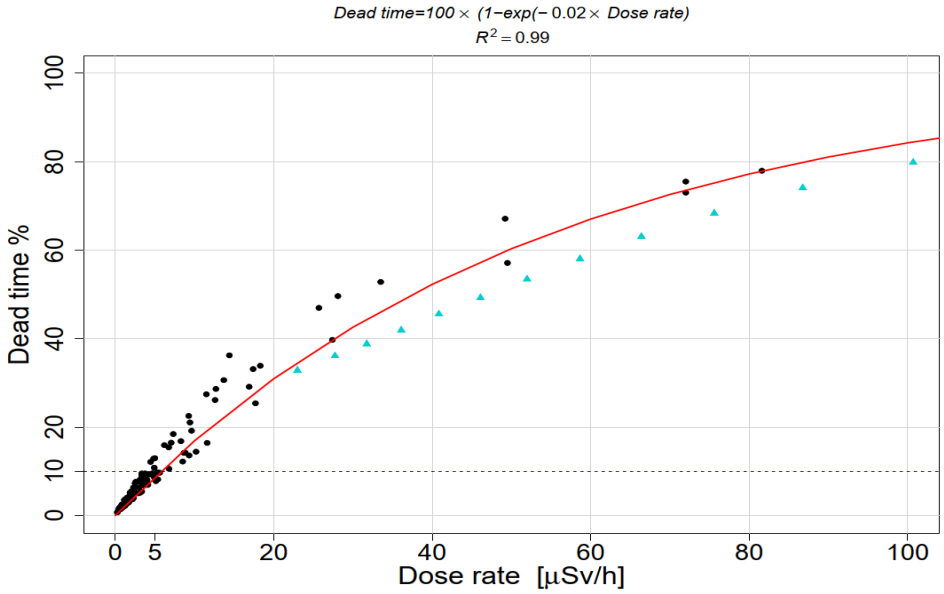

Figure 3.13: The dead time behaviour as a function of dose rate for waste candidate items (black dots) and calibration Co-60 source (cyan triangles).The dead time equal to approximately 10 % that corresponds to dose rate at 5 μSv/h. The red curve represents the fit of the data points.

As it can be seen from Figure 3.13, identical dose rate values could lead to different dead time values. This shows the impact of the item (or source) geometry on the dead time behaviour, such as attenuation, emitted gamma ray energies, scattering, source volume and position. Figure 3.13 shows that dose rates that are due to a point source (Co-60), lead to lower dead time values than the waste items, whose main activity is due to Co-60. The scattering in the waste item has a higher probability to generate more ICR in the detector, which explains the higher dead time values for the waste item geometries.

We also should note that the dead time increases for increasing shaping times (both the Rise Time and the Flat Top) [82].

3.3.2.E Peak areas

A peak occurs in the acquired gamma spectroscopy spectrum when a process repeatedly deposits the same amount of energy in the detector. The net peak area for a single peak at energy E_γ is a measure of the number of full deposition events of energy E_γ. The net peak area S is calculated as follows (Equation 3.13).

$$S = G - B \tag{3.13}$$

where G is the sum of the number of gross counts in the peak Regions Of Interests (ROI), $\sum_{i=1}^{N} y_i$ where y_i is count per channel in channel i. B represents the continuum distribution under the peak caused by events other than one that repeatedly deposit energy E_γ. This continuum can be modelled by a step function. The step background model is presented in Figure 3.14.

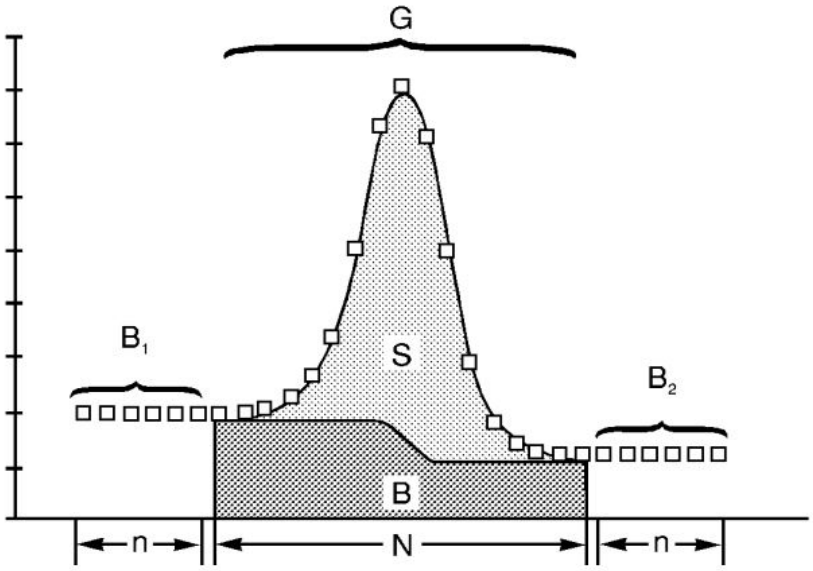

Figure 3.14: A step continuum. The background is assigned to each channel in proportion to the fraction of the total integral that lies under the curve from the first channel of the peak ROI to channel i. [24]

Equation 3.14 provides an expression of the background B.

$$B = \sum_{i=1}^{N} \left(\frac{B_1}{n} + \frac{B_2 - B_1}{nG} \cdot \sum_{j=1}^{i} y_j \right). \tag{3.14}$$

where y_j is count per channel in channel j, N is the number of channels in the peak ROI, n is the number of continuum channels on each side, B_1 and B_2 represent either the sum of n channels immediately to the left or to the right of the peak region.

Following the general concept represented by Equation 3.13, the net peak area is calculated from step background model in Equation 3.15,

$$S = \sum_{i=1}^{N} y_i - \sum_{i=1}^{N} \left(\frac{B_1}{n} + \frac{B_2 - B_1}{nG} \cdot \sum_{j=1}^{i} y_j \right). \tag{3.15}$$

3.3.2.F Efficiency calibration

The efficiency calibration describes the relationship between the number of peak counts in the spectrum and the nuclide disintegration rate [67]. The measurement of a gamma ray emission rate requires the knowledge of the HPGe detector efficiency at energy of the emitted gamma ray. The absolute total efficiency of the detector is given by [68]

$$\epsilon_{total} = \frac{\text{total number of counts recoreded in time t}}{\text{number of quanta emitted by the source in time t}}. \tag{3.16}$$

This takes into account the full energy peak and all incomplete energy depositions represented by the Compton continuum [20].

In gamma spectrometry, the intention is to associate the measured peak area of the spectrum with an identification and quantification of radioactivity present in the sample. The absolute full energy peak efficiency is expressed by

$$\epsilon_{peak}(E) = \frac{\text{number of counts recoreded in the peak at a particular energy in time t}}{\text{number of quanta emitted by the source in time t}}, \quad (3.17)$$

$\epsilon_{peak}(E)$ depends on the sample and the detector geometries, as well as the energy of the gamma rays [82].

Within the scope of this thesis, a dedicated efficiency calibration is performed for each waste (either unitary item, container or sample) using a mathematical calibration software In Situ Object Counting System (ISOCS) [6] without using radioactive standards at the laboratory. The efficiency response profile of each specific detector, to be used with the ISOCS software, is characterized at the factory using NIST-traceable sources and the MCNP Monte Carlo modelling code. The response profile of each individual detector in free space (vacuum with no attenuation) is determined for a 1000 m diameter sphere around the detector covering an energy range from 10 keV to 7 MeV. In the ISOCS software, the characterized detector is selected from a list of available detectors. The ISOCS algorithm mathematically calculates peak efficiency values using a characterized detector model that is validated with measured efficiency values. The measured peak efficiency at a given energy $\epsilon_{peak}(E)$ is defined in Equation 3.18

$$\epsilon_{peak}(E) = \frac{S}{T \cdot y \cdot A \cdot K_w}, \quad (3.18)$$

where S is the net peak area of the calibration peak, T is the acquisition time, y is the yield of the emitted gamma ray, A is the source activity at the reference time. K_w is the decay correction factor to account for radionuclide decay between the activity A reference time and the source acquisition time.

In order to generate the efficiency curve calibration, one needs to know the physical and geometry parameters of the object, such as dimensions, material elemental composition, densities and relative activity concentrations. Some of those parameters are well known and do not vary considerably. However, some other parameters are not-well-known, e.g., the activity distribution within the material matrix. For each not-well-known parameter, the user needs to provide an estimate of the parameter's variation intervals or values; e.g., by measuring a group of containers or consulting the manufacturer specifications for the containers or simply making educated guesses. These not well-known parameters contribute to the uncertainties of the calibration efficiency values at each energy.

[20] If the incident gamma ray energy is below the value at which pair production is significant, the spectrum results from the combined effect of Compton scattering and photoelectric absorption. The continuum of energies corresponding to Compton scattered electrons is called Compton continuum [82].

To generate the reference ISOCS calibration curve, we use the known physical parameters, such as the dimensions of the item, and the material composition. The corresponding ISOCS geometry parameters of the waste with a three dimensional rendering of a representative geometry are shown in Figure 3.15.

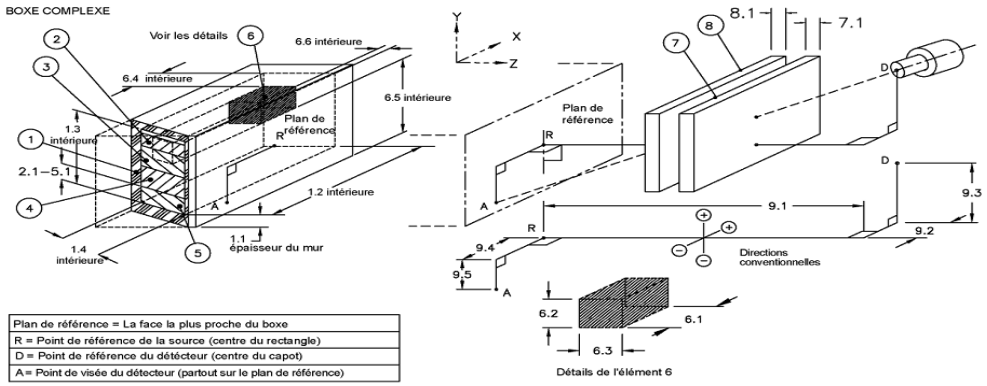

(a) Template drawing of the Complex Box.

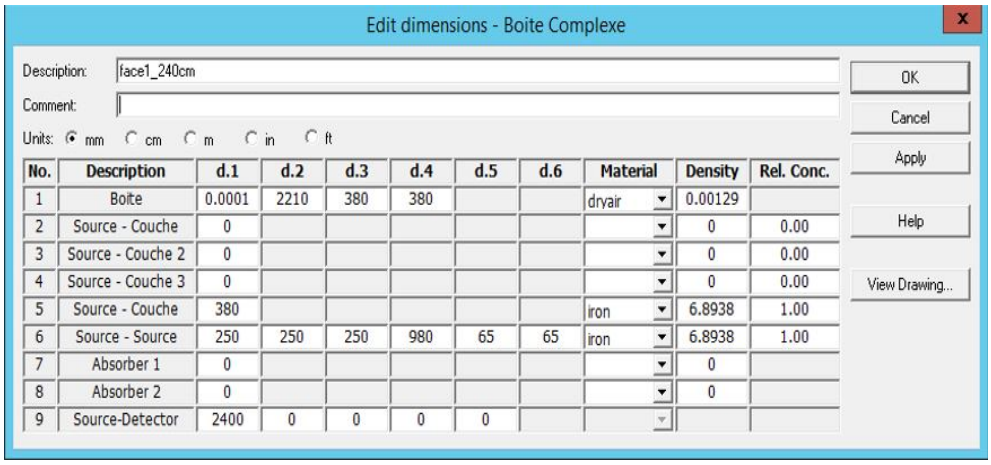

No.	Description	d.1	d.2	d.3	d.4	d.5	d.6	Material	Density	Rel. Conc.
1	Boite	0.0001	2210	380	380			dryair	0.00129	
2	Source - Couche	0							0	0.00
3	Source - Couche 2	0							0	0.00
4	Source - Couche 3	0							0	0.00
5	Source - Couche	380						iron	6.8938	1.00
6	Source - Source	250	250	250	980	65	65	iron	6.8938	1.00
7	Absorber 1	0							0	
8	Absorber 2	0							0	
9	Source-Detector	2400	0	0	0	0				

(b) ISOCS parameters panel

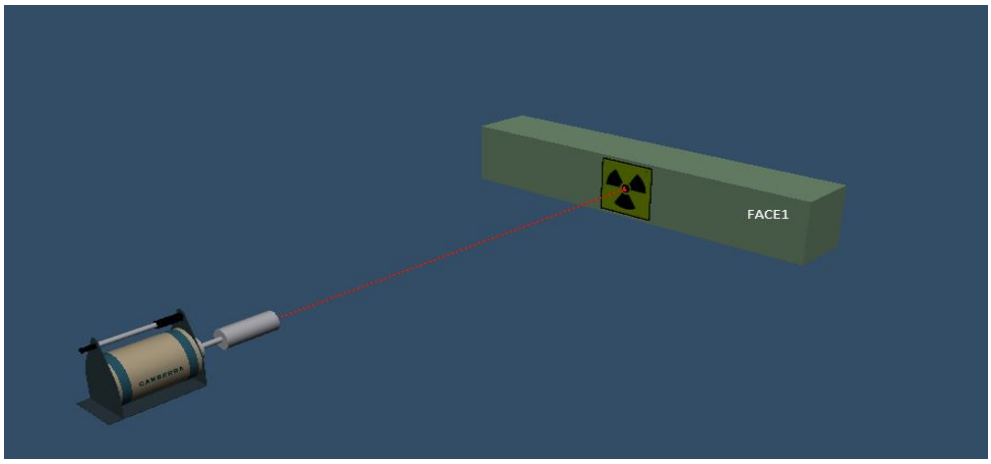

(c) A three dimensional visualization of modelled geometry.

Figure 3.15: Efficiency calibration geometry parameters for the reference model using Complex Box template for a waste item.

515 Based on the geometry input file, as seen in Figure 3.15, the calculated efficiencies for the
516 selected energies are presented in Figure 3.16

```
SGI_template: COMPLEX_BOX
ISOCS_file_name: L_max_face1_240cm_5.gis
Detector_name: FALCON2
Collimator_name: no_collimator

Convrgence_[%]: 1.0000
Test_description: FACE1_240CM
Comment:
Date_Time: Wed_Apr__1_21:10:33_2020
Source_area_cm2:  8.39800e+3
Source_grams:  2.19998e+6


keV_eff_%err:    45.00   2.87625e-8  10.0
keV_eff_%err:    50.00   4.14178e-8  10.0
keV_eff_%err:    60.00   7.48610e-8  10.0
keV_eff_%err:    70.00   1.16582e-7  10.0
keV_eff_%err:    80.00   1.65105e-7  10.0
keV_eff_%err:    90.00   2.15072e-7  10.0
keV_eff_%err:   100.00   2.65968e-7  10.0
keV_eff_%err:   110.00   3.15237e-7  10.0
keV_eff_%err:   120.00   3.59790e-7  10.0
keV_eff_%err:   150.00   4.51224e-7  10.0
keV_eff_%err:   200.00   4.88091e-7   8.0
keV_eff_%err:   300.00   4.23634e-7   8.0
keV_eff_%err:   400.00   3.57529e-7   8.0
keV_eff_%err:   600.00   2.86074e-7   6.0
keV_eff_%err:   800.00   2.47755e-7   6.0
keV_eff_%err:  1000.00   2.25174e-7   4.0
keV_eff_%err:  1132.00   2.14413e-7   4.0
keV_eff_%err:  1173.00   2.11626e-7   4.0
keV_eff_%err:  1500.00   1.91317e-7   4.0
keV_eff_%err:  2000.00   1.69190e-7   4.0
keV_eff_%err:  2500.00   1.49897e-7   4.0
keV_eff_%err:  3000.00   1.32476e-7   4.0
```

Figure 3.16: The reference ISOCS efficiency calibration points (in the red frame) with associated uncertainties generated for a waste item with energy range starting from 45 keV to 3 MeV.

517 Additionally, the graphical depiction of the reference ISOCS efficiency calibration points is
518 presented in Figure 3.17.

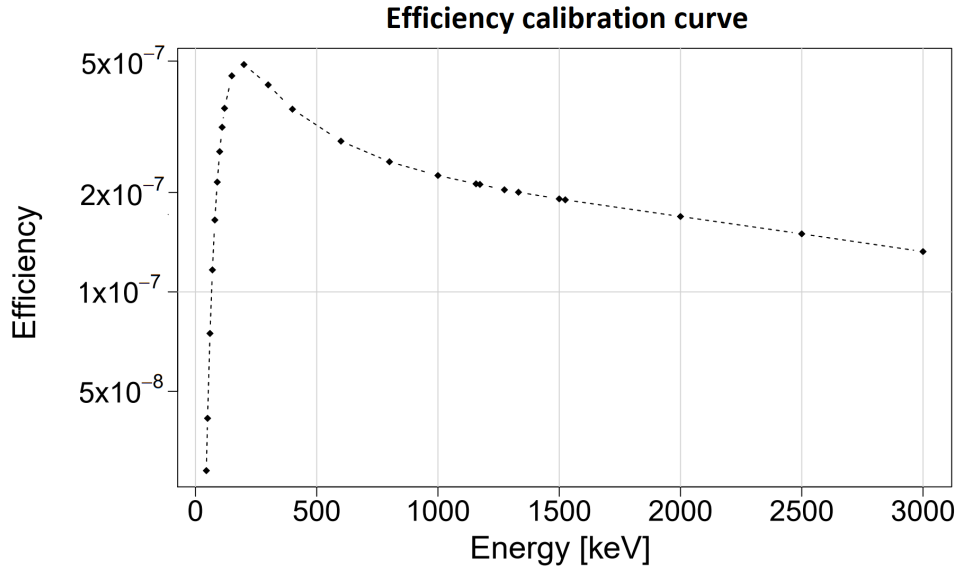

Figure 3.17: The reference ISOCS efficiency calibration curve for a waste item with energy range from 45 keV to 3 MeV.

519 ### 3.3.2.G ISOCS Uncertainty Estimator (IUE)

520 In order to estimate the uncertainties of the efficiencies due to the variation of the geometry
521 parameters, we refer to the ISOCS Uncertainty Estimator (IUE) [95][43][108]. As described
522 in Section 3.3.2.F, in order to generate the efficiency calibration curve, one needs to know the
523 physical and geometrical parameters of the object, such as dimensions and material elemental
524 composition. In order to account for the efficiency value variations due to the activity non
525 uniform distribution of the measured item, we introduce hot spots in the ISOCS model. The
526 objective is to associate to this hot spot other relative activity concentration values compared to
527 the rest of the item.
528 In the uncertainty qualification modelling process, one needs to vary the number of hot spots as
529 well as the relative activity concentrations. They might be constant (entry only "Minimum") or
530 variable (entry both "Minimum" and "Maximum"). In case of a variable number of hot spots, a
531 random number N of hot spots is generated assuming the uniform distribution within the limits
532 of the number of hot spots. Also, each hot spot is placed randomly within the item, e.g. any-
533 where in the defined layers, and has a different size that is generated between "Low" and "High"
534 values, which follows one of the sampling distribution types in IUE. In the randomization pro-
535 cess, each modeled variables follows one of the distribution type, such as [20]:

536 1. Uniform, where values between "Low" and "High" are equally probable;

537 2. Triangular, where the probability decreases linearly until values at "Low" and "High" reaches
538 zero;

539 3. Normal, where the user selects the confidence limit values.

Figure 3.18 shows the entered parameters that describe the amount and type of variations for the geometry model using the IUE software, for instance, the number of hot spots with their relative activity concentration and sizes.

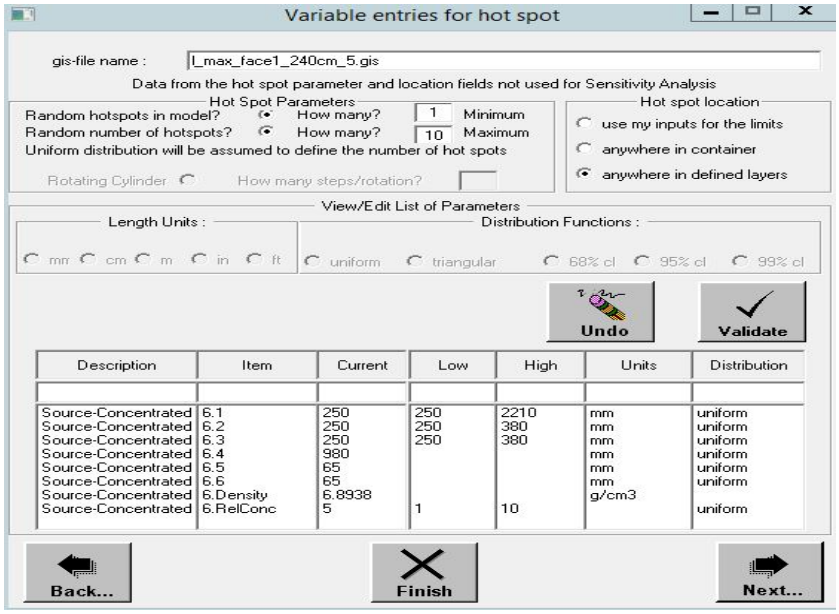

Figure 3.18: The entries for the hot spot parameter varied from 1 to 10 following a uniform distribution. Additionally, the relative activity concentration of the hot spot is generated using the uniform distribution within the limits [1,10].

The other feature of the IUE software is the simulation of multiple detectors that might be oriented opposite, facing, right and left to the item, as presented in Figure 3.19.

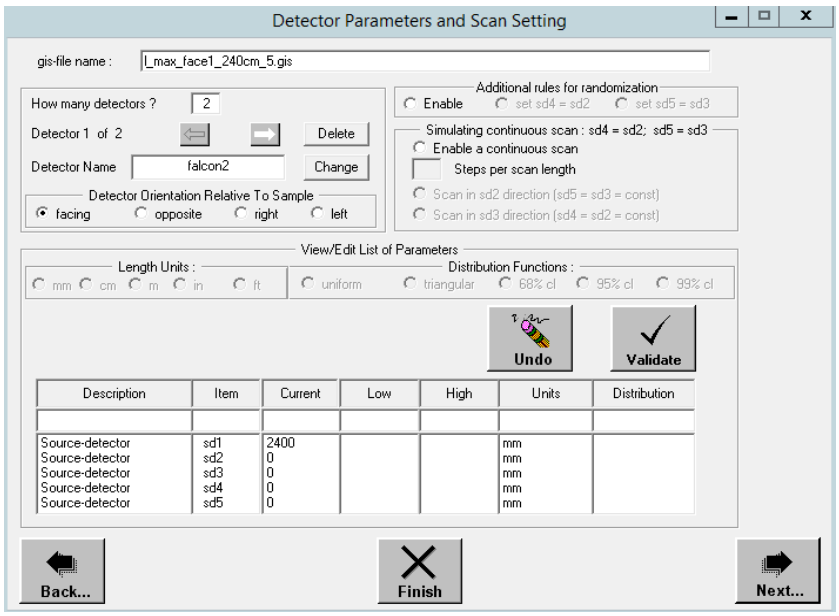

Figure 3.19: The detector parameters such as number, type, position and distance detector - source (item).

3.3.2.H Activity calculations

The net peak area S is proportional to the radioactivity value. However, in order to calculate the nuclide specific activity, it is necessary to correct the net peak area for the efficiency, yield of the emitted nuclide gamma ray y, mass of the sample m, the acquisition time T and decay correction factor K_w (see Section 3.3.2.F).
Hence, an approximate formula of the specific activity, at a given date and time, is given by Equation 3.19

$$\text{Specific Activity} = \frac{S}{\epsilon_{peak} \cdot T \cdot y \cdot m \cdot K_w}. \tag{3.19}$$

Equation 3.19 does not account for the decay during the acquisition time. If the acquisition time is a significant fraction of the half-life of the radionuclide being measured, this equation does not provide an accurate result. For such a situation, the correction factor for the radionuclide during the acquisition time, K_c should be included. The formula for the calculated specific activity at the beginning of the acquisition is given by [24]

$$\text{Specific Activity} = \frac{S}{\epsilon_{peak} \cdot T \cdot y \cdot m \cdot K_w \cdot K_c}. \tag{3.20}$$

Additionally, some identified radionuclides, within the sample, might emit gamma-rays at energies that cannot be resolved by the HPGe detector. Hence, the gamma ray spectrum will present peaks that can be attributed to one or multiple radionuclides. As an example, we could consider the case in which a sample contains Co-57, Se-75, and Hg-203. Table 3.7 presents the gamma-rays energies and corresponding intensities of these radionuclides.

Table 3.7: Examples of radionuclides with their energy peaks that can interfere.

Radionuclide	**Energy [keV]**	**Intensity [%]**
Co-57	122.06	85.60
	136.47	10.68
Se-75	121.12	17.20
	136.00	58.30
	264.66	58.90
	279.54	24.99
Hg-203	400.66	11.47
	279.20	81.46

In this case, the spectrum would contain 5 peaks centered around following values: 122, 136, 264, 279, and 400 keV. The 122 keV peak would be due to contributions from Co-57 and Se-75. Similarly, the 136 keV peak would be due to contributions from Co-57 and Se-75. The 264 and 400 keV peaks would be due to Se-75 only; while the 279 keV peak would be due to contributions from Se-75 and Hg-203. Hence, in order to account for this effect, one needs to add an interference correction to Equation 3.20 [24].

3.3.2.I Minimum Detectable Activity calculations

The estimation of the MDA values in the NDA technique is required in order to guarantee the ability of the NDA technique to measure activity values of ETM above the corresponding declaration thresholds [22]. Calculations of the MDA involve statistical methods of classical hypothesis testing [81]. There are two hypotheses: the detected signal originates from the blank observations or it is real. The expected statistical distribution in a counting process might be Normal for a sufficiently large number of counts. Therefore, we can establish the MDA at a specified confidence level for error probabilities α (false positives) and β (false negatives).
The MDA calculations for a given radionuclide, at the 95 $\%$ confidence level is based on Currie's derivation [53]. Currie's method is based on two concepts;

1. **Critical Limit** L_C is defined as the blank signal, which has a probability of 1- α not to be detected, given by Equation 3.21

$$L_C = k_\alpha \cdot \sigma_0, \tag{3.21}$$

   where σ_0 is a standard deviation of the blank signal distribution and k_α is the abscissas of the Normal distribution corresponding to the probability level 1-α . L_C depends on the fluctuation of the observed signal when the radioactive sample is not present (blank).

2. **Detection Limit** L_D is the smallest true signal, detected with 1- β probability, while having a probability of α that true blank signal is determined to be detected (above the L_C) as shown in Equation 3.22.

$$L_D = L_C + k_\beta \sigma_D, \tag{3.22}$$

   where σ_D is the standard deviation of the true signal distribution for L_D.

A common case where α and β values are both taken to be 0.05, then k_α= k_β=k=1.645. Then, the L_D expression cab be reduced to (see Equation 3.23)

$$L_D = k^2 + 2L_C = k^2 + 2k\sigma_0, \tag{3.23}$$

Equation 3.23 can be approximated as shown in Equation 3.24

$$L_D \approx 2.71 + 3.29\sqrt{2C} = 2.71 + 4.65\sqrt{C}, \tag{3.24}$$

where L_D increases with continuum counts C. Figure 3.20 depicts the concepts of L_C and L_D.

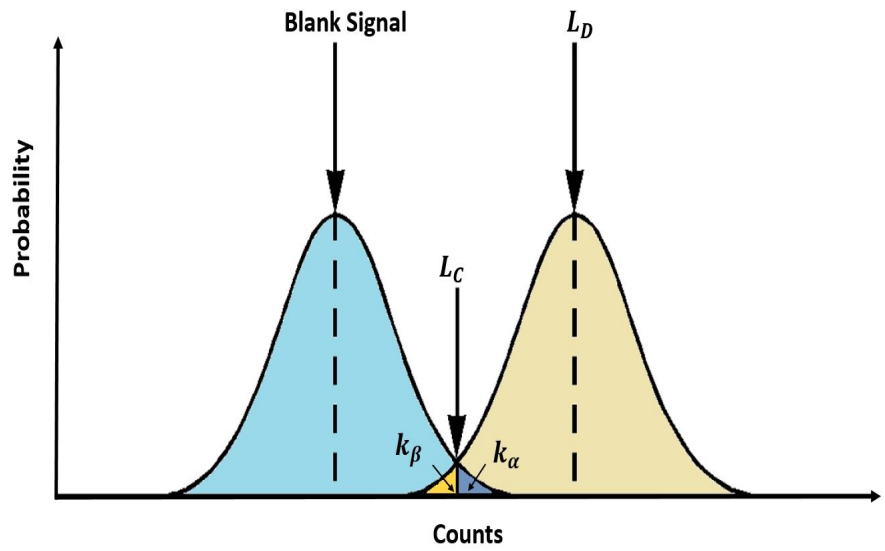

Figure 3.20: The representation of L_C and L_D showing the first (α) and second kind (β) errors. Adapted from [24]

In gamma spectrometry, to convert the L_D value to MDA, we need to take into account additional factors, such as the full energy peak efficiency ϵ_{peak}, live time of the acquisition T, yield of the emitted nuclide gamma ray y, mass of the sample m and decay correction factors K_w and K_c (see Equation 3.20).

Hence, the MDA value of the specific activity is defined in Equation 3.25 [24]

$$MDA = \frac{L_D}{\epsilon_{peak} \cdot T \cdot y \cdot m \cdot K_w \cdot K_c}. \tag{3.25}$$

The computed MDA values, for a blank sample with no activity, are an a priori estimate of the best sensitivity that can be expected from true sample measurements. For an actual sample, the computed MDA a posteriori (for continuum), will be higher than the a priori estimate due to interference and Compton scattering from other nuclides present in the actual sample [2].

3.3.3 Radiochemical analysis of the samples

This section gives a brief overview of the radiochemical analysis techniques, which we use to measure the specific activities of the DTM radionuclides in the waste samples (pure β-emitters, low-energy γ-rays and X-ray emitters), which can not be measured directly via NDA techniques. Using DA techniques allows the establishment of the experimental SFs (detailed description of SF method is in Section 3.4).
The radiochemical measurements are carried out on samples taken from a waste population, which is described in Section 2.4. Those sample measurements are performed by external laboratories [74]. We here describe the radiochemical measurement techniques, which are most frequently used in the laboratory of Jacobs[21] [33] for the radionuclides of interest, such as H-3, Fe-55 and Ni-63.

3.3.3.A Sample preparation

The sample preparation is essential for both accurate and reproducible analysis results [114]. The metallic samples are reduced in size if required. The process can involve digestion in mineral acids as a first step before being submitted for further analysis, such as gamma spectrometry, Fe-55 and Ni-63 [33].
The measurement of tritium is based on the pyrolysis method, in order to isolate H-3 from the matrix and also separate it from the potential interfering radionuclides such as C-14 or S-35 [44].

3.3.3.B Analytical methods

The radioactivity of the ETM radionuclides are estimated using the high energy resolution gamma spectrometry technique. The analyses are conducted using high-purity germanium detectors, coupled to MCA for gamma spectrum acquisition. The spectrum analysis steps include peak search and area calculations, background subtraction, efficiency calibration and activity calculations with a validated radionuclide library.
For the measurement of Fe-55 activities in iron or stainless steel samples, Fe-55 is separated from the prepared sample solution by solvent extraction using, e.g., di-isopropyl ether. The purified iron fraction follows a further decolorization step. This step is critical to match the calibration regime of the Liquid Scintillation Counter (LSC) instrument. Finally, the Fe-55 content is measured using the LSC analysis technique. The LSC is a common technique for the measurement of pure beta emitting radionuclides and includes the radionuclides that decay by electron capture. It has been applied in many aspects such as the characterization of radioactive waste [70].

[21] https://www.jacobs.com/, 16 March 2021

In order to measure the Ni-63 activities in the samples, Ni-63 is separated by anion-exchange, subsequently by the use of a nickel-specific resin. Finally, the prepared samples are measured using LSC.

The pyrolysis method is designed to evaluate the total radioactivity of H-3 which combines both of tritiated water (HTO) and organically-bound tritium (OBT). According to [33]:

"(...) The sample is burned in a two-staged catalytic pyrolyser, which consists of several independently controlled furnaces. Through those furnaces, a silica tube, is inserted. The heated catalyst that is carried by the latter half of the silica tube oxidises all forms of tritium to HTO with high efficiency. The subsequent outlet is passed into a system of water bubblers where the HTO vapour gets condensed and the tritium is exchanged with water in the bubblers. The aliquot of the distillate is then measured using LSC to determine the tritium concentration (...)".

3.4 Scaling factor (SF) formalism

The Scaling factor method is a technique for evaluating the radioactivity concentration of DTM and ITM radionuclides that exist in the radioactive waste. International Atomic Energy Agency (IAEA) and International Organization for Standardization (ISO) provide the theoretical justification of the SF method that can be found in [14],[18] and [73]. The SF method can be widely applied in nuclear power plants, nuclear facilities, and particle accelerators to radiologically characterize radioactive waste.

The applicability of the SF method relies on a correlation between radionuclide activity values. Often, it is convenient to correlate a given pair of DTM and KN radionuclide activities with similar production mechanisms and physiochemical characteristics. During the establishment of the scaling factors, one needs to apply statistical methods for checking the existence of such a correlation.

The correlation between DTM and KN in a waste package is established either via measurements or analytical calculations such as ActiWiz (see Section 3.2.2). The measurements can rely on DA (for H-3) or NDA techniques (for Co-60) with adequate detection limits. The establishment of the experimental scaling factor distributions, requires the collection of a representative sample set taken from the waste population. The sampling strategy for LL/IL waste produced at CERN is based on the knowledge gained from previous studies carried out for VLL waste [121]. The analytical calculations need to rely on appropriate physics models and sufficiently accurate knowledge of the chemical composition and activation scenarios. Finally, one needs to consider any physiochemical behaviour (such as diffusion) that could affect the migration of radionuclides within the waste.

The SF of the sample n_i collected in a waste is given by the ratio of the activities of the DTM and KN,

$$SF_i = \frac{a_{DTM_i}}{a_{KN_i}}. \tag{3.26}$$

The radionuclide activity concentrations are often distributed over a range spanning several orders of magnitudes. There are two main methods to calculate the mean values of the SF.

An arithmetic mean is calculated as shown in Equation 3.27. For a large variation of the individual values averaged, the arithmetic mean can propagate a weighted value towards the higher values and can be inappropriately skewed.

$$\overline{SF} = \frac{1}{n}\sum_{i=1}^{n}(SF_i). \tag{3.27}$$

Whereas, a geometric (or log) mean can be expressed as the exponential of the arithmetic mean of logarithms. This method reduces the effect of extreme or outliers values. The geometric

scaling factor is defined as follows in Equation 3.28

$$\overline{SF} = exp\left(\frac{1}{n}\sum_{i=1}^{n} ln(SF_i)\right). \tag{3.28}$$

The radioactivity of the DTM radionuclide is estimated by multiplying its corresponding SF by the activity concentration of the KN. The average SF is calculated as a geometric mean (or arithmetic mean) from the analyzed values assuming a linear relationship between the KN and DTM nuclides. The general formula of the linear model can be determined as follows [122].

$$\hat{a}_{DTM_i} = \hat{\beta}_0 + \hat{\beta}_1 \times a_{KN_i}, \tag{3.29}$$

where $\hat{\beta}_0$ and $\hat{\beta}_1$ are the model parameters estimated from the *n* samples collected from the waste population and a_{KN_i} is the measured radioactivity of the key nuclide in the *ith* waste package. In Equation 3.29, the intercept $\hat{\beta}_0$ is usually set to zero following the hypothesis[22] that either both KN and DTM have an activity different from zero or both have an activity equal to zero. The slope $\hat{\beta}_1$ represents the estimated scaling factor from the linear model built from the values of *n* samples collected. Information about the SF's applicability can be supported by involving common statistical tools, such as the coefficient of determination in multiple regression[23], R^2 [9] or Student's test and Fischer-Snedecor's test to validate the linear relationship for KN and DTM radionuclides.

More complex mathematical relationships between key nuclides and DTM nuclides can be modelled by methods such as linear regression of logarithms of the measurement data, which can be applied to non-linear relationship between pair of radionuclides KN and DTM [73]).

[22] this hypothesis may not be true especially when the radionuclides have a large difference in half-lives and one of them is completely decayed.

[23] or correlation coefficient (CC), typically values of the CC above 0.6 have been taken to indicate evidence of significant positive correlation.

3.5 Radiological characterization workflow

This section presents the general overview of the radiological characterization process developed at CERN for LL/IL, metallic waste that will be subjected to melting prior to final disposal. The process is depicted in Figure 3.21.

The initial step **Define the radioactive waste** relies on the definition of a waste population intended for elimination. Within the scope of this thesis, the waste population is composed of mostly legacy, solid metallic waste.

Next, we collect information about the waste population based on the key parameters listed by IAEA. That information is needed in the next steps of the radiological characterization.

The key parameters[24] for the the radiological characterization include:

- physical state;
- volume, mass and dimensions of waste items;
- origin of the activity (contamination or activation);
- radiological profile: e.g. irradiation t_i and cooling t_c times.

In order to predict the radionuclide inventory (step **Predict the radionuclide inventory**), we carry out analytical calculations using ActiWiz (see Section 3.2.2). In the case of legacy waste, we need to predict unknown parameters required for the analytical calculations. For instance, for undefined cooling time t_c, we consider a set of potential cooling times, which vary from 3 years up to 30 years. As a result of this step, we can establish a list of expected radionuclides, which can be classified as ETM (including KN), DTM or ITM. Additionally, we can establish CFs for the ITM radionuclides.

The following step **Pre-select** uses an experimental dose rate threshold for pre-sorting waste into either VLL, LL/IL "other" (not considered for the melting in the future) and LL/IL "MAST", where the latter is considered for further selection as LL/IL waste candidate for melting within the ongoing Melting of Activated STeel (MAST) project [48]. Subsequently, for every sampling campaign, a representative sample set is collected from the waste population (step **Collect samples**). The collected samples are subjected to radiochemical analysis techniques (see Section 3.3.3). The objective is to establish the SFs for the DTM radionuclides (see Section 3.4). The entire process to establish the SF for the DTM radionuclides might be long and challenging, in order to collect representative samples from the waste population. Within the present thesis, the estimation of DTM activity values is based on the SF established for VLL waste.

The **Select** step defines an operational method that can estimate the total beta-gamma specific activities of pre-selected waste items (see Section 4.1). This method is deployed in order to min-

[24] The key parameters for unconditioned waste are listed in Table 2.1

imize the number of gamma spectrometry measurements of the pre-selected items, by further reducing the probability of a mistake during selection.

When the waste package is formed based on the selection method (see Chapter 6), we analyze it in order to be eliminated (step **Analyze waste package for elimination**). This step corresponds to the NDA measurements (step **NDA measurements. Establish ETM specific activity**) carried out in the gamma spectroscopy facility at RWTCS.

As shown in Figure 3.21, the ETM(KN) specific activity is established via gamma spectrometry analysis (see Section 3.3.2). Hence, we can obtain the specific activities of DTM and ITM radionuclides by multiplying the specific activity of the KN with the established SFs and CFs corresponding to identified radionuclides DTM and ITM (step **Quantify DTM and ITM specific activity**).

The final step presents the possible applications that are based on the specific activities obtained previously. For instance, we can calculate the total beta-gamma specific activity with the associated uncertainty. The total beta-gamma specific activity needs to satisfy the acceptance criteria of the melting facility.

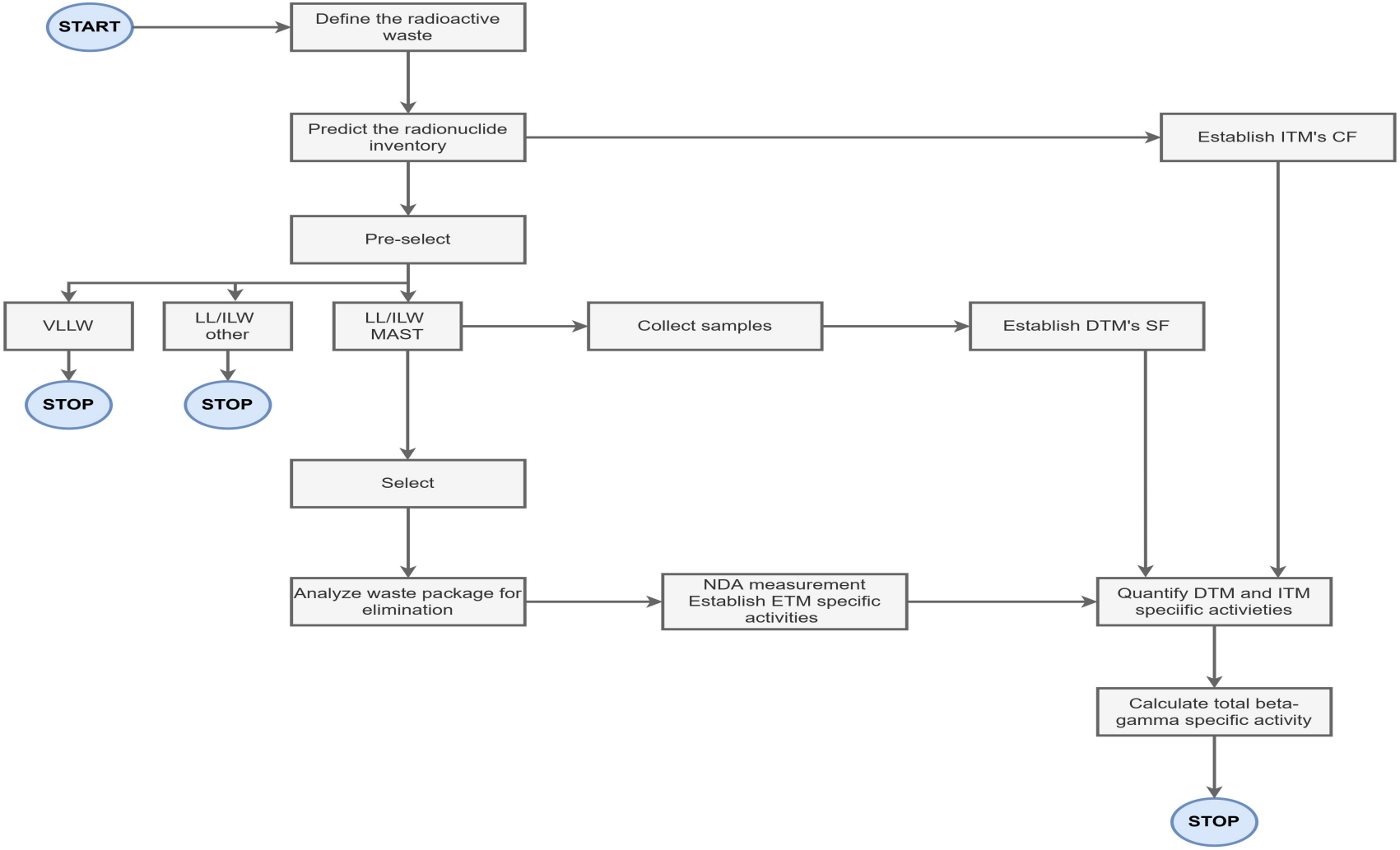

Figure 3.21: The radiological characterization process developed for LL/IL waste at CERN that will be subjected to melting in the future.

Chapter 4

A novel Non-destructive Assay technique

The process of the radiological characterization of radioactive waste consists of a series of radiation measurements, complemented by analytical studies. The objective of performing such analyses is to quantify the activity of radionuclides inside the waste item.

First, we introduce a methodology that allows the quantification of the specific activities of Co-60 and other beta-gamma emitters within a waste package using the SF approach (see Section 5.3.4). This is based on the measured average dose rate mapping at 40 cm from the individual waste items that will be packaged inside the waste container. We provide an experimental correlation between the ratio of the specific activity of Co-60 and the average dose rate as a function of apparent density of the waste item. This methodology is valid under the assumption that Co-60 is the dominant gamma emitter (referred to as KN) in the waste item, where the decay time is more than 3 years. The objective is to evaluate whether the individual waste item processed in the selection phase has a total specific beta gamma activity lower than a certain threshold, e.g. 20 kBq/g for the melting. The methodology is validated using gamma spectroscopy techniques with a geometry model optimization formalism for waste packages (see Section 5.5).

The quantification of the gamma emitters (ETM) is typically performed by gamma spectrometry, under the assumption of homogeneous activity distribution within an item. However, due to the activation mechanisms, some waste can have heterogeneous activation patterns. In this chapter, we describe the qualification of gamma spectrometry measurements of LL/IL waste in order to quantify the impact of assuming homogenous distribution of activity. The qualification is a process used to assess the capacity of a model to predict physical quantities within a set of assumptions. Qualification studies [64] [55] have shown the effect of varying geometry model parameters on the efficiency calibration curves and the activity results.

Section 4.2 briefly describes the measurement conditions that relate to both the acquisition and analysis parts of the *In-Toto* gamma spectrometry of LL/IL waste. Second, we present the geometry optimization technique in order to improve the accuracy of the activity values (see Section 4.3).

Finally, Section 4.4 focuses on the qualification of gamma spectrometry, including the characteristics of the assayed LL/IL waste, the impact of the various geometries on the efficiency calibrations, and geometry optimization activity results. Additionally, the activity qualification approach is presented in Section 4.4.3, in order to identify the "best model" that describes the activity values of the measured item.

4.1 Selection phase criteria of the MAST waste items

In the selection phase, the process includes a step to fill a MAST container (either 2.7 m^3 or 4 m^3) preparing it for further analysis in view of its transport to the melting facility. Hence, we propose an intermediate step between pre-selection and the gamma spectrometry analysis of the MAST waste package. We introduce an operational method that can estimate the total beta-gamma activity of pre-selected waste items based on the measured Average Dose Rate (AVG-DR) and apparent densities. We establish a correlation between the ratio of the Co-60 specific activity and the AVG-DR as a function of the apparent density. The Co-60 specific activity is estimated using gamma spectrometry, the AVG-DR is measured using both scanning and multiple points around the waste item (at contact, 10 cm, and 40 cm) while the apparent density is estimated by taking the ratio between the item's mass and the apparent volume envelope.
For 35 individual waste items, we performed gamma spectrometry analyses and the corresponding AVG-DR measurements. The gamma spectrometry acquisition and analyses are carried out using a High Purity Germanium detector (Falcon 5000 HPGe) in a dedicated area of the RWTCS as shown in Figure 4.1.

Figure 4.1: Gamma spectrometry setup for *In-Toto* measurement of the bulky pipe CR-015901.

The item-to-detector distance is selected in order to have a maximum allowed dead time of less than 15 % for all measured waste items. The acquisition live time varies from 10'000 to 72'000 seconds for bulky items. For hollow items, the acquisition live time is set to 10'800 seconds. Dose rate measurements are carried out using the Dose Rate Meter 6150AD 6/H[25] with the measuring range from 0.1 μSv/h to 10 mSv/h and the energy range from 60 keV to 1.3 MeV. We perform two types of AVG-DR estimations. The first approach is based on the

[25] https://www.automess.de/assets/documents/en/Prospekt_6150AD_E.pdf, 1 May 2021

collection of several measurement points depending on the waste size and shape. In general, dose rate mapping is done for three distances; at contact, at 10 cm and at 40 cm from the outer surface of the waste item. Additionally, we complete these measurements by scanning the entire object at contact and at 40 cm distance. We use the option of the device that we collect the average value of the dose rate, which allows us to record the dose rate more accurately. This is a complementary measurement for long pieces with the highest dose rate differences across the waste item. For the ion pumps that produce magnetic field, we used the RadEye[26] device from ThermoFisher Scientific, which was tested in the presence of magnetic field strengths up to 300 mT [42]. The background dose rate at the measurement area varies between 0.07 and 0.1 μSv/h. We show the formulas that enable us to estimate the specific activity of Co-60 with dose rate measurement at contact, at 10 cm and at 40 cm from the outer surface of the waste item. This estimation of the KN allows calculations of the total beta-gamma activity of individual waste item using the SFs listed in Table 5.3. For each AVG-DR measurement distance, we produce a curve of the ratio between the Co-60 Specific activity and the AVG-DR as a function of the apparent density as shown in Figure 4.2. A fit is performed for each data set to produce a penalizing fit function at the 50% confidence level.

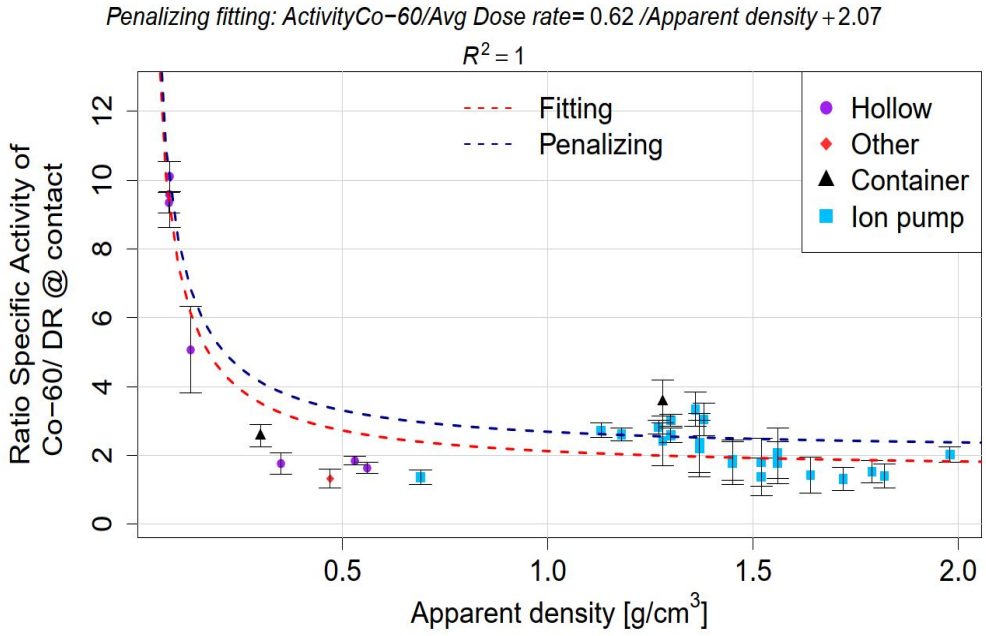

(a) Specific activity of Co-60/Average dose rate at contact as a function of apparent density. The fit (red line) is ActivityCo-60/Avg Dose rate= 0.59/Apparent density+1.52, R^2=0.93

[26] https://www.thermofisher.com/order/catalog/product/4250671#/4250671, 1 May 2021

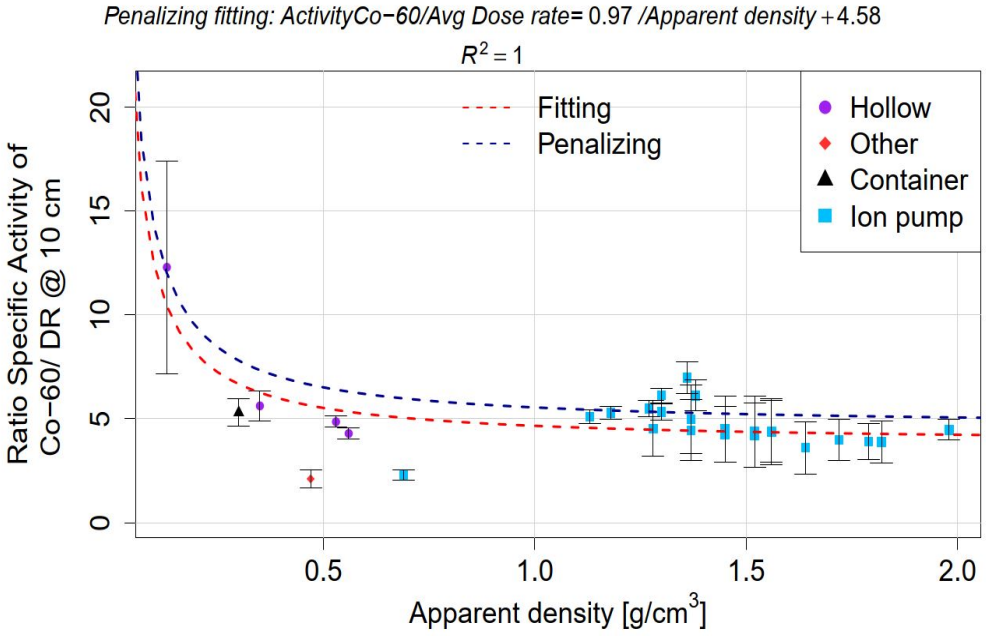

(b) Specific activity of Co-60/Average dose rate at 10 cm as a function of apparent density. The fit (red line) is ActivityCo-60/Avg Dose rate= 0.86/Apparent density+3.80, R^2=0.70

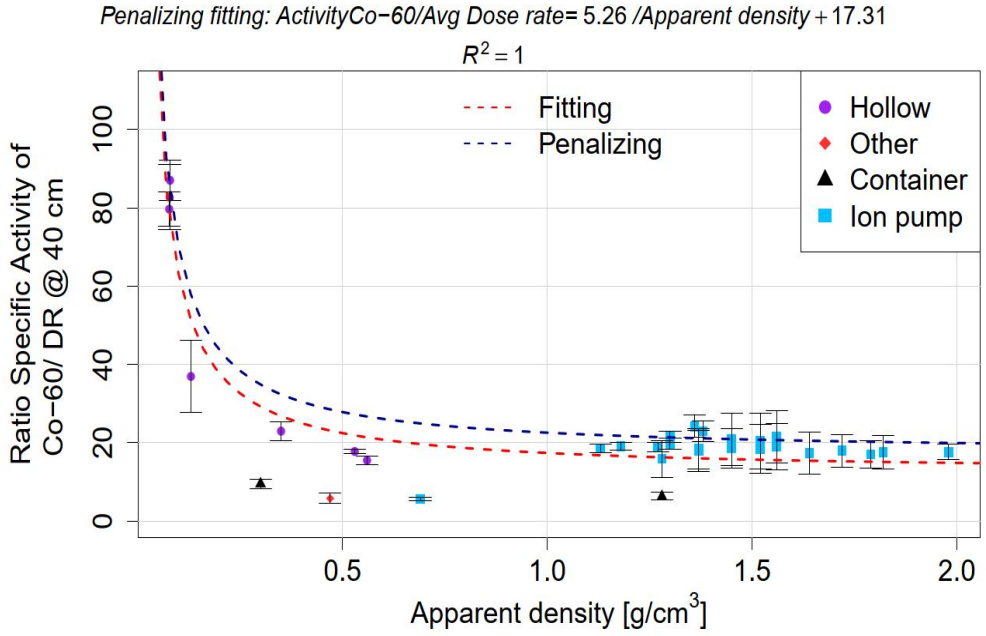

(c) Specific activity of Co-60/Average dose rate at 40 cm as a function of apparent density. The fit (red line) is ActivityCo-60/Avg Dose rate= 5.07/Apparent density+12.31, R^2=0.92

Figure 4.2: The ratios of the specific activity of Co-60 and AVG-DR at three distances: at contact, at 10 cm and 40 cm as a function of the apparent density. The data points represent the measurements (gamma spectrometry and dose rate mapping) for hollow (e.g. pipes), ion pumps, container and other waste item considered as MAST LL/IL waste candidates.

Equations 4.1a-4.1c present the penalizing functions to estimate the specific activity of Co-60.

$$\textit{Activity Co-60 (Bq/g)} = \left[\frac{0.62}{\textit{Apparent density}(\frac{g}{cm^3})} + 2.07\right] \cdot AVG - DR@contact, \quad (4.1a)$$

$$\textit{Activity Co-60 (Bq/g)} = \left[\frac{0.97}{\textit{Apparent density}(\frac{g}{cm^3})} + 4.58\right] \cdot AVG - DR@10cm, \quad (4.1b)$$

$$\textit{Activity Co-60 (Bq/g)} = \left[\frac{5.26}{\textit{Apparent density}(\frac{g}{cm^3})} + 17.31\right] \cdot AVG - DR@40cm. \quad (4.1c)$$

Instead of performing gamma spectrometry measurements of each item, we deploy a computation, where a function consists of two input values: the average dose rate AVG-DR and the apparent density. Taking into account radiation protection dose optimization objectives and the inherent averaging properties of far dose rate measurements, we recommend implementing the selection criterion methodology that is based on the 40 cm distance.

4.2 Gamma spectrometry assay setup of LL/IL waste

Gamma spectrometry is a commonly deployed technique at CERN to quantify the residual activity of gamma emitters in various items, ranging from small volume samples in a laboratory to large items such as unitary blocks or waste containers. Gamma spectrometry occupies an important role in the radiological characterization process of LL/IL waste at CERN. Gamma spectrometry measurements on LL/IL items present a number of challenges during both the acquisition and the analysis steps. The former challenges relate to the high counting rate effects, long counting time required to meet the MDA requirements, available physical space, and the necessity to count from multiple faces. The latter challenges are due to the difficulty to model the geometry and combine the multiple counts results.

The available space at the gamma spectrometry laboratory at CERN and also the waste package dimensions limit the waste-to-detector distance. This leads to performing the acquisitions at higher counting rate and dead times. An example of the counting setup is illustrated in Figure 4.3.

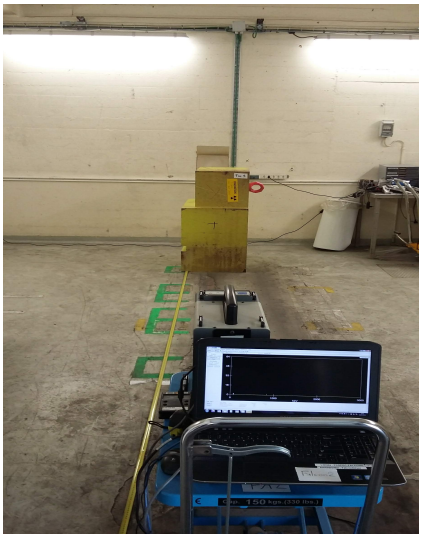

(a) Gamma spectrometry setup for measurement of waste. The maximum contact dose rate of the presented waste is 400 μSv/h. In order to obtain a dead time below 10%, the distance detector-waste is set at 3 meters.

(b) Gamma spectrometry setup for measurement of container filled with ion pumps. The maximum contact dose rate of the container is above 250 μSv/h. Due to space limitation, the maximum distance detector-waste is about 1.5 meters resulting in dead time of 24 %.

Figure 4.3: Gamma spectrometry setup at RWTCS laboratory for measurement of radioactive waste.

A significant parameter of the acquisition step is the system dead time (detailed description can be found in Section 3.3.2.D). In order to avoid gamma spectrum distortions, we seek to limit the dead time value up to $\sim$ 15% nominally. However, the dead time could be higher, as indicated in Figure 4.3b where the dead time reached 24% due to insufficient space around the waste item.

We also need to set the acquisition time and the geometry in such a way as to ensure that the MDA values are below the LL/IL waste declaration thresholds for the expected ETM radionuclides. Table 4.1 presents an example calculation of the MDA values for Co-60 radionuclide during the acquisition of typical waste: a pipe (Figure 2.4b), an ion pump (Figure 2.4c), and a container 2.7 m^3 (Figure 4.3b).

Table 4.1: Calculated MDA values for the acquisition live time of 10 000 seconds for different types of waste.

Waste code	**Description**	**Radionuclide**	**MDA [Bq/g]**	**LL/IL Declaration Threshold [Bq/g]**
CR-018150	Pipe	Co-60	0.38	10
CR-120640	Container 2.7 m^3	Co-60	0.09	10
CR-006532	Ion pump	Co-60	0.13	10

When selecting the LL/IL to be measured by gamma spectrometry, one needs to take into account the As Low As Reasonably Achievable (ALARA) [56] principle. Occupationally exposed personnel at CERN are classified into two categories in terms of the dose limits (details can be found in [60]). It is a priority at CERN to apply the ALARA principle: this covers the justification of exposure, the optimization of collective and personal doses as well as the limitation of received doses. At CERN more than 99% of users equipped with a personal dosimeter receive less than 1 mSv effective dose/year. To achieve this goal, the maximum dose rate at contact of the LL/IL items in the elimination campaigns is limited to 1mSv/h.

Another challenge when performing the gamma spectrometry measurements and analyses is the case of highly attenuating waste. Such a waste is more prone to higher geometry modelling uncertainties, due to its geometry parameters that might not be well known, such as material composition, density, and dimensions.

In addition, in the case of a large activity heterogeneity within the waste, some radionuclides might not be identified on one face, despite their presence and identification on another face. Hence, in order to improve the accuracy of the activity estimation, we propose performing gamma spectrometry measurement of multiple faces. The number of measurements will depend on the dimensions and activity distribution of the waste. Multi-faces measurements are shown in Figure 4.8.

A significant step in the gamma spectrometry analysis involves using the software package ISOCS in order to model the geometry of waste. However, for waste with heterogeneous activity distribution and various shapes, ISOCS offers limited functionalities. This limitation leads to larger uncertainties in the activity estimation results. To overcome this limitation, we developed a new methodology described in Section 4.3

4.3 Geometry optimization technique for improved efficiency calibrations

Activated components can be removed from the accelerator complex at CERN for maintenance, or dismantling. Such operations require characterization in view of the further disposal as radioactive waste. The characterization process consist of radiation measurements, complemented by analytical studies, which quantify the activity of radionuclides inside a given activated item. Within the present thesis, we consider a fraction of metallic radioactive waste without contamination with a dose rate higher than 100 μSv/h that can be classified as a LL/IL waste (see Chapter 2). Due to the activation mechanisms, the waste can have significant variations in activity distributions or heterogeneities.

When gamma spectrometry measurements are performed on waste, knowledge of the geometry model parameters, including dimensions, position with respect to the detector, material composition, and activity distribution (hotspots) is often limited, especially for the two last parameters. The uncertainties related to activity distribution are described in [80]. Additionally, [46] focuses on the uncertainties that correspond to dimensions, material composition etc.. The ISOCS tool (see Section 3.3.2.F) allows the computation of the full energy peak efficiencies for each waste item (or sample) in order to estimate the activity values of the waste without using radioactive sources standards at the laboratory. The associated uncertainties of the ISOCS efficiency values take into account only the uncertainties due to the numerical approximations, peak area statistics and emission intensity values. However, performing the gamma spectrometry analysis, the gamma emitters (ETM) are quantified under the assumption of homogeneous distributions of activity within a measured waste. This assumption might lead to underestimating the activity values of the identified ETM radionuclides. In order to determine the uncertainties of the measured activities, due to waste geometry parameters, such as dimensions and heterogeneous source distribution, a tool called Geometry Uncertainty Reduction Utility (GURU) has been developed [63]. This tool consists of two modules. One quantifies the geometry model uncertainties and the other reduces them by combining the gamma spectrometry results in order to identify the best estimate model that best describes the "actual" geometry of the waste.

In the case of a heterogeneous distribution of the activities within the waste, various hotspots can be positioned inside the geometry model. However, modelling the hot spots in ISOCS using the Complex Box template is limited to a single hotspot in the model. Conversely, IUE (see Section 3.3.2.G) enables modelling multiple hotspots. Nevertheless, those hotspots within the model are limited to a single relative activity concentration value for all hotspots. To overcome those limitations when performing a quantification and reduction of the uncertainties for multiple hot spots with a different relative activity concentrations that can be present in the model, we use the GURU DataAnalyzer/SpectroMatcher framework [63].

4.3.1 Estimation of efficiency calibration uncertainties

The geometry parameters are often not well known. In order to quantify the most influencing parameters of the model, we perform a sensitivity analysis. Based on this, we can focus on the parameters whose impact on the efficiencies and associated activities are negligible. In addition, we can identify trends of efficiency variation trends.

The DataAnalyzer is a module in GURU that relies on multiple analysis results extracted from ISOCS and IUE. Within this module, one can deduce the most sensitive parameter(s) by varying One-factor-At-a-Time (OAT) or allowing them to change simultaneously for performing uncertainty analysis.

Considering the sensitivity analysis by perturbing One-factor-At-a-Time (OAT), one can assume an initial model as the reference model (also called "ref model"), which is based on the ensemble of geometry parameters and the corresponding uncertainties. The variation intervals of the efficiencies are established using a specific distribution of the waste geometry parameters. During the perturbation process, the geometry parameters are sampled within the interval limits using a sampling distribution such as uniform or normal.

The variation of the efficiencies for a variety of the geometry model parameter is calculated using Equation 4.2a

$$\epsilon_{\text{model i}}(\overrightarrow{X}, E) - \epsilon_{\text{ref model}}(\overrightarrow{X}, E) = \partial\epsilon, \tag{4.2a}$$

where $\epsilon_{\text{model i}}$ represents the efficiency of model i at energy E and $\epsilon_{\text{ref model}}$ is the efficiency of the reference model at energy E. $\overrightarrow{X}$ is a vector of variable model parameters $(X_0, ...X_i, ...X_n)$. $\partial\epsilon$ is an absolute efficiency variation. Equation 4.2b represents a relative efficiency variations $\partial\epsilon_{\%}$.

$$\frac{\epsilon_{\text{model i}}(\overrightarrow{X}, E)}{\epsilon_{\text{ref model}}(\overrightarrow{X}, E)} - 1 = \partial\epsilon_{\%} \tag{4.2b}$$

Based on Equations 4.2a, one can determine the relative sensitivity S^{ϵ}_{Xi} of the efficiency ϵ to a model parameter Xi given in Equation 4.3 .

$$S^{\epsilon}_{Xi} = \frac{\partial\epsilon}{\partial Xi}. \tag{4.3}$$

The sensitivity indicates whether parameter Xi significantly impacts the efficiency value. However, one has to bear in mind that the uncertainties can be high for parameters with low impact. Therefore, Equation 4.4 describes the relative change of the efficiency as a result of the uncertainty propagation.

$$\sigma^2(\epsilon) = \sum_i \sum_j \frac{\partial\epsilon}{\partial Xi}\frac{\partial\epsilon}{\partial Xj}\sigma(Xi)\sigma(Xj)r_{i,j} = S^{\epsilon}_{X}\mathbf{M}S^{\epsilon^T}_{X}. \tag{4.4}$$

Where $\frac{\partial\epsilon}{\partial Xi}$ is the sensitivity of the efficiency to the parameter Xi (or Xj), σ(Xi), σ(Xj) represent

respectively the uncertainty of the parameters Xi and Xj and $r_{i,j}$ is the Pearson correlation between Xi and Xj. M is the variance-covariance matrix.

4.3.2 Reduction of efficiency uncertainties

By varying the geometry parameters, a set of perturbed efficiency calibration curves is produced. These curves are used to evaluate activity results as a function of the geometry parameters. In order to perform an optimization (i.e. determine the best geometry models), the following constraints should be fulfilled [45].

Multi-count consistency is the requirement that multiple gamma spectrometry measurements carried out at different locations should give the same value of the measured activity of the item. Additionally, the calculated activity values for each emission line of a radionuclide should be consistent.

Those constrains are exploited by the SpectroMatcher module in GURU. This module enables correlating the efficiencies of all faces. We can correct the known activity values of reference model by the efficiency ratio, as presented in Equation 4.5, where $A_i^k(j)$ is the calculated activity for the radiocuclide with emission j using model i for the face k. $A_{ref}^k(j)$ represents the calculated activity with the reference model. The efficiencies $\epsilon_{ref}^k(E)$ and $\epsilon_i^k(E)$ correspond to the reference model and model i at energy E of emission j from the face (detector) k.

$$\forall i, j, k, A_i^k(j) = \frac{\epsilon_{ref}^k(E)}{\epsilon_i^k(E)} A_{ref}^k(j) \tag{4.5}$$

Based on Equation 4.5, we can calculate the activity values for each radionuclide with emission j, model and face.

Hence, we can match the activities between different faces and identify the best models that better describe the "actual" geometry, based on combining the different gamma spectrometry results. This method uses the Figure of Merit (FOM)s that quantifies the consistency between activity values obtained from multiple countings, or obtained from multiple gamma-lines emitted by the same radionuclide. The FOM is determined in Equation 4.6 for each gamma emission j and model i.

$$FOM_i(j) = \sum_{k=1}^{K} (A_i^k(j) - < A_i(j) >)^2. \tag{4.6}$$

Where, $< A_i^k(j)$ is the activity of the radionuclide with associated gamma emission j using model i for face k.

$< A_i(j) >$ is the average over K faces for emission j using model i, which is defined as $< A_i(j) >= \sum_{k=1}^{K} \frac{A_i^k(j)}{K}$.

The user needs to select the gamma lines of interest, among the ones identified in all faces of the gamma spectroscopy measurement results. Then, one can calculate a Rank (as given in Equation

4.7) for each gamma emission line and model by summing the sub-ranks ($subRank_i^j$) according to the FOM value. Namely, the sub-rank $subRank_i^j$ is obtained by ranking the $FOM_i(j)$. Hence for all models n, the best model for each gamma emission line is assigned to a sub-rank # 1, the second best to # 2, etc..

$$Rank_i = \sum_{j=0}^{J} subRank_i^j. \tag{4.7}$$

Where J is the number of common gamma emission lines formed for each face. The model with the minimum $Rank_i$ is considered as the best model.

4.3.3 The hotspots formalism

In this section, we introduce the hotspot formalism. In the case of a significant heterogeneous activity distribution within the item, one can expect various hotspots with different relative activity concentration. With the ISOCS limitations where only a single hot spot can be modeled in the geometry and IUE that allows multiple hot spots but they are limited to a single relative concentration, we use the GURU Data Analyzer framework [63] to overcome these limitations. In order to simplify the formalism of N hotspots, we here consider a model with two hotspots. The set of efficiency computations given by IUE corresponds to hotspots h1 and h2 as presented in Figure 4.4. In the case presented in Figure 4.4, the total model is a combination of h1, h2 and the # geometry model. The hotspots relative activity concentrations of the latter one are set to 0.

Referring to Equation 3.16, the efficiency $\epsilon(E)$ is defined as a ratio of the number of counts *N* recorded in the peak at energy E to number of photons *C* emitted by the source.

Hence, the total efficiency ϵ of the presented case is given by Equation 4.8.

$$\epsilon_{total} = \frac{N_{total}}{C_{total}} = \frac{N_{\#} + N_{h1} + N_{h2}}{C_{\#} + C_{h1} + C_{h2}} = \frac{1}{C_{\#} + C_{h1} + C_{h2}} \Big(\frac{N_{\#} C_{\#}}{C_{\#}} + \frac{N_{h1} C_{h1}}{C_{h1}} + \frac{N_{h2} C_{h2}}{C_{h2}} \Big) \tag{4.8}$$

From Equation 4.8, we derive Equation 4.9 that presents the efficiency of the total model consisting of two hotspots.

$$\epsilon_{total} = \frac{\epsilon_{\#} C_{\#} + \epsilon_{h1} C_{h1} + \epsilon_{h2} C_{h2}}{C_{\#} + C_{h1} + C_{h2}} \tag{4.9}$$

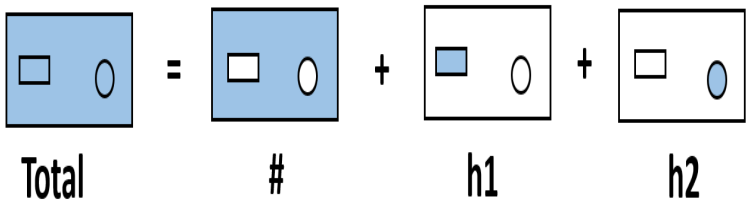

Figure 4.4: Combination of hotspots geometry models in the "Complex Box" marked as a black frame. Blue colour represents a volume inside the sample with a relative activity concentration different from 0. White colour represents a volume inside sample with 0 relative activity concentration. Also, two shapes (circle and rectangular) represent distinct hotspots.

It needs to be noted that the efficiency of model # cannot be directly calculated using IUE. Therefore, IUE creates four (or 2N calculations if we consider N hotspots) calculations corresponding to various representations of the model, denoted as h1, h2, t1 and t2, as depicted in Figure 4.5. The purpose of the GURU software is to combine those calculations and construct the efficiency of the model that consist of N hotspots.

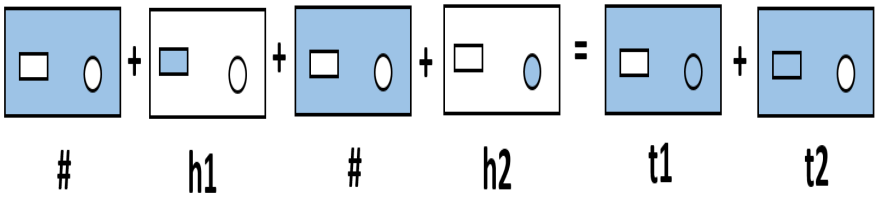

Figure 4.5: Combination of hot spots models #, h1 and h2 in order to obtain t1 and t2.

The efficiency of models t1 or t2 is given by Equation 4.10

$$\epsilon_{t1} = \frac{N_{t1}}{C_{t1}} = \frac{N_{\#} + N_{h1}}{C_{\#} + C_{h1}} = \frac{1}{C_{\#} + C_{h1}} \left(\frac{N_{\#} C_{\#}}{C_{\#}} + \frac{N_{h1} C_{h1}}{C_{h1}} \right) \tag{4.10a}$$

Hence,

$$\epsilon_{t1} = \frac{\epsilon_{\#} C_{\#}}{C_{\#} + C_{h1}} + \frac{\epsilon_{h1} C_{h1}}{C_{\#} + C_{h1}} \tag{4.10b}$$

Therefore, the efficiencies of models t1 and t2 are combined in Equation 4.11

$$\epsilon_{t1} + \epsilon_{t2} = \frac{\epsilon_{\#} C_{\#} + \epsilon_{h1} C_{h1}}{C_{\#} + C_{h1}} + \frac{\epsilon_{\#} C_{\#} + \epsilon_{h2} C_{h2}}{C_{\#} + C_{h2}} \tag{4.11}$$

In the specific case of $C_i = R_i m_i$, where the relative activity concentration is not taken into account R_i=1, the efficiency of # model can be reconstructed by extracting $\epsilon_{\#}$ and noting that $C_{\#} + C_{h2} = m_{\#} + m_{h2} = m_{t1}$ as shown in Equation 4.12.

$$\epsilon_{\#} = \frac{1}{2m_{\#}} [\epsilon_{t1} m_{t1} - \epsilon_{h2} m_{h2} + \epsilon_{t2} m_{t2} - \epsilon_{h1} m_{h1}], \tag{4.12}$$

Afterwards, taking into account Equations 4.11 and 4.12, Equation 4.13 leads to the efficiency of the total model with two hotspots.

$$\epsilon_{total} = \frac{\frac{R_\#}{2}[\epsilon_{t1}m_{t1} - \epsilon_{h2}m_{h2} + \epsilon_{t2}m_{t2} - \epsilon_{h1}m_{h1}] + \epsilon_{h1}C_{h1} + \epsilon_{h2}C_{h2}}{C_\# + C_{h1} + C_{h2}} \tag{4.13}$$

Bearing in mind the general case of N hotspots within the activated object, the general theory can be demonstrated in three steps.

Firstly, from Equation 4.9, we derive a formula that depends on # and N hotspots given in Equation 4.14.

$$\epsilon_{total} = \frac{\epsilon_\# R_\# m_\# + \sum_{i=1}^{N} \epsilon_{hi} R_{hi} m_{hi}}{R_\# m_\# + \sum_{i=1}^{N} R_{hi} m_{hi}} \tag{4.14}$$

Then, by reconstructing Equation 4.12, the efficiency of model # on N hotspots and t_i models, we obtain Equation 4.15

$$\epsilon_{total} = \frac{1}{N m_\# \Big[\sum_{i=1}^{N} (\epsilon_{ti} m_{ti} - \sum_{j=1, j\neq i}^{N} \epsilon_{tj} m_{tj}) \Big]} \tag{4.15}$$

Finally, the efficiency of the total model, that contains N hotspots, is given in Equation 4.16

$$\epsilon_{total} = \frac{\frac{R_\#}{N} \sum_{i=1}^{N} \Big[\epsilon_{ti} m_{ti} - \sum_{j=1, j\neq i}^{N} \epsilon_{tj} m_{tj} \Big] + \sum_{i=1}^{N} \epsilon_{hi} R_{hi} m_{hi}}{R_\# m_\# + \sum_{i=1}^{N} R_{hi} m_{hi}} \tag{4.16}$$

Where, each ϵ_{ti},i=1...N and ϵ_{tj},j=1...N correspond to the number of IUE computations that requires 2N hotspots.

Additionally, the validation of the hot spots combination that follows the new formalism presented above is detailed in [63].

4.4 Qualification of gamma spectrometry assay results

We perform a gamma spectrometry qualification in order to evaluate the underestimation of the real activity values of the radionuclides of interest, due to the assumption of a uniform activity distribution within the waste. These uncertainties can be quantified by comparing a reference model with an optimized experimental model considered as the "best model", which represents the best knowledge we can have regarding a system. The qualification process is applied to selected LL/IL waste, as described in the following sections.

4.4.1 Characteristics of the assayed LL/IL waste

The gamma spectrometry measurements are carried out in a dedicated area in RWTCS at CERN equipped with a HPGe detector, Falcon 5000. The measurements of two bulky items ($<$ 2 tons) are performed on the four faces of each unitary piece, as indicated in Figures 4.6 and 4.7.

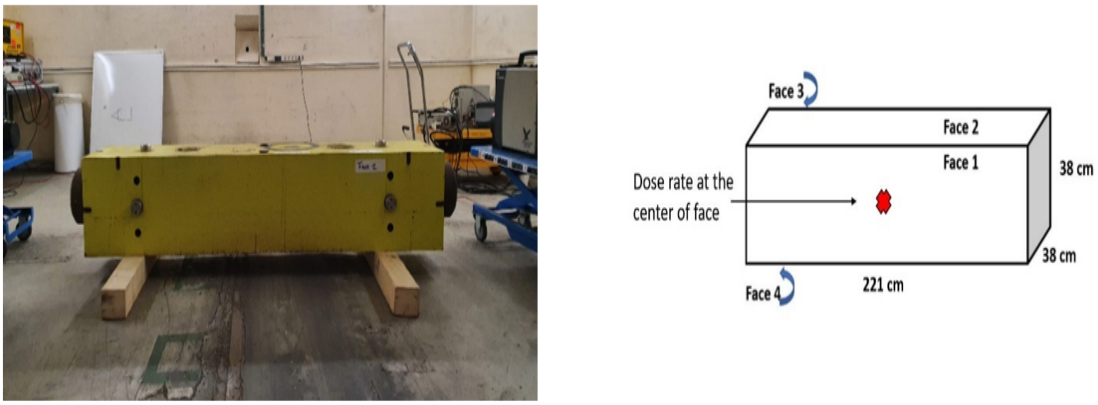

Figure 4.6: Gamma spectrometry setup for the measurement of waste items; the long iron block. Faces are identified on the right schematic view.

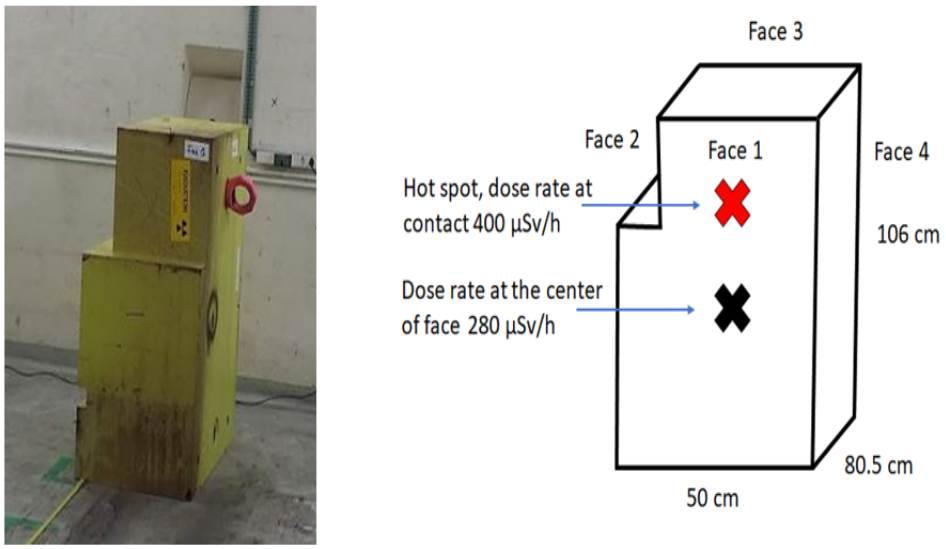

Figure 4.7: Gamma spectrometry setup for the measurement of waste items; the short iron block. Faces are identified on the right schematic view.

The geometry description can be visualized and edited in the ISOCS Geometry Composer. A three dimensional rendering of a representative geometry is shown in Figure 4.8

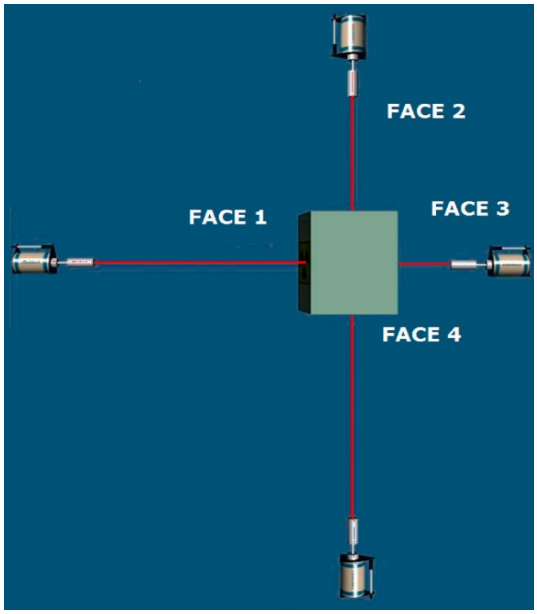

Figure 4.8: ISOCS geometry of the small iron block. The figure shows a combination of the geometry models for four faces of the waste item.

The main acquisition parameters for the iron blocks can be found in Table 4.2
For each each gamma spectrometry acquisition of each face (or count), we produce a set of efficiency calibration curves, applying the "Complex Box" ISOCS geometry template. Additionally, for each face we consider a uniform source distribution in the material matrix and an envelope geometry. The impact of an envelope geometry is presented in detail in Section 4.4.2.

Table 4.2: Main acquisition setup parameters of the gamma spectrometry measurements as well as maximum and minimum dose rate values measured at contact for unitary waste items.

	Long iron block	**Short iron block**
Maximum dose rate at contact (μSv/h)	289	400
Minimum dose rate at contact (μSv/h)	33	9
Distance detector-item (m)	from 2.4 to 2.7	from 0.5 to 3.2
Dead time (%)	from 8 to 9.3	from 4.1 to 9.8
Acquisition live time (s)	50 000	from 10 000 to 72 000

Then, for each face, activity values are determined using the Genie 2000 Nuclide Identification with the Interference Correction calculation engine. The multi-count activity ratios of the reference geometry models are presented in Tables 4.3-4.4 for both iron blocks.

Table 4.3: List of identified radionuclides with their activities (relative uncertainties) for the four faces of the unitary piece. The uncertainties are quoted at 1σ. The geometry model uncertainties are not included. The mass of the item is 2200 kg.

FACE	**Co-60 [Bq/g]**	**Na-22 [Bq/g]**	**K-42<Ar-42 [Bq/g]**	**Sc-44<Ti-44 [Bq/g]**
1	2.03E+02 (5 %)	9.14E-02 (16 %)	1.72E-01 (11 %)	1.22E+00 (6 %)
2	1.84E+02 (5 %)	4.74E-02 (26 %)	5.97E-02 (18 %)	3.91E-01 (8 %)
3	2.72E+02 (5 %)	2.40E-01 (10 %)	3.73E-01 (10 %)	3.16E+00 (6 %)
4	2.88E+02 (5 %)	4.27E-01 (7 %)	8.94E-01 (7 %)	6.71E+00 (6 %)
Activity ratio between faces 1 and 3	1.3	2.6	2.2	2.6
Activity ratio between faces 2 and 4	1.6	9.0	15.0	17.0

Table 4.4: List of identified radionuclides with their activities (relative uncertainties) for the four faces of the unitary piece. Blank cells represent activity values found below the MDA and which are neglected in this study. The uncertainties are quoted at 1σ. The geometry model uncertainties are not included. The mass of the item is 2650 kg.

FACE	**Co-60 [Bq/g]**	**Na-22 [Bq/g]**	**K-42<Ar-42 [Bq/g]**	**Sc-44<Ti-44 [Bq/g]**
1	2.48E+02 (5 %)	4.83E-01 (10 %)	1.22E+00 (9.5 %)	8.49E+00 (6.2 %)
2	1.09E+02 (5 %)		8.08E-02 (29 %)	5.89E-01 (11 %)
3	1.62E+01 (5 %)	3.96E-03 (21 %)		2.86E-02 (8.5 %)
4	1.41E+02 (5 %)	1.15E-01 (7.5 %)	2.29E-01 (9 %)	1.60E+00 (6 %)
Activity ratio between faces 1 and 3	16	122	Not Applicable	297
Activity ratio between faces 2 and 4	1.3	Not Applicable	3	3

The obtained activity values using the reference models - for both the long and short iron blocks

- show high activity ratios between the counts (between faces 1 and 3 or 2 and 4). The high ratio values (reaching a factor of 300 for the short item) can be explained by the large activity heterogeneities in the waste items. This effect can be also observed by measuring the contact dose rate on each face, as shown in Table 4.2. Hence, we can deduce that measuring one face with the assumption of a uniform source distribution might be insufficient to properly model the waste geometry and compute the ISOCS efficiency calibration values.

4.4.2 Impact of the envelope geometry

The physical shape of the waste item might be irregular, as in the case of the two iron blocks. Thus, we perform calculations to investigate the influence of different geometry configurations on the activity results. Two geometry models are considered. The first model assumes the maximum dimensions (maximum envelope) of the iron block. In the second approach, we assume a smaller (or minimum) envelope volume. In addition, both geometry models have homogeneous source activity distributions.

In Table 4.5, we summarize the dimensions of the envelope geometry models for both iron blocks.

Table 4.5: Maximum and minimum geometry models of the analyzed waste

Object	**Volume cm^3**	
	Maximum envelope	**Minimum envelope**
short iron block	50x80.5x106	45x75.5x106
long iron block	38x38x221	38x38x200

The ratios of the efficiency calibration values of the two considered models (maximum envelope/minimum envelope) vary between 0.98 and 0.99 for gamma ray energies ranging from 45 keV to 3 MeV. Since, the activity is inversely proportional to the efficiency calibration value (see Equation 3.20), we conclude that the maximum envelope model for long iron block overestimates the activities by about 2 %.

Respectively, for the short iron block, the ratios of the activity results of the two considered models vary between 0.93 and 0.94 for the same energy range as for long iron block. The maximum envelope model overestimates the activities by about 6 %. In both cases, we take into account the maximum envelope geometry model as the reference model in the rest of the present thesis.

The computed efficiency curves for the long and short iron blocks originating from the stochastically perturbed models for the maximum and minimum envelope geometries can be found in Appendix A.1

4.4.3 Activity results qualification approach

Qualification is a process used to evaluate the capacity of a model to predict physical quantities within a set of assumptions.

First, we want to assess the "real[27]" activity value within the waste item. For this purpose, we perform the GURU optimization of the efficiency calibration models in order to compare the reference model activities to the optimized models. Then, we want to quantify the uncertainties originating from the reference model assumption, on the activity values. By the quantification of uncertainties, we are able to construct correction factors applied to the activity values.

The aim is to quantify random errors and biases of a simplified geometry model. This is generally achieved by comparing a simplified reference model (model 0) with an optimized experimental model considered as the "best model" which represents the best knowledge we can have regarding a system. Based on the large set of perturbed geometry models with the PDF shown in Figure 4.9, we construct a correction factor (1+CF*(E)*) to apply to the reference model and to get an envelope activity value. This envelope value is identified with a confidence level of 97.5%.

The value of the correction factor (1+CF*(E)*) is determined in Equation 4.17, where CF*(E)* is equal to the uncertainty $\mathbb{B}$ + kσ represented by a systematic error, bias $\mathbb{B}$ and a random error, standard deviation σ in relative values [75][76]. Reference A_0*(E)* (blue line) is the activity of the reference model and A_p*(E)* is the activity of the envelope model (yellow line).

$$A_0(E)(1 + CF(E)) = A_p(E). \tag{4.17}$$

[27] It means actual. Hence, we can only get close to the activity value, never get it right due to uncertainties

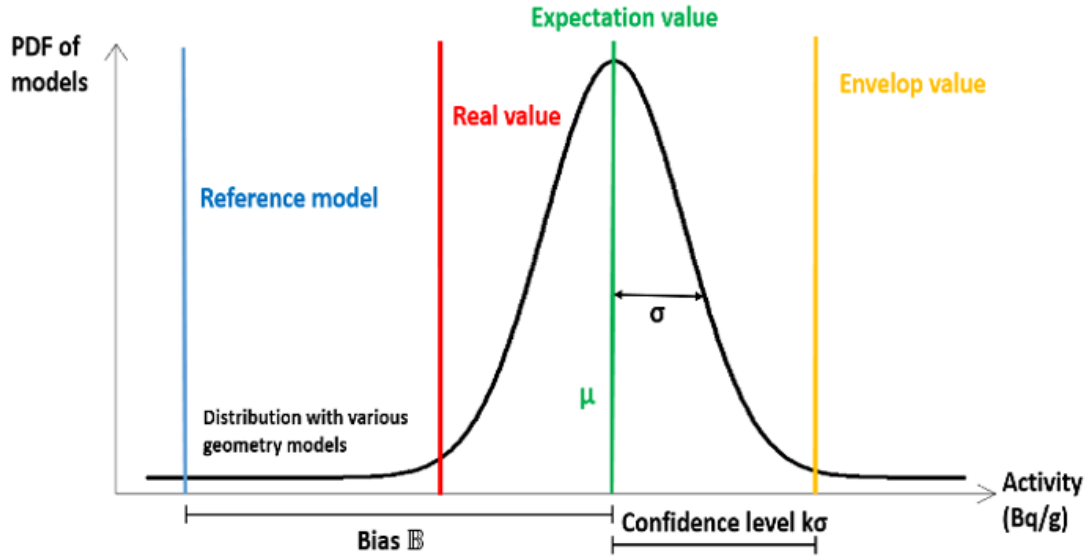

Figure 4.9: Schematic representation of the parameters involved in the qualification process.

As a first step, we evaluate the best estimate of the real activity value (red line) knowing the reference model (uniform source distribution). Afterwards, based on the vast set of perturbed geometry models, generated with IUE with the PDF, we construct a correlation factor (1+CF*(E)*) to apply to the reference model and obtain an envelope activity value (see Equation 4.17).
The correction factor can be negative as the envelope model can be lower than the reference model's activity value. In that case, the envelope activity value is assumed to be equal to the reference model value. Also, the real value can be located in anywhere in the statistical distribution.
Considering the measurements of multiple faces, we estimate the average of the activity results of opposite faces of the object. Equation 4.18 defines the relation between the reference model and envelope average activity values.

$$(A_0^1 + A_0^2)(E)(1 + CF(E)) = A_p^1(E) + A_p^2(E). \tag{4.18}$$

Where $A_p^1(E)$, $A_p^2(E)$ and $A_0^1(E)$, $A_0^2(E)$ respectively represent the activities calculated at energy E for opposite faces 1 and 2 of the object using the envelope and reference geometry models. Activity of $A_p^1(E)$ or $A_p^2(E)$ etc. can be expressed by Equation 3.20 (see Chapter 3).
The correction factor for the average activity values over two opposite faces can be formulated by the ratio of the efficiency calibration values of those two opposite faces as presented in Equation 4.19. The quantity $R(E) = \dfrac{A_0^2(E)}{A_0^1(E)}$ is the activity ratio of two opposite faces obtained with the reference model.

$$(1+CF(E)) = \frac{A_p^1(E)+A_p^2(E)}{A_0^1(E)+A_0^2(E)} = \frac{A_p^1(E)\dfrac{\epsilon_0^1(E)}{\epsilon_p^1}+A_p^2(E)\dfrac{\epsilon_0^2(E)}{\epsilon_p^2(E)}}{A_0^1(E)+A_0^2(E)} = \frac{\dfrac{\epsilon_0^1(E)}{\epsilon_p^1(E)}+R(E)\dfrac{\epsilon_0^2(E)}{\epsilon_p^2(E)}}{(1+R(E))} \tag{4.19}$$

4.4.4 Geometry optimization results

As mentioned in Section 4.3, within the ISOCS software, one computes the uncertainties, such as counting statistics, corrections due to acquisition dead time or gamma emission probabilities that contribute to the activity uncertainty. Additionally, in the present thesis, we focus on the uncertainty originating from the geometry modelling, such as material composition, dimensions and activity distributions.

4.4.4.A Distribution of efficiency calibration curves

IUE allows investigating the impact of the variations of one or more parameters of the item's geometry. The IUE software computes the efficiency values for energies ranging from 45 keV up to 3 MeV for the analyzed waste items. Each ensemble of computed efficiencies consists of 1000 models for which the parameters are sampled using a uniform distribution. The relative efficiency difference $\epsilon_{Rel.Diff}$ for each ensemble is given by Equation 4.20 [64]

$$\epsilon_{Rel.Diff} = \frac{\epsilon_{\text{model i}}}{\epsilon_{\text{ref model}}} - 1 = \frac{A_{\text{ref model}}}{A_{\text{model i}}} - 1. \tag{4.20}$$

Where $A_{\text{ref model}}$ and $A_{\text{model i}}$ are the activities of a radionuclide applying the efficiency calibration curve of the reference and i models. $\epsilon_{\text{ref model}}$ and $\epsilon_{\text{model i}}$ are efficiencies using reference and i models.

Equation 4.21 shows the corresponding standard deviation of the relative efficiency differences for 1000 models generated in IUE.

$$\sigma(\epsilon_{Rel.Diff}) = \sqrt{\frac{1}{1000}\sum_{i=1}^{1000}\overline{\epsilon}_{Rel.Diff} - \epsilon_{Rel.Diff}} \tag{4.21}$$

The distribution of efficiency calibration curves is analyzed for each detector face and summarized respectively for two iron blocks in Figures 4.10 and 4.11. For the long iron block, the efficiency calibration curves are overlapped for detector pair 1 and 2 or 3 and 4, because of similarity in the dimensions of faces and the source-to-detector distances.

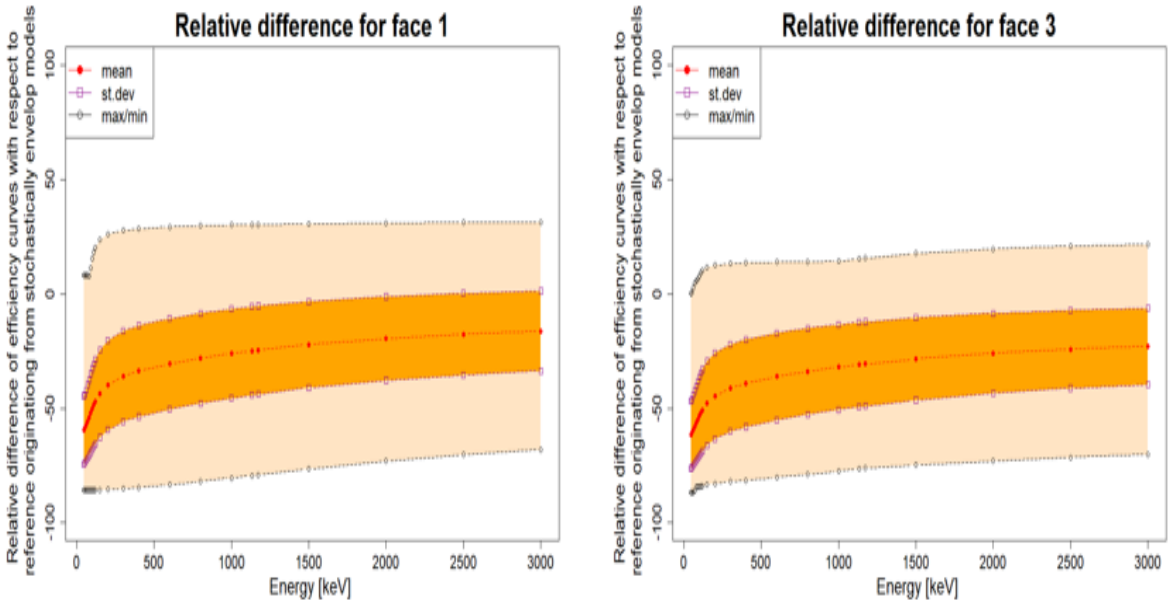

Figure 4.10: Relative efficiency difference (%) as a function of energy compared to the reference model. The yellow envelope presents the range of efficiency variations. The orange envelope describes the range of variations around the expectation value (red curve) at 1σ.

An important bias is observed as compared with the reference model for very low energies (e.g., -60% bias at 45 keV, with 15% standard deviation). When energy increases, the bias is reduced to -20 % at 3 MeV (standard deviation is around 17%). The computed average of efficiency curves which originate from models that have been stochastically perturbed, show that the activity would be higher by a factor ranging from 1.3 for higher energies to 2.6 for lower energies on face 3 and from 1.2 to 2.5 on face 1 in the energy range from 45 keV to 3 MeV. For characteristic gamma lines of commonly measured gamma emitters (Co-60, Na-22, etc.) in steel and aluminium dominated waste, the activity would be higher by a factor of 1.3 when compared with the reference model (a discrepancy which is commonly acceptable for the purpose of waste radiological characterization).

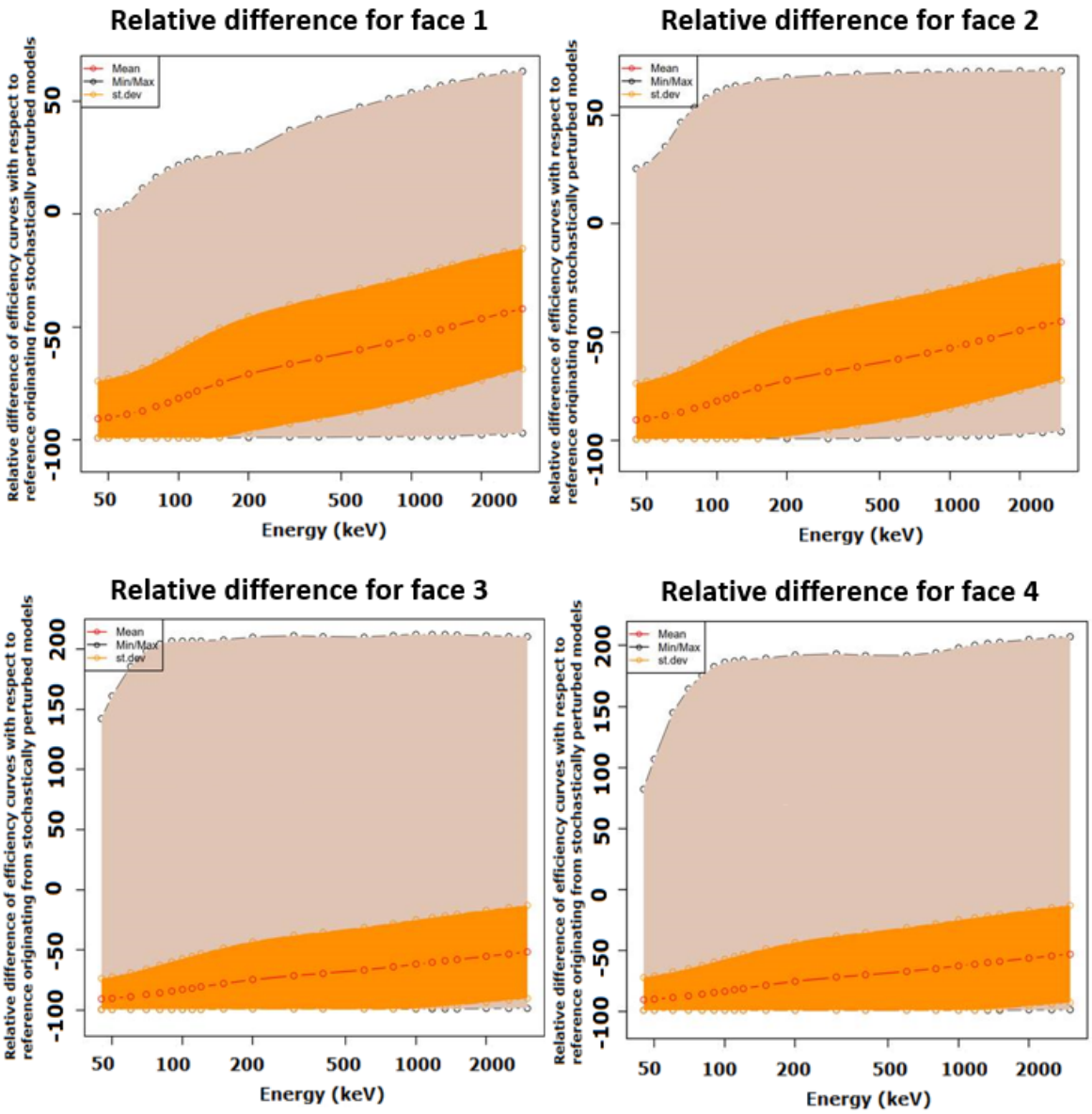

Figure 4.11: Relative efficiency difference (%) as a function of energy compared to the reference model. The brown envelope presents the range of efficiency variations. The orange envelope describes the range of variations around the expectation value (red curve) at 1σ.

For the short iron block, the important bias is of -85 % compared to the reference model. The standard deviation is around 15 % at 45 keV. One can observe, that the bias is reduced to -50 % at 3 MeV.

If we consider the measurement on each face independently, the most appropriate envelope value could have a relative difference to the reference model of -99.64 % even at energies above 2 MeV. As a result, the envelope activity value would be around 300 times higher than the reference efficiency for the same range of energies. Such results confirm that measuring only one face of a heterogeneous waste item can result in radionuclides not being detected on that one face, despite the presence and detectability on another face, as we can observe in the case

of Na-22 in faces 2 and 1 of the sample unit (see Table 4.4).
Additionally, the activity values of the entire set of 1000 models are presented in A.2.

4.4.4.B Reference and optimized geometry activity results

The multi-count activity ratios of the reference and optimized geometry models are presented in Figures 4.12 and 4.13. After geometry optimization the activity ratios converge to one, which means that the activity value obtained by measuring two opposite faces is consistent. Within the GURU framework, it is possible to vary the relative source concentrations of the hot spots (also referred to as the contrast). The contrast value is estimated as the ratio of the highest and lowest activities between the two opposite faces assuming a uniform source distribution. This quantity represents an estimate of the relative activity concentration variation range of the hot spots [55]. During the optimization process, the contrast parameter was varied from 1 to 100 or from 1 to 200 depending on the heterogeneity of the assay item. Obtained activity ratios from the gamma spectrometry measurements, with a uniform source distribution within the material matrix, as shown in Figures 4.12 and 4.13 are between 1.3 (for Co-60) and 17 (for Sc-44<Ti-44) for the long iron block and between 16 (for Co-60) and 297 (for Sc-44<Ti-44).

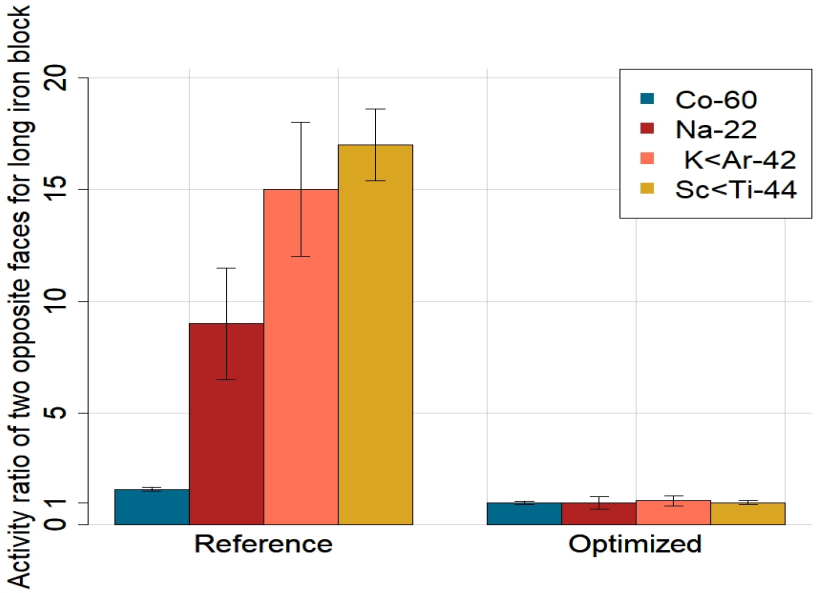

Figure 4.12: Activity ratio for opposite detectors faces before and after geometry optimization for the contrast ranging from 1 to 100 for the long item. The activity values after the geometry optimization for two opposite faces are consistent.

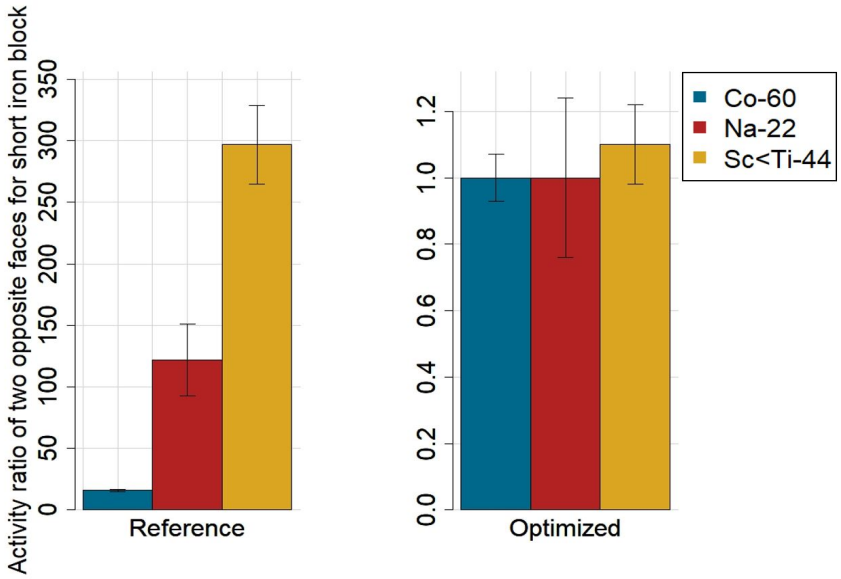

Figure 4.13: Activity ratio for opposite detectors faces before and after geometry optimization for the contrast ranging from 1 to 200 for the short item. The activity values after the geometry optimization for two opposite faces are consistent.

Since the optimization is performed over two faces at a time, we opted for averaging the results obtained for each pair of faces. The activity uncertainty of the average value is calculated as the square root of the quadratic sum of uncertainties corresponding to each single face. This ignores any correlations between activity values of each face. Table 4.6 below presents the average activity values of the reference and optimized models over two opposite faces and four faces for the waste items. We notice that averaging over four faces provides similar results compared to averaging over two faces. We systematically observe that averaging over the most active two opposite faces, leads to more penalizing results when compared to the four faces average results.

Table 4.6: Average activity over the two opposite faces with the highest dose discrepancies and four faces with reference and optimized models. Uncertainties are given at 1σ. Note that the reference activity result uncertainties do not take into account the geometry model uncertainty due to the less known parameters. N/A corresponds to unidentified radionuclides.

LONG IRON BLOCK

	REFERENCE		**OPTIMIZED**		**Ratio OPTIMIZED/REFERENCE**	
	Two opposite faces	**Four faces**	**Two opposite faces**	**Four faces**	**Two opposite faces**	**Four faces**
Co-60 [Bq/g]	2.36E+02 (4 %)	2.37E+02 (3 %)	4.58E+02 (4 %)	4.1E+02 (3 %)	1.94± 0.1	1.73 ± 0.06
Na-22 [Bq/g]	2.37E-01 (14 %)	2.01E-01 (8 %)	4.58E-01 (14 %)	3.55E-01 (8 %)	1.93± 0.37	1.76± 0.21
K-42<Ar-42 [Bq/g]	4.77E-01 (10%)	3.75E-01 (6%)	7.28E-01 (10 %)	5.67E-01 (6 %)	1.53 ± 0.21	1.51 ± 0.13
Sc-44<Ti-44 [Bq/g]	3.55E+00 (5 %)	2.87E+00 (3%)	5.22E+00 (5 %)	4.33E+00 (3 %)	1.47 ± 0.1	1.51 ± 0.07

SHORT IRON BLOCK

	REFERENCE		**OPTIMIZED**		**Ratio OPTIMIZED/REFERENCE**	
	Two opposite faces	**Four faces**	**Two opposite faces**	**Four faces**	**Two opposite faces**	**Four faces**
Co-60 [Bq/g]	1.35E+02 (5 %)	1.3E+02 (3 %)	2.49E+02 (4 %)	1.91E+02 (3 %)	1.84± 0.11	1.47± 0.06
Na-22 [Bq/g]	2.43E-01 (10 %)	N/A	1.79E-01 (12 %)	N/A	0.73± 0.11	N/A
K-42<Ar-42 [Bq/g]	1.55E-01 (10 %)	N/A	2.59E-01 (10 %)	N/A	1.67 ± 0.3	N/A
Sc-44<Ti-44 [Bq/g]	4.23E+00 (6 %)	2.66E+00 (4 %)	3.52E+00 (5 %)	3.29E+00 (4 %)	0.83 ± 0.07	1.24± 0.07

The comparison of the reference and optimized model activity values for both assay items allows us to select - as a final result - the values that correspond to the average of activities of opposite faces with the highest dose rate difference. This choice leads to a more conservative result. Even though, the dose rate ratio between opposite faces is approximately 2 (or 28) for the long item (or the short item), the ratios of the optimized to the reference average activity values are below a factor of 2 for Co-60. We conclude that the average of the uniform distribution activity underestimates by a maximum factor of 2 (see Table 4.6). In order to be conservative, we recommend establishing a safety factor represented as an additional systematic uncertainty of 50% on the average activity values using the reference models. We draw the attention of the reader that the above conclusions are confirmed only for bulky objects with attenuation thicknesses that are above $\sim$25 cm.

4.4.4.C Establishment of the envelope geometry model

We generate efficiency calibration curves with IUE and based on the qualification method described in Section 4.4.3 and compute a set of envelope correction factors (CF) taking into account different contrast values and different energies from 45 keV to 3 MeV.

Figure 4.14a presents the ratio between the "best estimate" value and reference value for Co-60 at 1173 keV for the long iron block. The ratio is 1.56 for the contrasts varies between 1-10 and 1.9 for the contrast between 1-80. The envelope to the reference values ratio is of 2.38 (contrast 1-10) and 6.89 (contrast 1-80). The optimized value is represented by the red line, the expectation value is represented by the green line and characterizes the bias due to a heterogeneous source distribution ($\mathbb{B}$=exp.value-1). The envelope value is represented by the yellow line and characterizes the random uncertainty due to a heterogeneous source distribution (kσ=pen.value-$\mathbb{B}$).

As illustrated in Figure 4.14b, the contrast ranges from 1 to 80 leading to a maximum ratio between the envelop and reference models of less than 10.

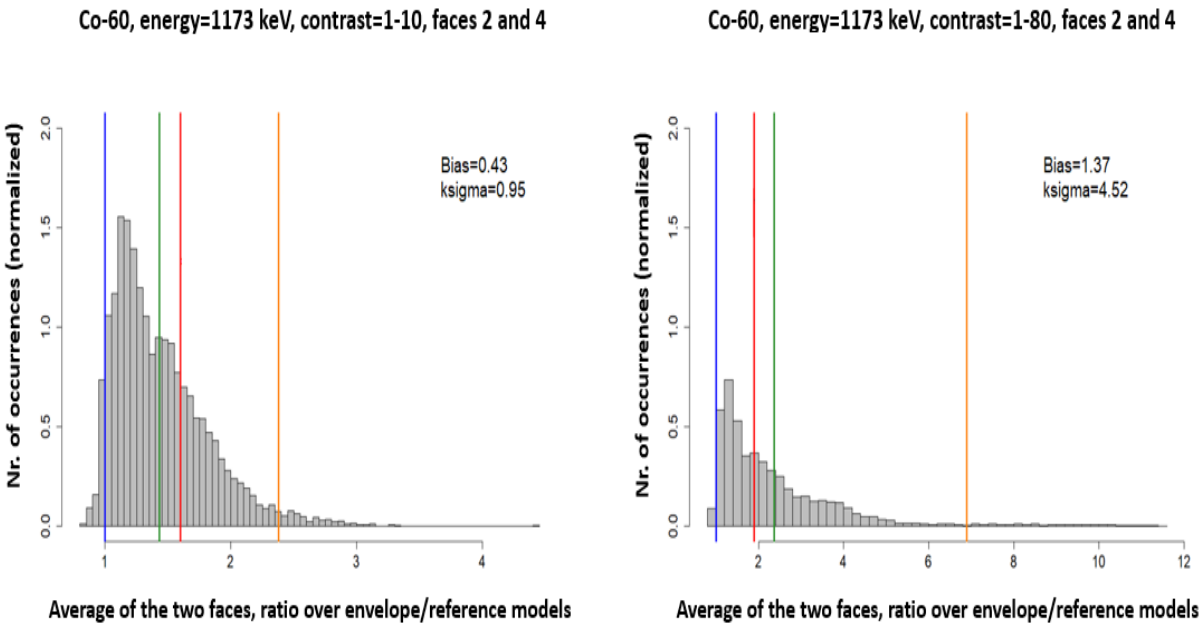

(a) Distribution of correction factors (1+CF(E)) normalized for the uniform distribution (reference model, blue line) for Co-60, 1173 keV. For the contrast ranging from 1 to 10, the expectation value (green) is 1.43, optimized (red) 1.56, and envelope (yellow) 2.38. For the contrast from 1 to 80, the expectation value (green) is 2.37, optimized (red) 1.9, and envelope (yellow) 6.89.

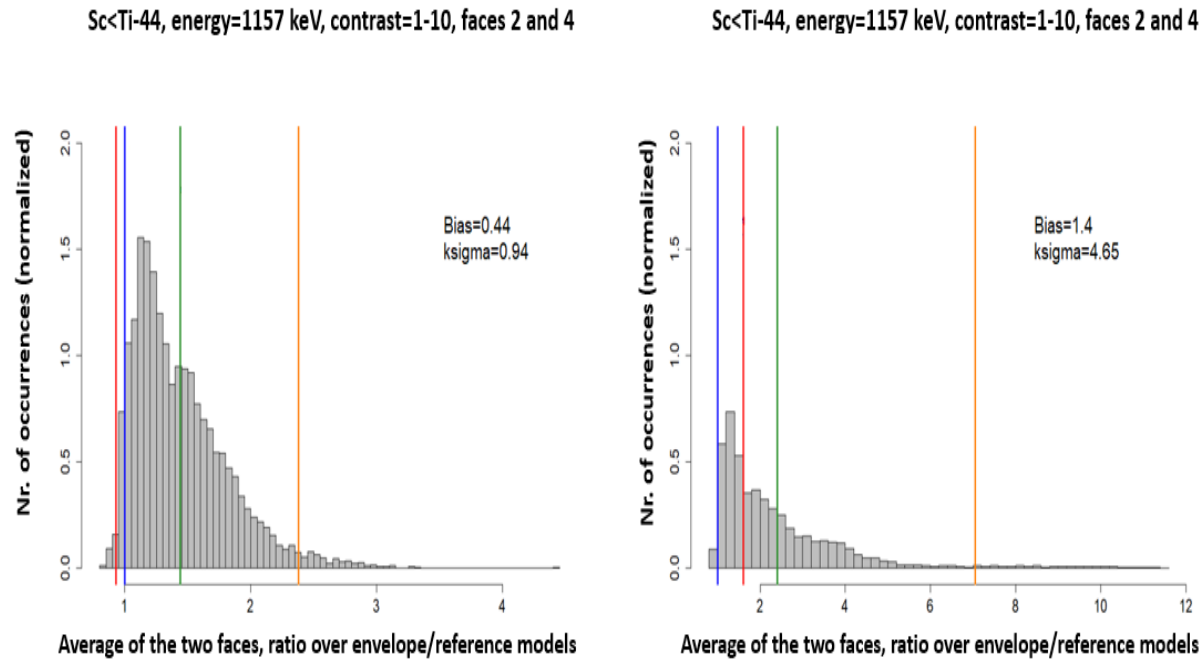

(b) Distribution of correction factors (1+CF(E)) normalized for the uniform distribution (reference model, blue line) for Sc<Ti-44. For the contrast ranging from 1 to 10, the expectation value (green) is 1.44, optimized (red) 0.93, and envelope (yellow) 2.38. For the contrast from 1 to 80, the expectation value (green) is 2.4, optimized (red) 1.6, and envelope (yellow) 7.05.

Figure 4.14: Distribution of correction factors (1+CF(E)) for Co-60 and Sc<Ti-44 radionuclides.

For the short iron block, Figure 4.15 presents the ratio between the "best estimate" value and the reference value. The ratio is 1.8 for Co-60 (the ratio of activities between faces 1 and 3 is around 16 for the uniform source distribution model). Also, the ratio between the envelope and reference models is of 7.05.

In the case of Sc-44<Ti-44, the ratio of the envelope CF and reference activity values is 73.57 for the considered contrast that ranges from 1 to 400.

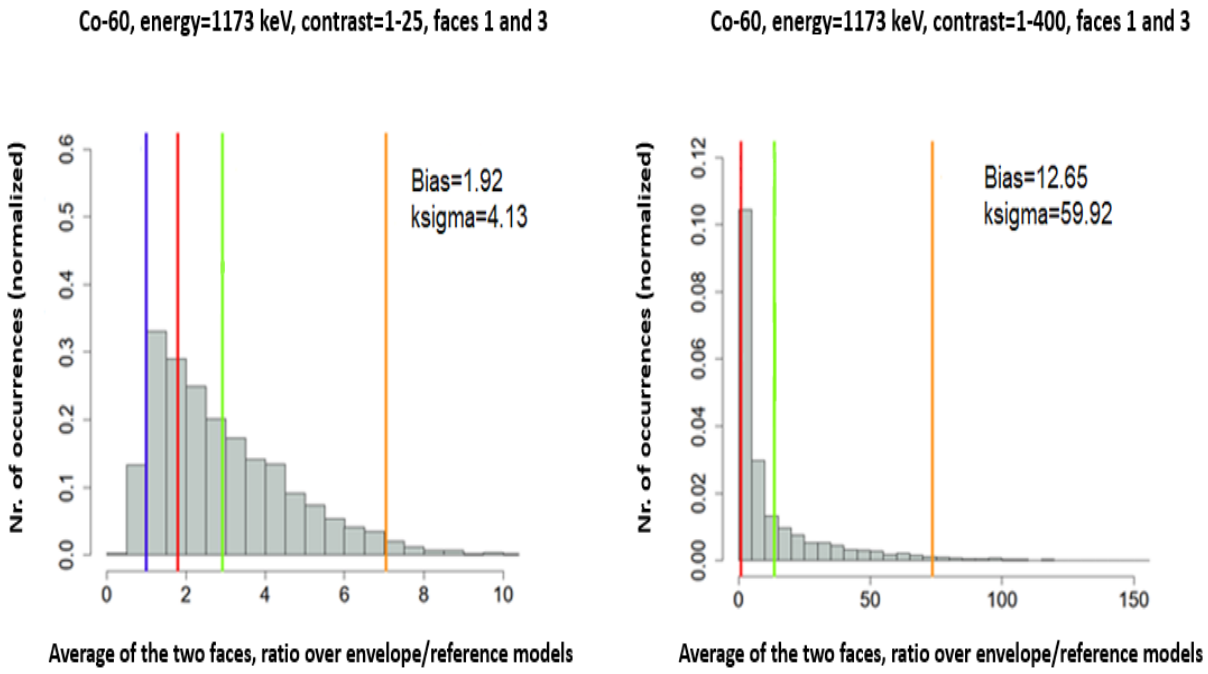

Figure 4.15: Distribution of correction factors (1+CF(E)) normalized for the uniform distribution (reference model, blue line) for Sc<Ti-44. For the contrast ranging from 1 to 25, the expectation value (green) is 2.92, optimized (red) 1.8, and envelope (yellow) 7.05. For the contrast from 1 to 400, the expectation value (green) is 13.65, optimized (red) 0.8, and envelope (yellow) 73.57.

446 In addition, Tables 4.7 and 4.8 present the envelope correction factor with a confidence level
447 97.5% for both different shapes, such as the long and the short iron blocks.

Table 4.7: Envelope correction factors (1+CF(E)) to consider as a function of energy and source distribution contrasts, for comparable shape and activity distribution of the long iron block.

Energy (keV)	**[1-10]**	**[1-80]**	**[1-100]**
45	4.7	36.6	45.3
50	4.7	36.1	44.9
60	4.6	34.1	42.8
70	4.4	31.7	39.2
80	4.2	29.7	36.6
90	4.1	28.2	35.3
100	4.0	26.5	33.4
110	3.9	25.3	31.7
120	3.8	24.0	30.0
150	3.6	20.6	25.3
200	3.3	16.9	20.1
300	3.1	13.3	14.8
400	2.9	11.4	12.5
600	2.7	9.7	10.5
800	2.6	8.5	9.1
1000	2.5	7.6	8.1
1157	2.4	8.4	7.5
1173	2.4	7.1	7.4
1274	2.4	6.9	7.3

Continued on next page

Table 4.7 – *Continued from previous page*

Energy (keV)	[1-10]	[1-80]	[1-100]
1332	2.3	6.6	7.0
1500	2.3	6.4	6.8
1525	2.2	6.0	6.2
2000	2.2	5.9	6.2
2500	2.1	5.0	5.2
3000	2.0	4.5	4.6

448

449 The correction factor is valid for comparable shapes and activity distributions of the waste items.
450 For instance, the correction factors (for Co-60) differ by a factor of 3 (for the long iron block)
451 for contrast ranges of [1-10] and [1-100].

Table 4.8: Envelope correction factors (1+CF(E)) to consider as a function of energy and source distribution contrasts, for comparable shape and activity distribution of the short iron block.

Energy (keV)	[1-10]	[1-25]	[1-50]	[1-100]	[1-200]	[1-400]
45	4.7	10.6	21.3	42.8	83.9	165.6
50	4.6	10.6	21.0	42.0	82.5	162.9
60	4.5	10.3	20.3	40.8	79.8	157.7
70	4.5	10.1	19.9	40.2	78.7	154.3
80	4.4	10.0	19.8	39.6	76.3	150.5
90	4.4	9.8	19.6	38.6	74.7	147.8
100	4.4	9.8	19.3	37.9	72.8	143.6
110	4.4	9.8	19.0	37.1	71.5	140.2
120	4.3	9.7	18.6	36.4	69.8	137.8

Continued on next page

Table 4.8 – *Continued from previous page*

Energy (keV)	**[1-10]**	**[1-25]**	**[1-50]**	**[1-100]**	**[1-200]**	**[1-400]**
150	4.2	9.4	18.1	34.4	66.5	129.6
200	4.1	8.9	17.2	32.4	62.0	119.7
300	3.9	8.5	16.0	30.3	57.0	109.3
400	3.8	8.3	15.5	29.2	54.6	102.9
600	3.7	7.9	14.7	27.2	49.7	93.6
800	3.6	7.6	13.9	25.2	45.9	84.8
1000	3.5	7.3	13.2	23.8	42.4	77.8
1173	3.5	7.1	12.7	22.6	40.3	73.6
1332	3.4	6.9	12.5	21.7	38.4	69.9
1500	3.3	6.7	12.2	21.1	36.8	66.0
2000	3.2	6.4	11.2	19.2	33.8	56.8
2500	3.2	6.1	10.5	17.9	30.6	50.2
3000	3.1	5.9	10.1	17.0	28.0	44.4

For the short iron block, the correction factor (for Co-60) differs by a factor of 21 for contrast ranges [1-10] and [1-400]. At lower energies, the efficiency is limited by the self-absorption of the photons and the photon absorption and attenuation in the detector dead layers. This faithfully reflected by Equation 4.19, for which we calculated the correction factor values as presented before.

In conclusion, the geometry optimization results allow the establishment of the optimized (or best) geometry models. These results are based on a robust methodology based on the FOM that rely on the multi-count and multi-line activity consistencies. The activity ratios for the opposite faces, using the reference model, vary from 1.3 to 17 for the long iron block and from 16 to 297 for the short one. After the optimization process, we obtain geometry models that lead to activity ratios that are consistent with the factor of 1 for contrasts ranging from 1 to 100 (for the long item) and from 1 to 200 (for the short item).

Additionally, we notice that the ratio between the average activity values of the optimized and

reference models differs by less than a factor of 2, even though the activity distribution is quite heterogeneous with optimized contrast values of 70 (for the long item). This result suggests that the use of a reference model (as compared with an optimized model) is adequate for the purpose of waste characterization with heterogeneously distributed activity. However, in order to be conservative, we recommend the introduction of an additional safety factor of 2 on the average activity values using the reference models.

Chapter 5

Evaluation of Experimental and Analytical Scaling Factors

This Chapter provides the list of radionuclides, as well as scaling factors needed to estimate the activity of the DTM and ITM radionuclides in ferrous waste prior to its elimination.

Section 5.1 describes the first step in establishing a radionuclide inventory. In particular, one performs analytical ActiWiz calculations for both LL/IL and VLL elimination pathways, following the acceptance criteria.

The following Section 5.2 gives an overview of the experimental validation of the radionuclide inventory for ETM radionuclides given by a large number of *In-Toto* gamma spectrometry measurements. Subsequently, Section 5.3 provides the sampling strategy to quantify the number of samples needed to estimate the experimental SF for metallic LL/IL waste, such as steel, aluminium, and copper. This Section also focuses on the validation of the experimental and analytical SFs, for DTM and ITM radionuclides respectively.

Section 5.4 presents a statistical analysis needed to investigate the distribution of activity ratios of the DTM and KN radionuclides. The calculations are carried out for both sampling campaigns: for metallic VLL and LL/IL waste at CERN. We perform a statistical analysis to determine the SF distributions and validate whether the VLL and LL/IL sample sets belong to the same statistical distribution.

The application of the LL/IL radiological characterization methodology, developed at CERN, is presented in Section 5.5. We give an example of the output waste packages analyzed following this developed methodology. In particular, one presents the total beta-gamma specific activity for the first container that is planned to be eliminated in the frame of the MAST pilot elimination project at CERN. In addition, we describe the qualification calculations of the gamma spectrometry results for a 2.7 m^3 container with emphasis on the geometry optimization activity results.

5.1 Radionuclide inventory - ActiWiz calculations

This Section describes the first step of the radiological characterization of waste at CERN, which consists of establishing the list of expected radionuclides for ferrous metals.
This inventory is based on the computation of induced radioactivity in ferrous metals (including cast iron, low-carbon steel and stainless steel, which in the rest of this thesis will be referred to as "steel"). The computations are performed with the analytical code ActiWiz version 3.3.148/2018-0603, which relies on extensive Monte Carlo simulations carried out with the code FLUKA. In particular, the core functionalities of ActiWiz (e.g., calculation of nuclide production rates and decay chains) were accessed via the PyraGen software [99] by means of specifically developed Python programs. More details on the input parameters of the calculations and the predicted results are provided in the next sections.

5.1.1 ActiWiz Scenarios setup - Elemental composition and irradiation conditions

Steel is assigned a standard chemical composition taken from the CERN catalogue of materials, with a view to being representative of the majority of the waste items to be characterized (see Steel 304L, Table 3.1). The exact elemental composition of the metal will vary considerably depending on the considered waste item. Variations of trace elements weight fractions can be found even among metallic pieces taken from the same waste package.
The calculations are carried out for seven representative locations during irradiation which are the following:

- at the beam impact area;
- within bulky materials (e.g., magnet) surrounding the beam impact area;
- adjacent to bulky materials (e.g., magnet) surrounding the beam impact area;
- close to the concrete tunnel wall (beam loss in bulky material);
- behind massive concrete shielding;
- at 10 cm lateral distance to target;
- close to the concrete tunnel wall (beam on target).

The primary proton beam is assigned 5 different energies/momenta: 160 MeV, 1.4 GeV, 14 GeV/c, 400 GeV/c and 7 TeV in order to cover the entire energy spectrum of the proton accelerator complex at CERN. The irradiation times are set to 4 months, 1 year, 3 years, 10 years and 30 years while the cooling times are set to 3, 10 and 30 years.

5.1.2 Analytical predictions of the radionuclide inventory of the metallic LL/IL waste

The radionuclide inventory is the list of radionuclides produced in a given waste item, with activity levels that can exceed the declaration thresholds of VLL or LL/IL waste. The first step towards establishing the radionuclide inventory consists of simulating 525 different activation scenarios[28] (see Section 5.1.1) using ActiWiz and scoring the complete list of the produced radionuclides and their specific activities per primary proton.
In this Section, we define the ETM and DTM/ITM radionuclides as indicated in the SHEaR Process Assessment (SHERPA) campaign for steel waste [90]. SHERPA is a campaign for the sustainable compressing and shearing of metallic waste that originate from the hadron and electron machines at CERN before their elimination in the French final repositories for VLL waste.
The distinction between DTM and ITM radionuclides depends on their importance for the radiological characterization: if a radionuclide contributes by more than 1% to the total value of IRAS it is considered as a DTM provided that it can be measured experimentally, otherwise it is classified as an ITM. It should be noted that the activity limits used in the calculation of IRAS are typically the same for DTM and ITM radionuclides. Therefore the radionuclides which we identified as DTM are the ones with the highest contribution to the total activity. From this point of view, we can describe an ITM as a nuclide whose level of activity is so low, that its measurement would be at the same time difficult and unjustified considering its low importance for the radiological characterization. The study indicates the radionuclide inventory for three cases detailed in the following sub-sections.

5.1.2.A VLL pathway

The steps below presents the steps to determine the VLL radionuclide inventory:

- For each activation scenario, we normalize the complete list of radionuclides and their specific activities to the maximum acceptable activity for VLL waste (i.e., IRAS = 10, [23]

- We select the radionuclides with normalized specific activities that are above the declaration threshold for at least one activation scenario. The resulting list is referred to as the "VLL potential radionuclides".

- Every ETM radionuclide that is a VLL potential radionuclide, is included in the VLL radionuclide inventory.

- For each radionuclide pertaining to the list of "VLL potential radionuclides" and for each activation scenario, we calculate the activity ratio to the corresponding Co-60 value. We

[28] 7(location) x 5(energy) x 5(irrad time) x 3(colling time)

then calculate the geometric means of the activity ratios, averaging over all the activation scenarios. Finally, we renormalize the average activity ratios to IRAS = 10 as computed for the entire list of potential radionuclides.

- Every DTM/ITM radionuclide that is in the list of VLL potential radionuclides and that has renormalized specific activities above the VLL declaration threshold are included in the VLL radionuclide inventory.

The final VLL radionuclide inventory therefore includes all the ETM "VLL potential radionuclides", and all the DTM/ITM "VLL potential radionuclides" whose average, renormalized specific activities are above the VLL declaration thresholds.

5.1.2.B LL/IL pathway

In the case of LL/IL waste, the radionuclide inventory is determined as follows:

- For each activation scenario, we normalize the complete list of radionuclides and their specific activities to the maximum acceptable activity for LL/IL waste (i.e., 37 kBq/g of total activity [22]).

- We select the radionuclides with normalized specific activities that are above the declaration threshold for at least one activation scenario. The resulting list is referred to as the "LL/IL potential radionuclides".

- Every ETM radionuclide that is a LL/IL potential radionuclide, is included in the radionuclide inventory.

- For each nuclide pertaining to the "LL/IL potential radionuclides" list and for each activation scenario, we calculate the activity ratio to the corresponding Co-60 value. We then calculate the geometric means of the activity ratios averaging over all activation scenarios. Finally, we renormalize the average specific activity ratios to 37 kBq/g of the total specific activity.

- Every DTM/ITM radionuclide that is in the list of LL/IL potential radionuclides and that has renormalized specific activities above the LL/IL declaration threshold are included in the radionuclide inventory.

The final LL/IL radionuclide inventory therefore includes all the ETM "LL/IL potential radionuclides", and all the DTM/ITM "LL/IL potential radionuclides" whose average, renormalized specific activities are above the LL/IL declaration thresholds.

5.1.2.C VLL and LL/IL elimination pathways combination

The retained radionuclide inventory for the combined VLL and LL/IL pathways, presented here, includes every radionuclide that is relevant for at least one elimination pathway (i.e., that is part of the VLL or LL/IL inventories). However, we notice that the radionuclide inventory for VLL waste turns out to be a subset of the inventory for LL/IL waste.

The application of a more conservative activity limit for LL/IL waste (i.e., 20 kBq/g[29] instead of 37 kBq/g) would not change the radionuclide inventory.

The list of predicted radionuclides using ActiWiz is presented in Table 5.1.

Table 5.1: The list of the radionuclide inventory consisted of 525 different activation scenarios for VLL and LL/IL waste .

	VLL pathway				**LL/IL pathway**			
Potential ETM radionuclides	Co-60	Co-57	Ti-44	Mn-54	Co-60	Co-57	Ti-44	Mn-54
	Na-22				Na-22	Ar-42		
Potential DTM radionuclides	H-3	Fe-55			H-3	Fe-55		
Potential ITM radionuclides	Ni-63	Ar-39	Ni-59	C-14	Ni-63	Ar-39	Ni-59	C-14
	Ca-41	V-49	Cl-36	Be-10	Ca-41	V-49	Cl-36	Be-10
					Si-32	Mn-53		

[29] The specific activity of 20 kBq/g refers to the activity limit of the melting facility [48].

5.2 RN Inventory Experimental validation with Gamma spectrometry

The validation of the radionuclide inventory for ETM radionuclides is based on the experience gained in the elimination of over 2'000 m^3 metallic waste from hadron and electron machines at CERN within the SHERPA project carried out between 2016 and 2019 and within the MAST project.

In particular, at the time of the SHERPA project over 2'000 *In-Toto* gamma spectrometry measurements were performed for the radiological characterization of the corresponding waste packages. The *In-Toto* gamma spectrometry measurements were performed at 75 cm from the lateral faces of each package, with the detector pointing to the centre of the face.

Additionally, during the MAST project, the gamma spectrometry measurements are performed for unitary items, such as pipes (Figure 2.4b), ion pumps (Figure 2.4c), and containers 2.7 m^3 (Figure 4.3b).

Naturally-Occurring radionuclides (e.g., K-40, Ra-226 and Th-232), artificial radionuclides which are part of the background radiation (e.g., Cs-137 from nuclear tests in the atmosphere) are not included in the present study.

Every radionuclide detected in the gamma spectrometry measurements (both in VLL and LL/IL waste) is part of the ETM radionuclides list that is analytically predicted (see Section 5.1.2). Hence, we conclude the accuracy of the activation models, used to predict the radionuclide inventory, described in this Chapter.

5.3 Experimental and Analytical Scaling factors

In this Section, we describe the sampling strategy, i.e. the statistical approach adopted to quantify the number of samples that will be used to estimate global experimental scaling factors for metallic LL/IL waste.
In Section 5.3.2, we present the current approach (at the time of writing this thesis), in order to estimate the specific activity of DTM radionuclides. Subsequently, Section 5.3.3 focuses on the analytical SF, based on the ActiWiz computations, as presented in Section 5.1

5.3.1 Sampling strategy of LL/IL waste

The activation mechanisms[30] of metallic VLL and LL/IL waste might be similar as they depend on the same input parameters, i.e. beam energy, locations within the tunnel complex, irradiation and cooling times. The experience gained at CERN during recent years on the characterization of VLL metallic waste is therefore useful for predicting important radionuclides for LL/IL radiological characterization, as well as for estimating the appropriate number of samples to collect in view of quantifying scaling factors. The current experience with VLL waste suggests that the KN in steel and copper is Co-60. Nevertheless, we recommend that the gamma spectrometry analyses, performed on the samples, should also cover the other dominant ETM radionuclides (Na-22, Ti-44 and Mn-54), in case one of them turns out to be a better key nuclide. Indeed, we can expect Mn-54 to dominate in steel shielding with only few traces of Ni and Co, and Ti-44 to dominate for long waiting times (>30 years).
The radionuclides listed before are systematically quantified via DA and NDA measurements when characterizing VLL waste. As a consequence, a large number of activity values have been determined for these radionuclides and can be used to estimate their expected variability as well as the dispersion of the scaling factors, which are activity ratios of DTM and ETM radionuclides. The dispersion (expressed as standard deviation) is one of the two parameters needed when quantifying the number of samples that should be collected to estimate the scaling factors of LL/IL waste, the other parameter being a pre-specified margin of error that we are willing to accept on the final scaling factors.
The calculation process based on the Central Limit Theorem (CLT) [52], which says that for a large enough sample size n, the distribution of the sample mean tends to a normal distribution, as determined in Equation 5.1.

$$Z_n = \frac{\overline{x} - \mu}{\sigma/\sqrt{n}} \sim \mathcal{N}(0,1). \tag{5.1}$$

[30] the principle of activation (low-energy neutron capture, spallation etc.) might be the same for similar positions in the accelerator (at the beam impact area). However, the beam losses might be different, which depend on the beam optics or the loss mechanisms of the specific machine or operation mode.

The transformation of Equation 5.1 that leads to the sample size formula is presented in the following Equations 5.2a and 5.2b

$$P\left(\frac{-d}{\sigma/\sqrt{n}} \leq z \leq \frac{d}{\sigma/\sqrt{n}}\right) = 1 - \alpha \tag{5.2a}$$

$$\frac{d}{\sigma/\sqrt{n}} = z_{1-\alpha/2} \tag{5.2b}$$

Finally, Equation 5.3 describes the relationship between the number of samples to collect n, the dispersion σ and the acceptable margin of error d.

$$n = \left(\frac{z_{1-\alpha/2} \cdot \sigma}{d}\right)^2 \tag{5.3}$$

In Equation 5.3, the $z_{1-\alpha/2}$ score is a factor that allows us to express the probability of coverage under a normal distribution (meaning that 90% of the data points are included in the range $\mu \pm 1.64\sigma$, where μ is the mean of the normal distribution, and $z_{1-\alpha/2}$ is equal to 1.64).
Although σ is unknown, it can be estimated using the measurements performed on the VLL metallic waste and this estimation can be made for each of the three material types considered here (namely, aluminium, steel and copper) and each DTM/ETM pair. For the calculations, only the pairs H-3/Na-22 in aluminium and H-3/Co-60 in both steel and copper are considered. Table 5.2 shows the estimates of σ ($\hat{\sigma}$= s where s is the experimental standard deviation of the scaling factors obtained from the VLL waste) together with the estimated number of samples for each material type. The margin of error was arbitrary set for three materials (steel, aluminium and copper) to try to cover the range of experimental SFs.

Table 5.2: Estimated number of samples per material type.

Material	Standard deviation ($\hat{\sigma}$= s)	Margin of error (d)	Number of samples (n)
Aluminium	112	36	30
Steel	26	4	100
Copper	24	7	30

In the case of aluminium, the scaling factor for H-3/Na-22 has a large spread, which would lead to a comparatively large number of samples if we applied a margin of error similar to steel and copper. However, the amount of aluminium waste to be characterized is relatively low. Therefore, we decided to accept a higher margin of error in order to keep the number of samples adequate with respect to the other materials.

5.3.2 Experimental scaling factors (DTM radionuclides)

Currently, we do not have yet a significant number of samples, hence we chose to use the VLL metallic samples, where over 300 samples were measured via radiochemical analyses and gamma spectrometry in the frame of the SHERPA elimination project [34] in 2016 and 2017. They were taken from radioactive metals irradiated in CERN's proton machines and with cooling times longer than 3 years. The samples were measured via gamma spectrometry to evaluate the activities of key nuclides (in the case of steel: Co-60), and via radiochemical analysis for the activity of DTM radionuclides (in the case of steel: H-3 and Fe-55). Each DTM radionuclide was therefore associated with a set of activity ratios, namely one activity ratio per sample. These sets of activity ratios follow a log-normal distribution, where the value at the third quartile was conservatively chosen as the reference scaling factor. The corresponding scaling factor values for H-3 and Fe-55 are presented in Table 5.3.

5.3.3 Analytical scaling factors (ITM radionuclides)

The analytical scaling factors are based on the extensive ActiWiz calculations described in Section 5.1. For each ITM radionuclide, we took the geometry average of the specific activity predicted in all activation scenarios and normalized the average specific activity to 1 Bq/g of the key nuclide (i.e., Co-60). The analytical scaling factors were calculated also for the DTM radionuclides and compared with the experimental scaling factors [90]. The comparison shows that on average the experimental values are a factor of 2.7 higher than the analytical predictions. This discrepancy is possibly due to the fact that all activation scenarios considered with ActiWiz were assigned the same probability, whilst some of the sampled radioactive waste shared similar radiological history (e.g. in case of waste produced during one particular dismantling campaign). In the rest of this study we will therefore apply a corrective factor of 2.7 to all analytical scaling factors for ITM radionuclides.
In order to determine the final list of ITM radionuclides, we verify if their geometric average activity value is above the declaration threshold of LL/IL waste for the maximum specific activity of 37 kBq/g and Co-60 as the KN. The final list of ITM radionuclides and their corresponding SF values with a corrective factor can be found in Table 5.3.

5.3.4 Recommended Scaling Factors and total activity determination for LL/IL waste

For the evaluation of the activity of ETM radionuclides, the scaling factors are not used as the activity of these radionuclides is assessed via *In-Toto* gamma spectrometry. For DTM radionuclides, we apply the experimental SF from SHERPA (steel with more than 3 years of cooling time) corresponding to the third quartile of the SF statistical distribution [90]. For ITM radionuclides, we apply the analytical SF calculated as the product of the analytical geometric means

and a corrective factor of 2.7.

The complete radionuclide inventory, along with the recommended scaling factors for DTM and ITM radionuclides, can be found in Table 5.3. These values can be used for the characterization of radioactive steel to be shipped to the melting facility prior to elimination as VLL or LL/IL waste.

Table 5.3: Radionuclide inventory (ETM, DTM and ITM radionuclides) and recommended scaling factors (DTM and ITM radionuclides) for Steel. The scaling factors (SF) are based on Co-60 as key nuclide. The scaling factors are not applicable to ETM radionuclides, because the activity of these radionuclides will be evaluated via gamma spectrometry.

ETM	**DTM**		**ITM**	
	Radionuclide	SF	Radionuclide	SF
ETM radionuclides are identified and quantified via	H-3	5.1	Be-10	1.00E-06
direct measurements using gamma spectrometry.	Fe-55	19	Cl-36	1.80E-05
Gamma emitters often found in metallic waste are			Ar-39	1.40E-02
Co-60, Ti-44, Na-22, Mn-54 and Co-57.			Ca-41	7.50E-05
			V-49	1.00E-03
			Ni-59	1.50E-02
			Ni-63	1.3
			Si-32	8.50E-04

The total specific activity $A^{TOT}_{\beta,\gamma}$ of the beta- and gamma-emitting radionuclides listed in Table 5.3, is calculated using Equation 5.4, below where:

- M is the mass of the waste package;
- a_e is the specific activity of the ETM radionuclide e, which is measured with gamma spectrometry. The sum is over all the ETM radionuclides in the inventory;
- $a_{(Co-60)}$ is the specific activity of the key nuclide Co-60, measured with gamma spectrometry;
- SF_d is the SF for the DTM radionuclide d;
- SF_i is the SF for the ITM radionuclide i.

$$A^{TOT}_{\beta,\gamma} = M\Big(\sum_{e=ETM} a_e + \sum_{d=DTM} a_{Co-60} \cdot SF_d + \sum_{i=ITM} a_{Co-60} \cdot SF_i\Big). \tag{5.4}$$

Regarding the radionuclide activity limits, the primary LL/IL waste will only comply with the maximal $A_{\beta,\gamma}^{TOT}$ activity of 20 kBq/g of the MAST project [48]. Hence, no other radionuclide-specific limit will be applied, including – for example – individual coating thresholds as laid down in the ANDRA specifications for LL/IL.

5.4 VLL and LL/IL Experimental Scaling Factors statistical analysis

The aim of this section is to perform a statistical test analysis of the both the VLL and LL/IL SF distributions and verify the normality of the LL/IL SF.

We remind the reader of the set of first-order differential equations, known as Bateman equations [36] that describe the case of several radionuclides forming a linear decay and build-up chain, as presented in Equation 5.5.

$$\frac{dN_i}{dt} = -\lambda_i N_i + \lambda_{i-1} N_{i-1} + P_i. \tag{5.5}$$

Where N_i denotes the concentration of a given radionuclide and λ_i is the decay constant of *i*th radionuclide. Yet, it is crucial to consider the nuclide continuous production via the production rate P_i. The production rate depends on the elemental composition of the irradiated material, the particle flux and the nuclear cross sections. Additionally, any complex decay chain can be broken into a set of linear radioactive decay chains [51].

The solution of the Bateman equations is applicable in forming an expression that describes the SF between a DTM and a KN as the product of three factors, given in Equation 5.6

$$SF_i = \frac{a_{DTMi}}{a_{KNi}} = \frac{P_{DTMi}}{P_{KNi}} \times \frac{(1 - e^{-\lambda_{DTM} t_{irradiation}})}{(1 - e^{-\lambda_{KN} t_{irradiation}})} \times \frac{e^{-\lambda_{DTM} t_{cooling}}}{e^{-\lambda_{KN} t_{cooling}}}. \tag{5.6}$$

The first term of Equation 5.6 describes the ratio of production rates of the DTM and the KN. The second term contributes to the build-up of the radioactivity of DTM and the KN during irradiation time span (the particle beam is present). The decay term denotes the time spans after the end of the exposure (cooling time).

The evaluation of the parameters that contribute the most to the SF values has been demonstrated in [121] (Chapter 3). The study shows that the cooling time is the dominant parameter. As presented in Equation 1.9, the cooling term is an exponential function of the cooling time, meaning that any normal distribution of the cooling time may lead to a log normal distribution of the decay term [123]. Accordingly, the distribution of the SF values calculated analytically and experimentally at CERN follows a log normal distribution [112].

The analysis of the distribution of activity ratios of the DTM and the KN determined experimentally over multiple disposal campaigns at CERN are describe as follows.

One can distinguish two ways of testing normality: numerical and graphical. Numerical methods are based on, for example, skewness or statistical tests of normality. The complementary methods are graphical methods, which visualize the distribution of the variables. Graphical and numerical methods fall into descriptive or theory-driven statistics [98]. In order to examine the distribution of the scaling factors for Steel waste, we perform:

- Histogram, which is a graphical method that belongs to descriptive statistics[31].

- Skewness, which is a numerical method that belongs to descriptive statistics. It measures the degree of the symmetry of the probability distribution. The skewness for a normal distribution is zero. Positive values of the skewness indicate that experimental data are skewed right. In the case of negative values, data are skewed left. The skewness values computed in the present thesis are defined by the SAS and SPSS computing packages [78]. The formula for skewness is complemented by an adjustment for sample size. The adjustment approaches 1 as N is large. The formula is given in Equation 5.7

$$G_1 = \frac{\sqrt{N(N-1)}}{N-2} \frac{\sum_{i=1}^{N}(x_i - \overline{x})^3/N}{s^3}. \tag{5.7}$$

where x_i represents the value of a random sample i, $\overline{x}$ is the mean value, s is the standard deviation, and N is the sample size.

- Q-Q (quantile-quantile) plot, which is a graphical method that belongs to theory-driven statistics[32]. It compares the quantiles of the variable with the quantiles that follows the theoretical distribution (i.e., the normal distribution). The straight line represents the normal distribution. If both distribution (experimental and theoretical) match, the points on the plot will follow this straight line.

- Shapiro-Wilk test, W test [107], which is a numerical method that belongs to theory-driven statistics. The W statistic is defined by Equation 5.8 [106] that determines the ratio of the best estimator of the variance to the sum of squares of the observations about the sample mean. The sample size of the W statistic should be greater than 7.

$$W = \frac{\left(\sum_{i=1}^{N} a_i x_i\right)^2}{\sum_{i=1}^{N}(x_i - \overline{x})^2}. \tag{5.8}$$

Where the exact value of the constant a is given by Equation 5.9

$$a = (a_1, a_2, ..., a_n) = (m^T V^{-1} V^{-1} m)^{-1/2} m^T V^{-1}. \tag{5.9}$$

Where m is the vector of expected values of the standard normal order statistics and V is the corresponding n $\times$ n covariance matrix. Also, for W value being closer to one, the more normal distributed the sample is.

[31] Descriptive statistics give brief information about variables. They consist of two basic categories of measures. For instance, mean median or mode measure the central tendency of a variable, while measures of dispersion include standard deviation ,range or interquartile (IQR).

[32] Theory-driven statistics are based on both empirical and theoretical distributions. Theory-driven statistics compare an empirical distribution function of the variable with the particular theoretical distribution function either in graphical methods (Q-Q plot) or numerical methods (Shapiro-Wilk test).

306 The following analysis focuses on the DTM SF values that are used to estimate the total specific
307 activity $A^{TOT}_{\beta,\gamma}$ of the beta- and gamma-emitting radionuclides (see Table 5.3). The analysis of
308 the SF distribution are based on the steps presented before. Figures 5.1 and 5.2 shows the SF
309 distribution of the H-3/Co-60, and the Fe-55/Co-60 respectively.

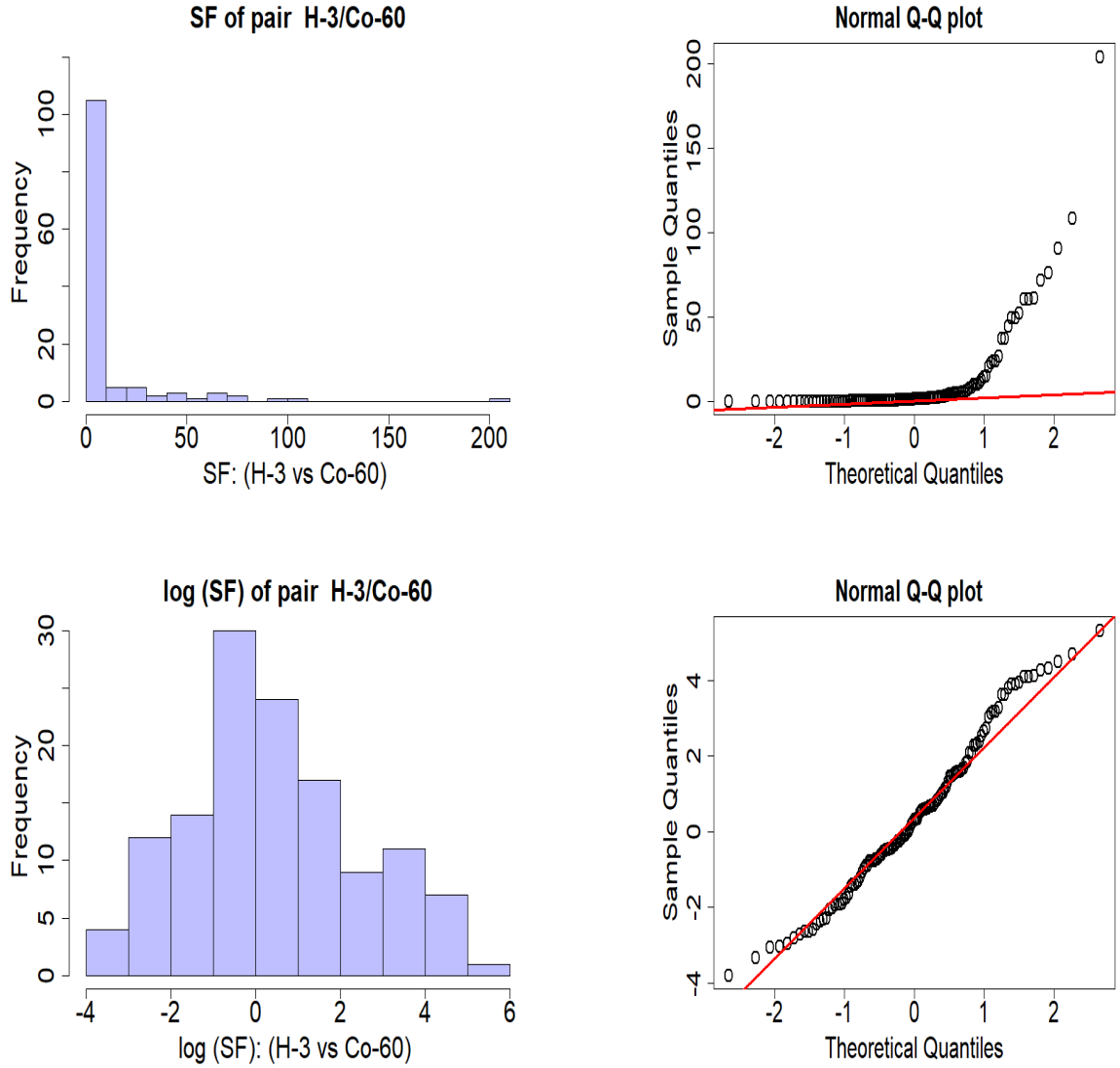

Figure 5.1: Histograms and Q-Q plots of cumulated scaling factors for pair of H-3 and Co-60 for 129 samples of activated Steel.

310 As illustrated in Figure 5.1, the data after the logarithmic transformation can be approximated
311 via a normal distribution. Table 5.4 presents other statistical tests that we performed.

Table 5.4: Summary of the SF analyses of the of H-3 and Co-60 pair for activated Steel.

SF of pair H-3/Co-60, n=129				
Mean	10.5		**Median**	1.4
Standard deviation	26		Q_1	0.4
Geometric mean	1.5		Q_3	5.1
Geometric st dev	7.7		**Correlation**	0.46
	non log-transformed data		**log-transformed data**	
Skewness	4.46		0.28	
W test	**W**	0.44	**W**	0.98
	p-value	2.2E-16	**p-value**	0.06
	reject normality		cannot reject normality	

The skewness values for both non- and log-transformed data are positive. However, the skewness value of the log-transformed data is close to zero, which indicates the data are fairly symmetrical. Additionally, we performed W tests, where the null hypothesis of the W test assumes that the sample distribution is normal. If the test is significant, the distribution is non-normal [65]. For the p-value $>$0.05, the data distribution is not significantly different from a normal distribution. Hence, one can assume the normal distribution for the log-transformed data (for p-value=0.06).

319 Figure 5.2 depicts the histograms and Q-Q plots before and after logarithmic transformation for
320 the SF of the Fe-55 and Co-60 pair.

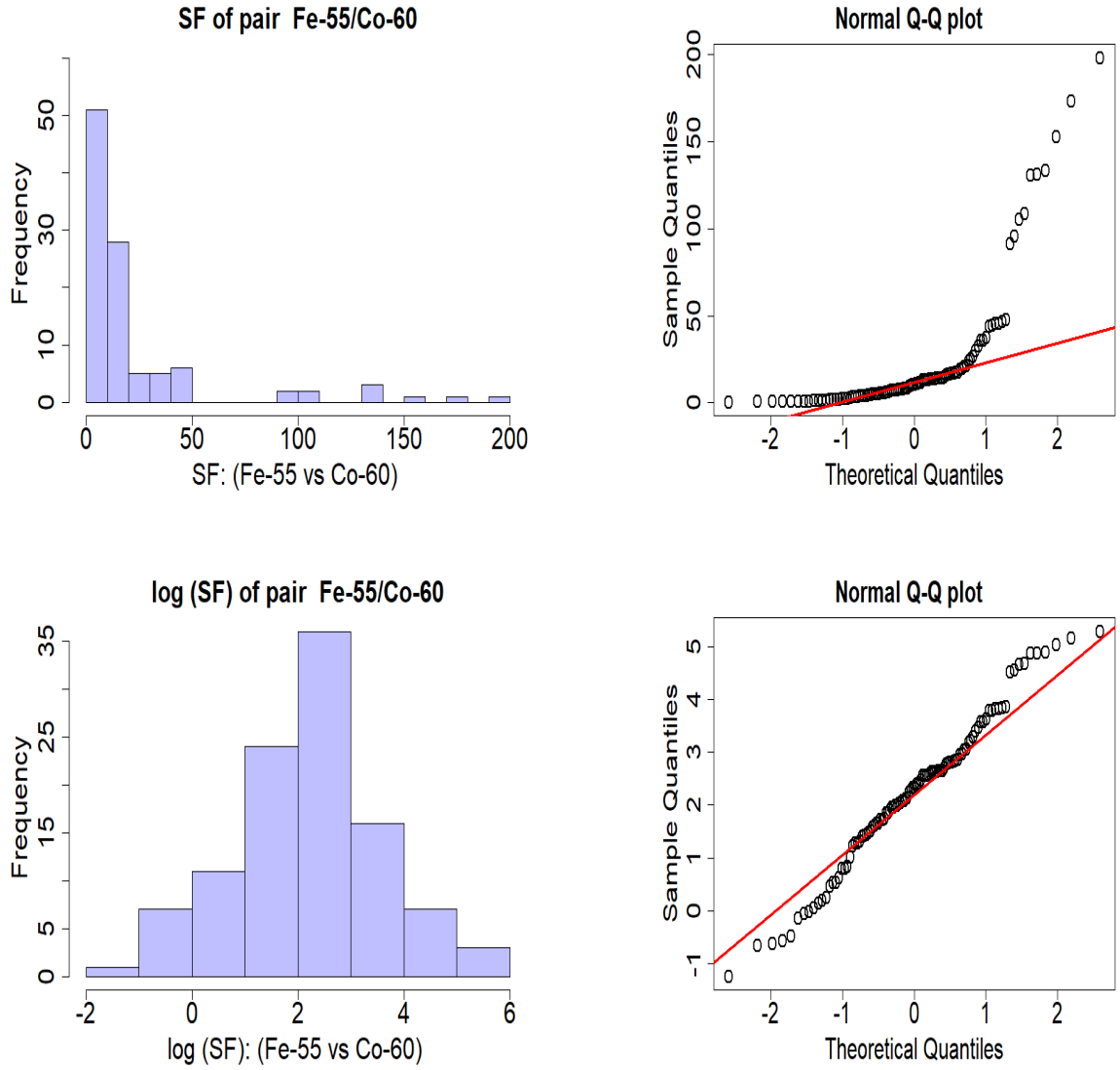

Figure 5.2: Histograms and Q-Q plots of cumulated scaling factors for pair of Fe-55 and Co-60 for 105 samples of activated Steel.

321 In Table 5.5, we summarize the the analysis performed for samples collected for VLL waste at
322 CERN.

Table 5.5: Summary of the SF analyses of the Fe-55 and Co-60 pair for activated Steel.

SF of pair Fe-55/Co-60, n=105				
Mean	24		**Median**	10.3
Standard deviation	38.5		Q_1	4.2
Geometric mean	9.5		Q_3	19
Geometric st dev	4.1		**Correlation**	0.71
	non log-transformed data		**log-transformed data**	
Skewness	2.75		-0.08	
W test	**W**	0.59	**W**	0.98
	p-value	1.1E-15	**p-value**	0.25
	reject normality		cannot reject normality	

The skewness for the log-transformed data indicates the tail in the negative direction. The skewness value is close to zero meaning that the data are fairly symmetrical. The W test for the log-transformed data shows that, for the p-value equal to 0.25, the data distribution is not significantly different from the normal distribution.

In the radiological workflow (see Figure 3.21), we can distinguish a step that focuses on collecting a representative sample ensemble from the waste population and analyzing them either by NDA or DA techniques. Within the present thesis, the phase of collecting LL/IL samples is still ongoing. The collected and analyzed Steel LL/IL samples at the time of writing this thesis is 25. The following calculations are based on the experimental SFs for H-3 and Fe-55 as DTM and Co-60 as a KN obtained from those 25 samples.

First, we analyze the SFs of pair H-3 and Co-60. As depicted in Figure 5.3, the data after the logarithmic transformation follows the normal distribution.

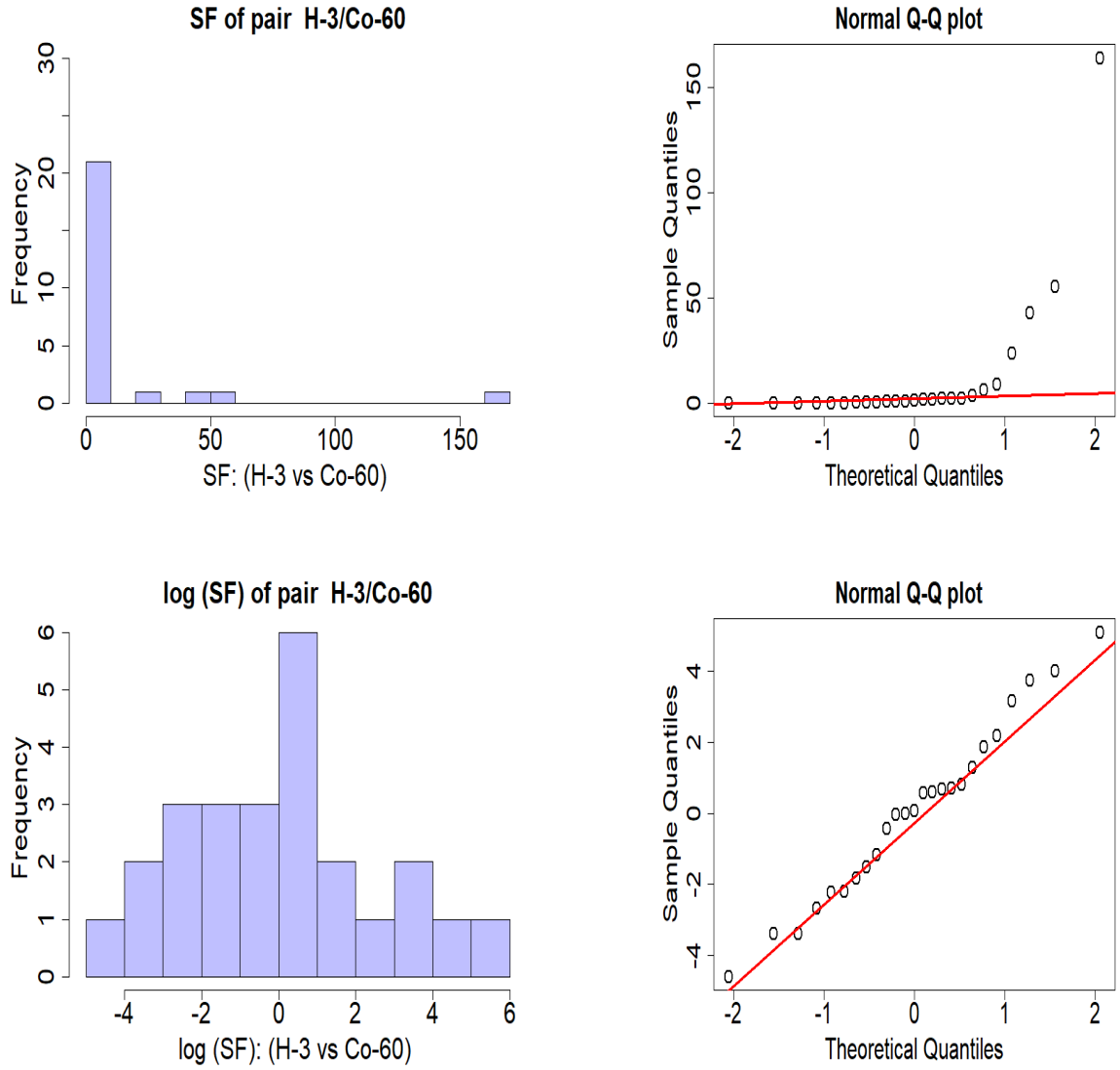

Figure 5.3: Histograms and Q-Q plots of cumulated scaling factors for pair of H-3 and Co-60 for 25 samples of activated Steel.

Additionally, the numerical methods, such as the skewness and W test indicate that data are normally distributed. The skewness value is 0.15 (data are fairly distributed) and the p-value for the W test is 0.91 meaning that we cannot reject the null hypothesis, which assumes that the sample distribution is normal. The analyzed data are presented in Table 5.6

Table 5.6: Summary of the SF analyses of the H-3 and Co-60 pair for activated Steel (from LL/IL waste).

SF of pair H-3/Co-60, n=25				
Mean	13		**Median**	1.1
Standard deviation	35.5		Q_1	0.2
Geometric mean	1.1		Q_3	3.6
Geometric st dev	11.9		**Correlation**	-0.13
	non log-transformed data		**log-transformed data**	
Skewness	3.9		0.15	
W test	**W**	0.41	**W**	0.98
	p-value	6.5E-09	**p-value**	0.91
	reject normality		cannot reject normality	

While performing the analysis for the SFs of the Fe-55 and Co-60 pair, we rejected one sample. Indeed, the SF for this sample differs from the rest by two orders of magnitude, and can be considered as an outlier. It might be due to activation mechanisms where the production rate of Co-60 may be very high, e.g. in the high flux region [10] compared with the production rate of the Fe-55.

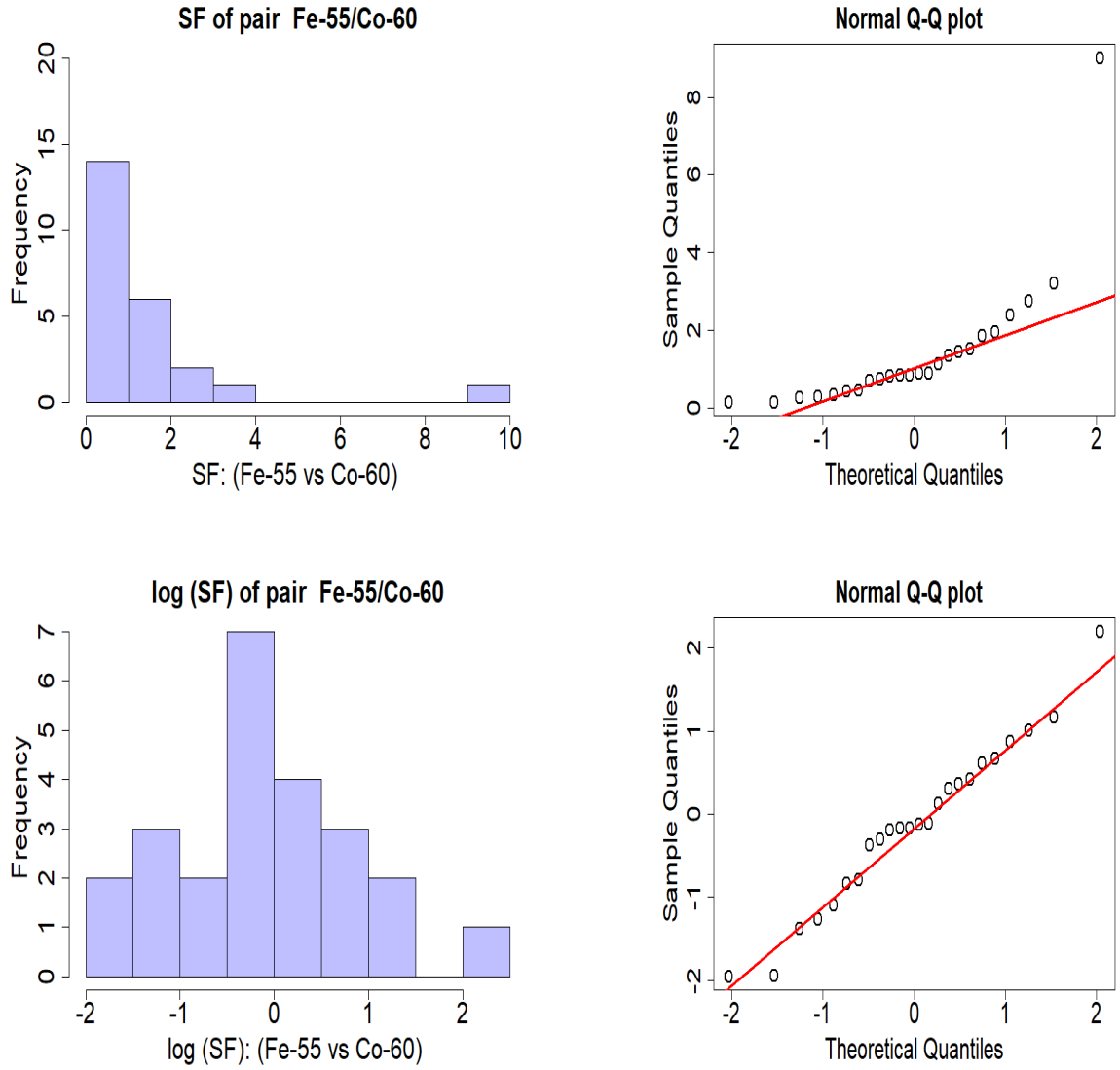

Figure 5.4: Histograms and Q-Q plots of cumulated scaling factors for pair of Fe-55 and Co-60 for 24 samples of activated Steel.

As depicted in Figure 5.4, the skewness values for log-transformed data are positive and its value is close to zero, which indicates the data are fairly symmetrical. Additionally, the p-value of the W test is 0.87, meaning that we cannot reject the null hypothesis that assumes the normal distribution of the SFs for Fe-55 and Co-60. The summary is presented in Table 5.7.

Table 5.7: Summary of the SF analyses of the H-3 and Co-60 pair for activated Steel (from LL/IL waste).

SF of pair Fe-55/Co-60, n=24				
Mean	1.4		**Median**	0.9
Standard deviation	1.8		Q_1	0.4
Geometric mean	0.9		Q_3	1.6
Geometric st dev	2.7		**Correlation**	0.98
	non log-transformed data		**log-transformed data**	
Skewness	3.4		0.05	
W test	**W**	0.61	**W**	0.98
	p-value	7.98E-07	**p-value**	0.87
	reject normality		cannot reject normality	

In what follows, we will test whether the two arbitrary sample sets (VLL and LL/IL) originate from the same distribution. The Kolmogorov-Smirnov test (KS test) is performed in order to determine if two sample distributions are identical, meaning that their corresponding values of the Empirical Cumulative Distribution Function (ECDF) are similar [54]. The ECDF of m observable data points (e.g. SF) defined, at any real number x is given by Equation 5.10

$$F_m(x) = \frac{1}{m}\sum_{j=1}^{m} \mathbf{1}\{X_j \leq x\}, \tag{5.10}$$

where, **1** represents the indicator function, that **1** is one if $\{X_j \leq x\}$ and zero otherwise [91]. X_j are the independent and identically distributed data points (e.g. SFs).
The null hypothesis assumes that the ECDF of the CERN's sample campaigns, $F_m(x)$ and $G_n(x)$ respectively are equal ($F = G$). The KS test is based on the maximum difference, the statistical test $D_{m,n}$ is given by Equation 5.11 [104]

$$D_{m,n} = sup_x|F_m(x) - G_n(x)|, \tag{5.11}$$

where the supremum is considered as a maximum discrepancy between the two distributions. If the maximum difference for $D_{m,n}$ is 1, it might mean that two distributions are not identical. Additionally, we perform the two-sample t test (Welch's t test)[117] in order to investigate if the difference between the means of CERN's sample campaigns is significant (or between medians, in so called mediantest[33]). The null hypothesis assumes that the means of two sample campaigns are identical. The Welch t-statistic is determined by Equation 5.12

$$t = \frac{\overline{X} - \overline{Y}}{\sqrt{(s^2_{\overline{X}}/n_X + s^2_{\overline{Y}}/n_Y)}}. \tag{5.12}$$

Where $\overline{X}$ and $\overline{Y}$ are sample SFs mean value of CERN's sample campaigns , $s_{\overline{X}}$, $s_{\overline{Y}}$ are standard deviations of the SFs, and n is the number of the SF points of the two distributions X and Y respectively.
If the p-value is below the assumed significance level, one can reject the null hypothesis. While for p-values above the significance level, there is not sufficient evidence to reject the null hypothesis.

[33] https://rdrr.io/cran/nonpar/man/mediantest.html, 28 July 2021

The following calculations present both tests of normality and investigate whether the two distributions are identical. At the beginning, we analyze Steel LL/IL and VLL samples collected to determine experimental SF (H-3 and Fe-55).

The performed tests investigating the difference between means or medians showed that there is not enough evidence to conclude that the means and medians of SF(H-3/Co-60) for Steel samples LL/IL and VLL are different at a significance level of 0.05 (mean p-value=0.76, median p-value=0.82).

According the KS test, the p-value is 0.73, indicating that we cannot reject the null hypothesis that two distributions are equal. Additionally, Figure 5.5, shows the ECDF for both SF distributions.

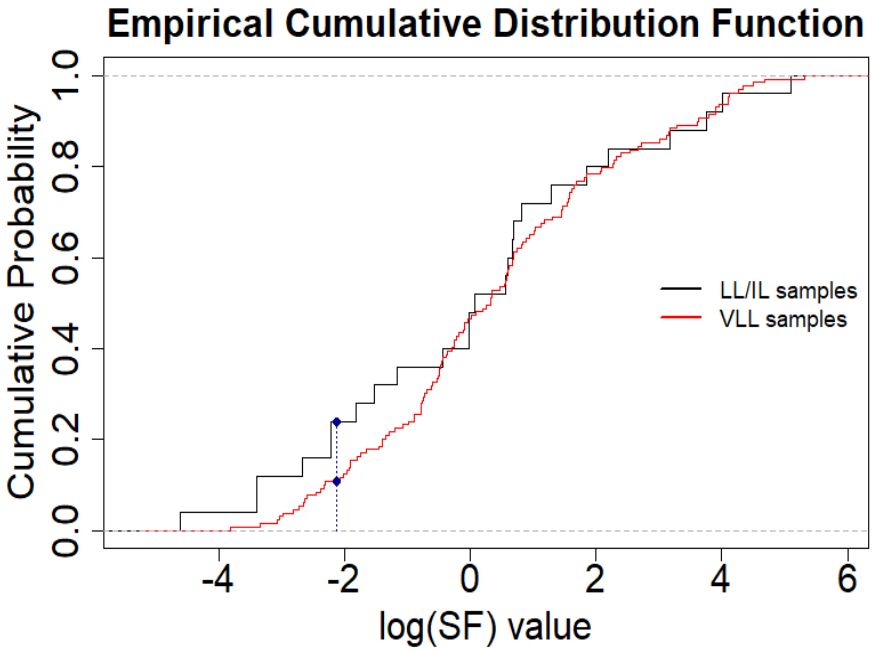

Figure 5.5: The Empirical Cumulative Distribution Function for two distributions for SF of pair H-3/Co-60; LL/IL and VLL samples respectively. The maximum discrepancy between the distributions is D=0.14.

Subsequently, one investigates whether the SF for Fe-55 for LL/IL and VLL sample distributions are identical. The test for means and medians showed that p-values are below significance level of 0.05, indicating that we can reject the null hypothesis (mean p-value=4E-08, median p-value=5E-07).The KS test presents the p-value at 4.3E-12, which demonstrates that the distributions for both LL/IL and VLL samples are not equal, even if both sample campaigns follow the normal distribution. Figure 5.6 depicts the ECDF with the maximum discrepancy between distributions, D=0.77.

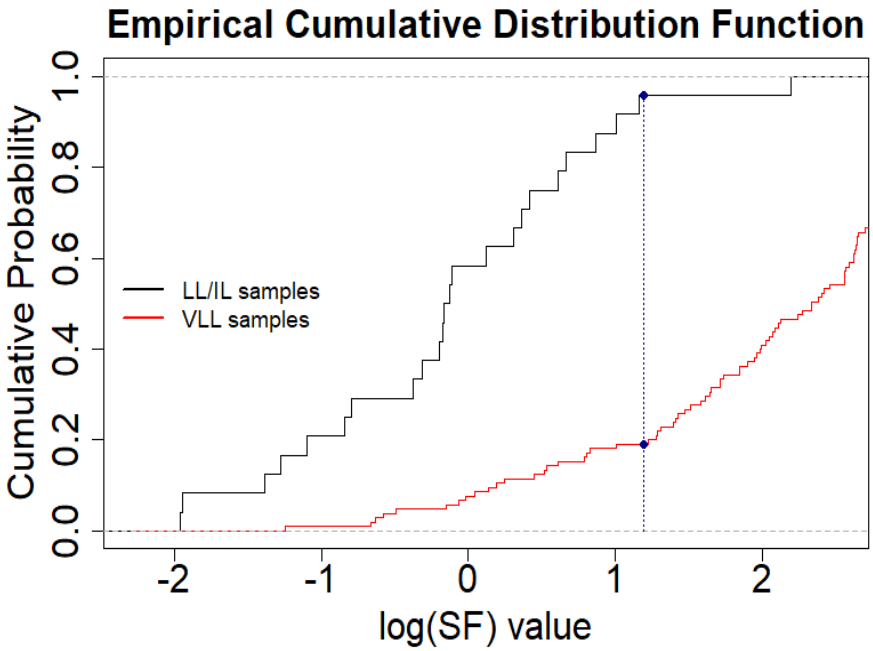

Figure 5.6: The Empirical Cumulative Distribution Function for two distributions for SF of pair Fe-55/Co-60; LL/IL samples and VLL samples respectively. The maximum discrepancy between distributions is D=0.77.

Thus, one might conclude that the Steel LL/IL and VLL samples distributions for SFs for H-3 are equal and follow the normal distribution (see Tables 5.4 and 5.6). The combined SF distributions are presented in Figure 5.7 and the summary of the analyses, including statistical tests (W test) is given in Table 5.8.

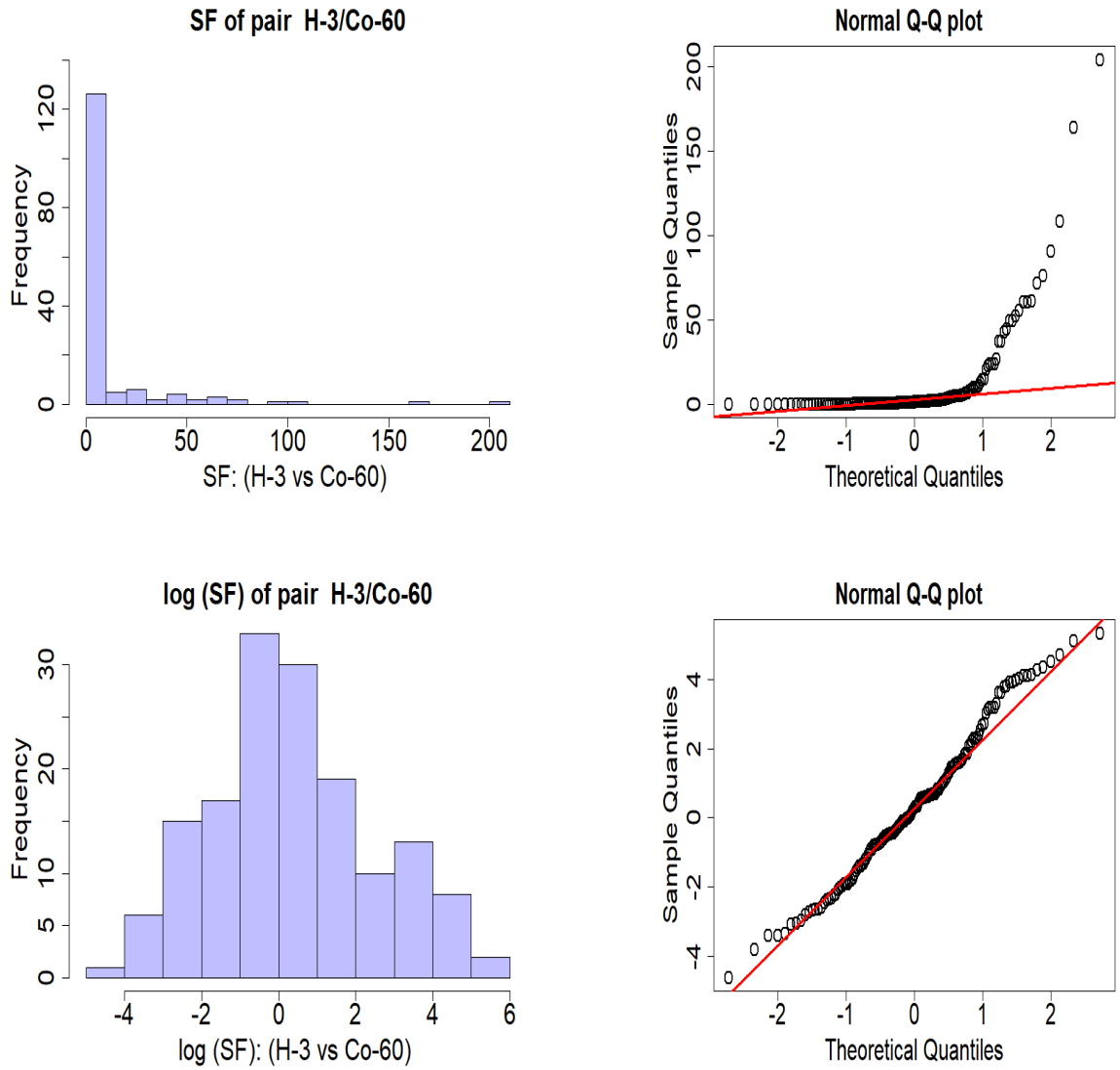

Figure 5.7: Histograms and Q-Q plots of cumulated scaling factors for pair of H-3 and Co-60 for 154 samples of activated Steel.

Table 5.8: Summary of the SF analyses of the H-3 and Co-60 pair for activated Steel.

SF of pair H-3/Co-60, n=154				
Mean	11		**Median**	1.3
Standard deviation	27		Q_1	0.3
Geometric mean	1.4		Q_3	5.0
Geometric st dev	8.3		**Correlation**	0.02
	non log-transformed data		**log-transformed data**	
Skewness	4.3		0.2	
W test	**W**	0.43	**W**	0.98
	p-value	2.2E-16	**p-value**	0.1
	reject normality		cannot reject normality	

However, the tests performed for the SF of Fe-55/Co-60 demonstrated that the SF distributions for LL/IL and VLL samples are not identical. It might be caused by the differences in the production rate of Co-60 and Fe-55 in CERN's accelerator materials, as well as the impact of the cooling time on the SF values.

In the next step of the analysis, we extracted the SF values from VLL sample campaigns carried out until 2020, specifically selecting those where the specific activity of Co-60 is greater than 10 Bq/g, where the value of 10 Bq/g which is the detection threshold for LL/IL waste given by ANDRA.

As presented in Figure 5.8, both distributions; LL/IL and VLL ($\geq$10 Bq/g) for the SF of H-3 and Co-60 can be identical. Taking into account the p-value of the KS test, we cannot reject the null hypothesis that two distributions are identical (p-value=0.54). In addition, tests of the means and medians show that the means and medians of the distributions are not significantly different (mean p-value=0.78, median p-value=0.5).

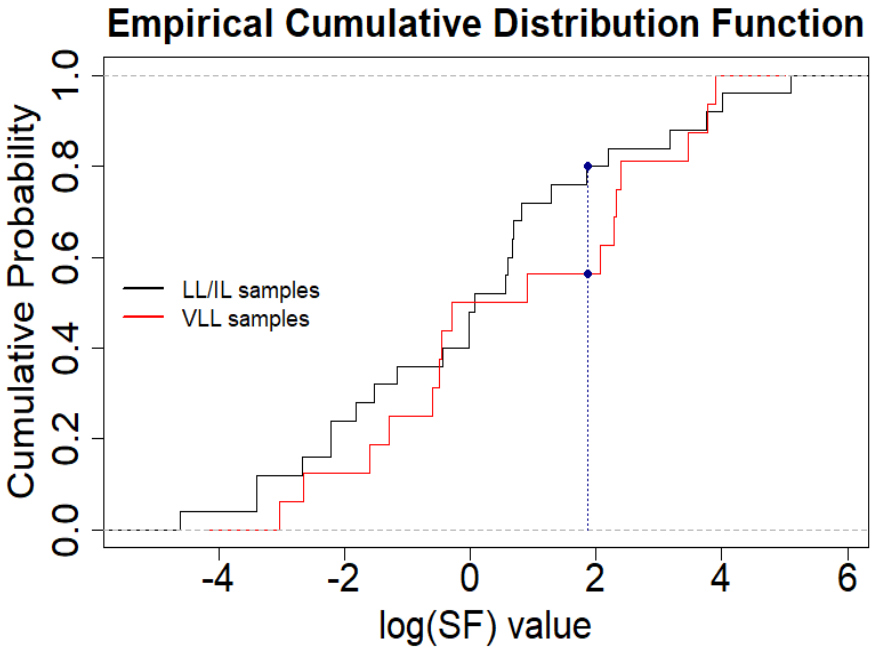

Figure 5.8: The Empirical Cumulative Distribution Function for two distributions for SF of pair H-3/Co-60; LL/IL and VLL (for samples with Co-60 specific activity greater than 10 Bq/g) samples respectively. The maximum discrepancy between distributions is D=0.23.

Additionally, Figure 5.9 and Table 5.9 present the summary of the normality test performed using the combined SFs of H-3 and Co-60 from the LL/IL and VLL ($\geq$10 Bq/g) samples.

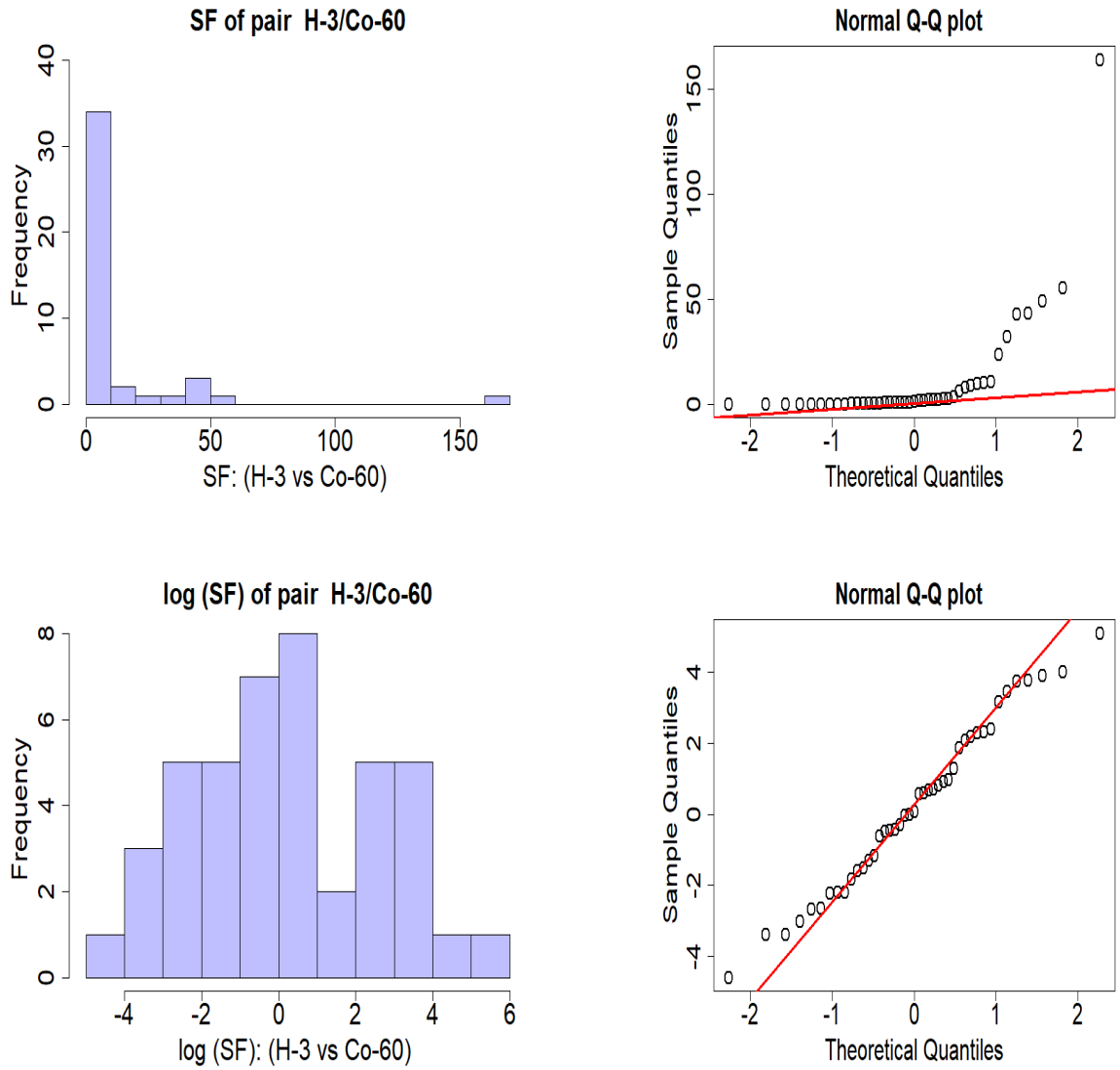

Figure 5.9: Histograms and Q-Q plots of cumulated scaling factors for pair of H-3 and Co-60 for 43 samples of activated Steel.

A positive skewness indicates that the size of the right-handed tail is larger than the left-handed tail. After logarithmic transformation, the skewness value indicates that the data are fairly symmetrical. The W test demonstrates, with the p-value equal to 0.71, one cannot reject the normal distribution hypothesis.

Table 5.9: Summary of the SF analyses of the H-3 and Co-60 pair for activated Steel.

SF of pair H-3/Co-60, n=43				
Mean	11.5		**Median**	1.1
Standard deviation	28		Q_1	0.2
Geometric mean	1.3		Q_3	8.5
Geometric st dev	10.6		**Correlation**	-0.07
	non log-transformed data		**log-transformed data**	
Skewness	4.3		0.07	
W test	**W**	0.45	**W**	0.98
	p-value	1.6E-11	**p-value**	0.71
	reject normality		cannot reject normality	

A similar analysis for the SF of Fe-55 and Co-60 is performed. Based on the KS test, one can conclude that the distributions of the SF are identical, p-value is 0.15. Also, the Welch's t test indicates that the means for two distributions are not significantly different, as well as for the median test (mean p-value=0.16, median p-value=0.17). Figure 5.10 depicts the ECDF of the SFs.

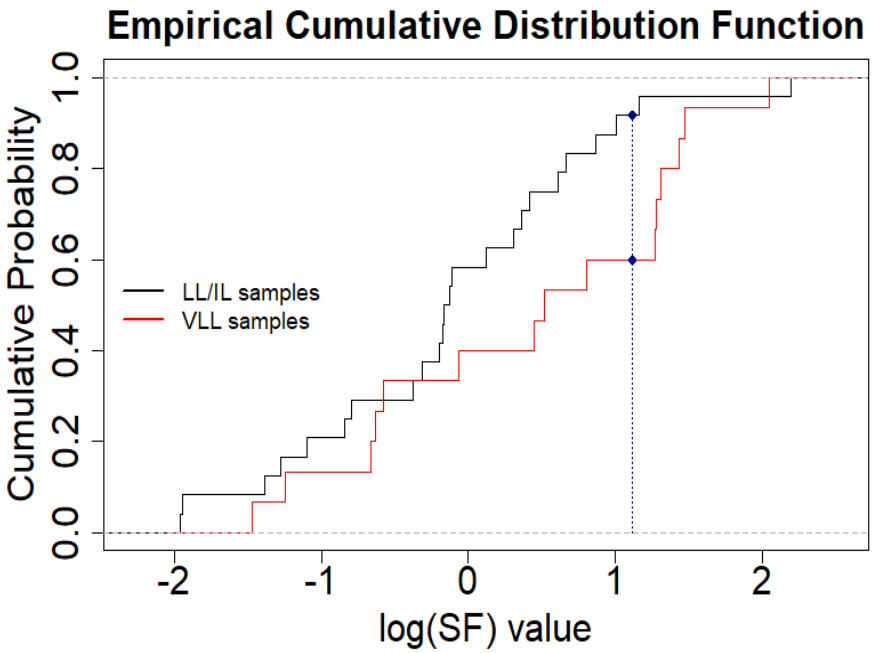

Figure 5.10: The Empirical Cumulative Distribution Function for two distributions for SF of pair Fe-55/Co-60; LL/IL and VLL (for samples with Co-60 specific activity greater than 10 Bq/g) samples respectively. The maximum discrepancy between distributions is D=0.36.

Additionally, the third quartile of SFs for VLL samples with specific activity of Co-60 greater than 10 Bq/g is 3.6. It shows that the SF values are comparable for LL/IL samples (3.6 and 1.6 respectively), which may indicate similar cooling times for both distributions. We observe different SF values for different positions in the accelerator for the same cooling time spans (see Figure 3.5). This behaviour can suggest that the samples for VLL with specific activity of Co-60 greater than 10 Bq/g and LL/IL can represent the activated material occurring close to the concrete tunnel wall, where the production rate of Co-60 is higher than of Fe-55.

In order to examine the distribution of cumulative SF of the Fe-55/Co-60 pair, one performs the W test and complementary graphical methods, such as histogram and Q-Q plots, as presented in Figure 5.11.

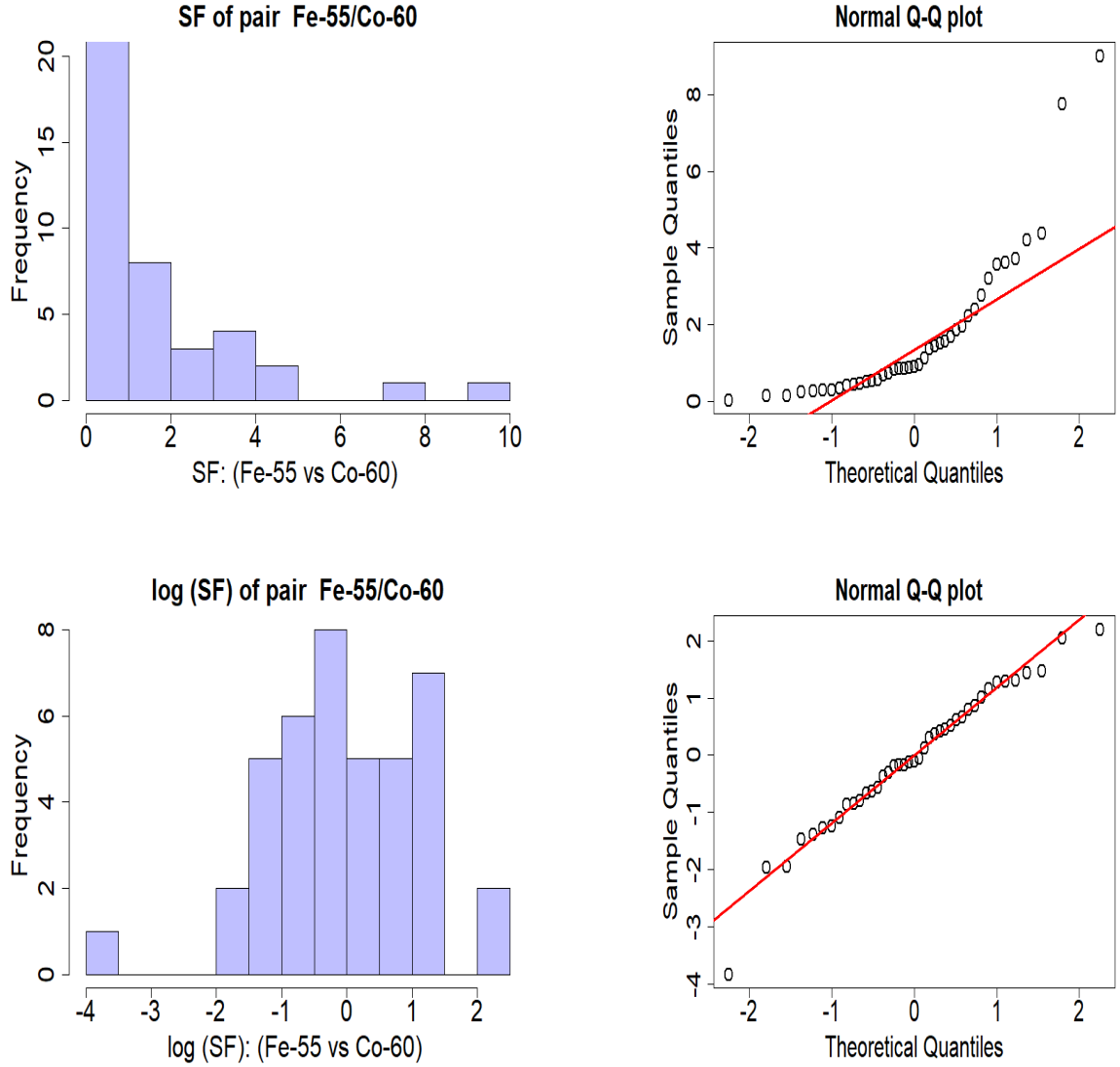

Figure 5.11: Histograms and Q-Q plots of cumulated scaling factors for pair of Fe-55 and Co-60 for 41 samples of activated Steel.

A negative skewness indicates that the size of the left-handed tail is larger than the right-handed tail. After logarithmic transformation, the skewness value indicates that data are moderately skewed. The p-value obtained in the W test, indicates that we cannot reject the null hypothesis (the sample distribution in normal). The summary is given in Table 5.10.

Table 5.10: Summary of the SF analyses of the Fe-55 and Co-60 pair for activated Steel.

SF of pair Fe-55/Co-60, n=41				
Mean	1.7		**Median**	0.9
Standard deviation	2.0		Q_1	0.4
Geometric mean	1.0		Q_3	2.3
Geometric st dev	3.3		**Correlation**	0.98
	non log-transformed data		**log-transformed data**	
Skewness	2.2		-0.6	
W test	**W**	0.74	**W**	0.97
	p-value	4.97E-07	**p-value**	0.38
	reject normality		cannot reject normality	

Conversely, we extracted SF values from VLL sample campaigns based on the specific activity of Co-60 lower than 10 Bq/g. The third quartile for the Fe-55/Co-60 SF is 21. This suggests that those samples have shorter cooling times than LL/IL samples. The tests performed show that the distribution of VLL samples for Co-60 $>$ 10 Bq/g and LL/IL do not originate from the same distribution (the p-value for KS test is 7.3E-14, the maximum discrepancy between distributions is D=0.82). Those samples represent the majority of VLL sample campaigns carried out till 2020 (99 out of 116), which can result that the all VLL and LL/IL samples originate from two different distributions, as depicted in Figure 5.6. The VLL samples with specific activities of Co-60 lower than 10 Bq/g can represent the activated material occurring close to the beam line, where the production rate of Fe-55 is higher than of Co-60, as depicted in Figure 3.5.
Due to the lack of a larger number of LL/IL samples at the time of this study, it was decided to consider the VLL scaling factors for the LL/IL waste for penalization purposes.

5.5 Application of the LL/IL characterization methodology to output waste packages

Based on the recommended radionuclide inventory and its corresponding SF values that are summarized in Table 5.3 and gamma spectrometry analysis (see Section 4.2), we estimate the total beta- gamma specific activity of LL/IL waste packages for the elimination via melting. The application of LL/IL methodology developed at CERN is demonstrated for the following examples, i.e. for a 2.7 m^3 waste package as shown in Figure 5.12.

Figure 5.12: A 2.7 m^3 container filled with 18 ion pumps (During filling up and measuring, respectively).

The waste package is counted by gamma spectrometry from six faces. The geometry models of the package are constructed with 3 dimensional rendering Geometry Composer as shown in Figure 5.13.

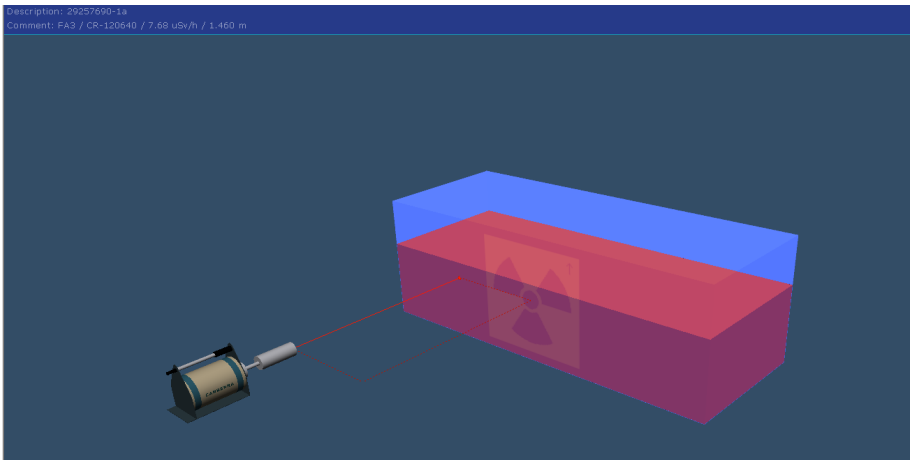

(a) ISOCS geoemtry of face 1A of the 2.7 m^3 waste package. The red colour reperesents the level of the waste inside, the blue colour the container walls.

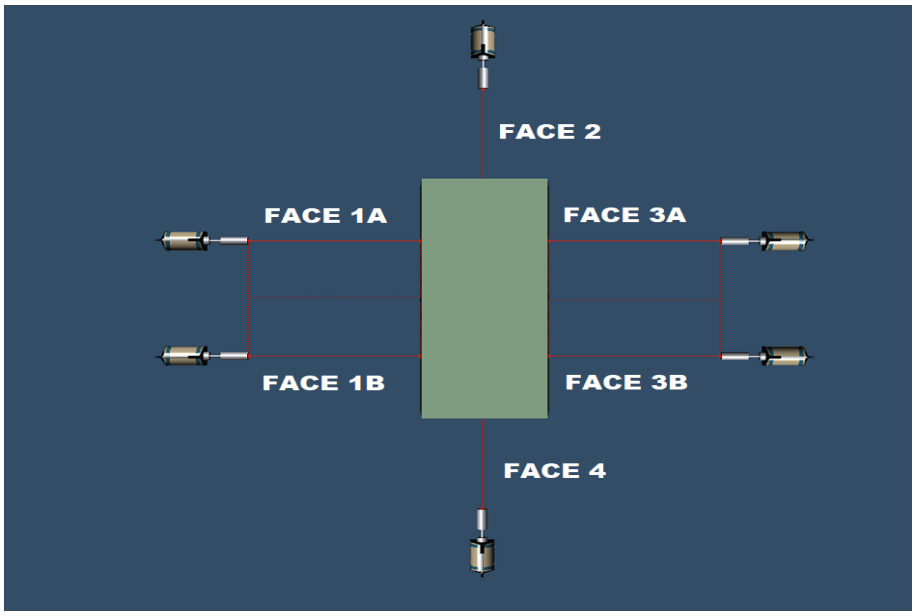

(b) Combination of the geometry models for six faces of the package.

Figure 5.13: ISOCS geometry of the 2.7 m^3 waste package.

In Table 5.11, we present the average total specific activities of gamma and beta emitters with the corresponding uncertainties (absolute values) for the output waste package.

Table 5.11: The average total specific activity estimates for the 2.7 m^3 container with the uncertainty, $A^{TOT}_{\beta,\gamma}$= 5500 (4425) Bq/g. The activity uncertainties of the radionuclides are quoted at 1 σ. Careful interpretation of the uncertainties (such as for V-49) is required as the activities (calculated using the scaling factors) are not normally distributed. The activity values follow a log-normal distribution.

ETM		**DTM**		**ITM**	
Radionuclide	Activity [Bq/g]	Radionuclide	Activity [Bq/g]	Radionuclide	Activity [Bq/g]
Co-60	208 (30)	H-3	1061 (746)	Be-10	2.08E-04 (0.03)
Na-22	0.08 (0.004)	Fe-55	3952 (2371)	Cl-36	0.004 (0.5)
Sc-44<Ti-44	0.29 (0.08)			Ar-39	2.9 (280)
Mn-54	0.25 (0.04)			Ca-41	0.016 (1.5)
				V-49	0.2 (1227)
				Ni-59	3.1 (39.0)
				Ni-63	270 (3437)
				Si-32	0.18 (27.6)

The uncertainties of the DTM and ITM radionuclides consist of the uncertainty of the activity of Co-60 (A^{Co-60}) from the gamma spectrometry analysis and uncertainty related to the SF experimental and analytical values (SF_i). The uncertainty propagation of the product of A^{Co-60} and SF_i are computed by Equation 5.13

$$\sigma(A^{Co-60} \cdot SF_i) = (A^{Co-60} \cdot SF_i)\sqrt{\left(\frac{\sigma(A^{Co-60})}{A^{Co-60}}\right)^2 + \left(\frac{\sigma(SF_i)}{SF_i}\right)^2} \tag{5.13}$$

Additionally, in order to estimate the standard deviation of the DTM radionuclides, one applies the following methods presented in [116], where one estimates the standard deviation from the interquartile range. Equation 5.14 presents the idea of the proposed estimation.

$$\sigma(SF_i) \approx \frac{q3 - q1}{2\Phi^{-1}\left(\frac{0.75n - 0.125}{n + 0.25}\right)}, \tag{5.14}$$

where q1 and q3 are first and third quartiles, n is the number of samples. Φ^{-1} is the upper zth percentile of the standard normal distribution, which can be computed by the command "qnorm(z)" using the statistical software R.

The large uncertainty values of the ITM radionuclides are due to wide log-normal distribution of SF for, e.g. V-49 and Ni-63.

During the gamma spectrometry analysis, we consider both uniform activity distribution and geometry optimization techniques. Hence, we qualify the activity results of the 2.7 m^3 waste package in order to quantify the impact of assuming uniform activity distribution of the gamma emitters within the waste. The qualification process is described in Chapter 4.

For each face, activity values are determined using the Genie 2000 Nuclide Identification with the Interference Correction calculation engine. The multi-count activity ratios of the reference and optimized geometry models for the 2.7 m^3 waste package are presented in Figure 5.14. During the optimization process, the contrast parameter is varied from 1 to 50 depending on the heterogeneity of the assay waste package. The activity ratios given by the gamma spectrometry measurements, with a uniform activity distribution within the material matrix, as presented in Figure 5.14 are between 2 (for Co-60) and 3.5 (for Sc-44<Ti-44).

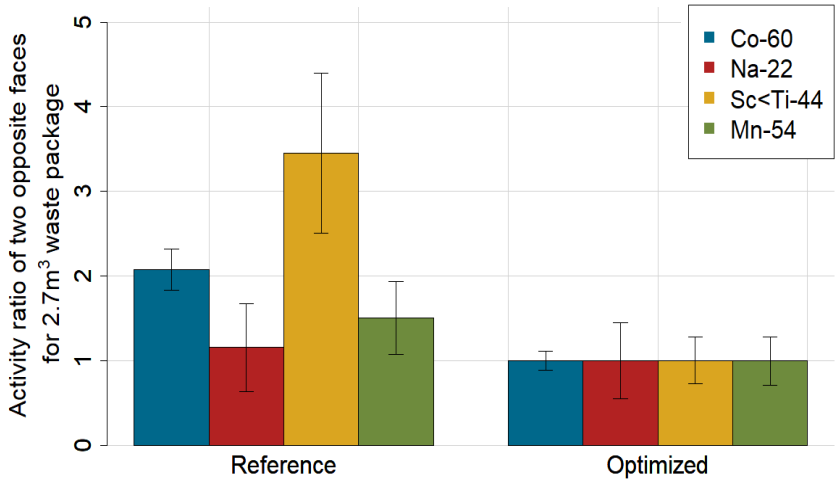

Figure 5.14: Activity ratio for opposite faces before and after geometry optimization for the contrast parameter ranging from 1 to 50 for the 2.7 m^3 waste package.

After geometry optimization, the activity ratios converge to one, which means that the activity values obtained by measuring two opposite faces are consistent. The optimization is performed over two faces at a time, therefore we opt for averaging the results obtained for each pair of faces. The activity uncertainty of the average value is calculated as the square root of the quadratic sum of uncertainties corresponding to each single face. This ignores any correlations between activity values of each face. In Table 5.12, we present the average activity values of the reference and optimized models over two, four and six opposite faces for the waste package.

Table 5.12: Average activities over the two opposite faces with the highest dose rate discrepancies and four and six faces with the reference and optimized models. Uncertainties are given at 1σ. Note that the reference activity result uncertainties do not take into account the geometry model uncertainty due to the less known geometry parameters. N/A corresponds to unidentified radionuclides.

2.7 m^3 WASTE PACKAGE

	REFERENCE			OPTIMIZED			Ratio OPTIMIZED/REFERENCE		
	Two opposite faces	**Four faces**	**Six faces**	**Two opposite faces**	**Four faces**	**Six faces**	**Two opposite faces**	**Four faces**	**Six faces**
Co-60 [Bq/g]	1.76E+02 (4 %)	2.09E+02 (3 %)	1.97E+02 (3 %)	1.79E+02 (4 %)	2.25E+02 (3 %)	2.61E+02 (3 %)	1.02 ±0.06	1.08 ± 0.05	1.33 ±0.05
Na-22 [Bq/g]	7.72E-02 (22 %)	N/A	N/A	8.48E-02 (22 %)	N/A	N/A	1.1 ±0.17	N/A	N/A
Sc-44<Ti-44 [Bq/g]	3.01E-01 (12 %)	2.87E-01 (9 %)	N/A	2.11E-01 (14 %)	2.32E-01 (11 %)	N/A	0.7 ±0.13	0.81 ±0.12	N/A
Mn-54 [Bq/g]	2.86E-01 (14 %)	2.79E-01 (10 %)	N/A	3.46E-01 (14 %)	2.45E-01 (11 %)	N/A	1.21 ±0.24	0.88 ±0.13	N/A

The objective of applying the geometry optimization method is to reduce the over (or under) estimation of the activities by improving the geometry modeling accuracy. The geometry optimization using the GURU tool enables estimating the best known activity values for the 2.7 m^3 waste package. The comparison of the reference and optimized model activity values for the waste package takes into account the average of the activity values for opposite faces with the highest dose rate difference. The highest measured dose rate ratio between two opposite faces is about 6 for this waste package. After the geometry optimization process, the ratio of the optimized and the reference models average activities for opposite faces with the highest dose rate ratio are underestimated by up to 20 % for Mn-54. For both Co-60 gamma lines, the ratio is fairly close to unity, as shown in Table 5.12 .

The averaging over four or six faces for optimized models is based on the assumption that we perform gamma spectrometry measurements of each face using the same detector, and the average value is only an approximation. If we opt for averaging the results for four and six faces, the ratio of activities of optimized and reference models increases. The differences between averaging over four or six faces and two faces of the optimized models are 6 % and 30 % respectively for Co-60.

We notice that the ratio between the average activity values of the optimized and reference models differ by less than 30 % (for Co-60, as the dominant gamma emitter to the total beta-gamma activity), even when the activity distribution is so heterogeneous that GURU predicts a factor 27 of the range of the relative source concentration variations of six faces, where the average number of hot spots per face is 5. This result suggests that the use of a reference model (as compared with an optimized model) is adequate for the purpose of waste characterization with heterogeneously distributed activity for the 2.7 m^3 waste package.

Additionally, we compare the activity concentration of Co-60 obtained from the gamma spectrometry analysis and the methodology that allows for quantifying the specific activities of Co-60 for various unitary waste (Sections 4.1). The average specific activity value of Co-60 for 18 ion pumps measured individually is 256 Bq/g and the predicted value is 280 Bq/g. Therefore, we show that this methodology is operationally efficient for waste package production purposes. Also, the methodology is validated using *In-Toto* gamma spectrometry measurements of the 2.7 m^3 waste package containing the 18 ion pumps, considering both uniform activity distribution and geometry optimization techniques, as described above.

Conclusion

The purpose of this thesis is to propose a technical solution in order to radiologically characterize Low level/Intermediate level (LL/IL) metallic waste produced when operating high-energy particle accelerators. The methodology makes use of analytical calculations and experimental measurements that allow the prediction of the radionuclide inventory and the qualification of the corresponding activity concentrations. Based on this information, we can perform the classification and thereby evaluate the acceptability of a waste population prior to its elimination in the dedicated final disposal facility, or the melting facility as an intermediate waste conditioning step before its final disposal, as required. The LL/IL metallic waste includes the legacy waste temporarily stored at CERN.

The thesis began with an overview of CERN's accelerator complex and the activation mechanisms that might lead to the production of radioactive waste. We also showed the concept of accelerator beam dynamics and eventual beam loses in accelerators. The beam loss monitoring system installed at CERN's accelerators helps identifying the beam loss mechanisms by measuring the corresponding patterns, which can be used in subsequent analytical activation calculations. Furthermore, we described in detail the characterization workflow that is in accordance with the IAEA guidelines. In particular, the radiological characterization phases, including the classification that is based on the activity concentration and half-lives of radionuclides and categorization that describes other waste properties and any processes that change the waste characteristics.

At the beginning of our study, we tackled a difficult task of predicting the radionuclide inventory. In order to obtain such a list, we need to perform a series of activation calculations using the well established analytical software tool ActiWiz. This allows rapid and accurate estimation of radionuclide production rate and the comparison of several hundred different activation scenarios. The calculations were performed for steel waste, which is a major fraction of legacy LL/IL waste temporary stored at CERN. Hence, the radionuclide inventory for steel waste was established by simulating 525 activation scenarios. Each activation scenario was normalized to the maximum acceptable activity for VLL waste, such as IRAS and to the maximum acceptable activity for LL/IL waste. Afterwards, we combined the obtained radionuclide inventories for VLL and LL/IL elimination pathways. The radionuclide inventory assigned to VLL waste was found to represent a subset of the LL/IL inventory. Every radionuclide identified in the gamma spectrometry measurement was found to be part of the radionuclide list obtained analytically.

The validation of the gamma-emitting radionuclides was based on the gamma spectrometry analysis of over 2'000 m^3 metallic waste, being eliminated within the SHERPA project. Additionally, the validation was performed on waste which belongs to the pilot project MAST. The *In-Toto* gamma spectrometry validation confirmed the accuracy of the activation simulations and calculations used to predict the radionuclide inventory of LL/IL waste.

The crucial step in the radiological characterization process is to quantify the activity concentrations of the radionuclides, classified as Easy-to-measure (ETM), Difficult-to-measure (DTM) or Impossible-to-measure (ITM) respectively. The activity concentration values of the ETM radionuclides are evaluated via a NDA technique, based on gamma spectrometry. Radiometric measurements using gamma spectrometry present many challenges. One is the radiological characterization of massive metallic waste items, which typically weigh more than 1 ton in general. The self-absorption and the heterogeneous activity distribution within the waste require a *In-ToTo* gamma spectrometry measurement with multiple counts. Additionally, dose rate levels above 100 μSv/h at contact creates both radiation protection and gamma spectroscopy acquisition constraints. In the acquisition phase of gamma spectrometry, we meet challenges related to the high counting rate effects and corresponding dead times. In the acquisition phase, we proposed a counting geometry that leads to lower dead times, while maintaining the necessary MDA values that are at least 10 % of the VLL declaration thresholds. In the analysis phase of the gamma spectrometry measurement, we encountered difficulties in the accurate determination of the geometry modelling parameters. These parameters are not well known, especially the activity distribution and material chemical composition. Consequently, the uncertainties on the activity of inhomogeneous waste can be high. In this thesis, we investigated the impact of the assumption that the activity is distributed homogeneously within the waste using the concept of geometry optimization methodology given in Chapter 4. The available software from Mirion Technologies (Canberra), such as ISOCS for full peak efficiency calculations and IUE for uncertainty estimation of the full peak efficiencies present limitations. ISOCS allows modelling only one hotspot at a time, in the geometry model. In IUE, we can generate multiple hotspots, however their relative activity concentrations are limited to a single value for all hotspots. In order to overcome those limitations, in the case of a heterogeneous activity distribution within the waste, we developed a novel in-house tool named GURU. This tool enables us to calculate the uncertainties related to activity distribution and reduce them by combining the gamma spectrometry results in order to identify the best geometry models, to describe the "actual" geometry of the waste. This can be achieved by constructing the FOMs that rely on the multi-count and multi-line activity consistencies. Within this Chapter, we determined the impact of the various geometries on the efficiency calibrations and the spread of the efficiency calibration computed for 1000 models for massive iron blocks ($>$ 2 tons) for energies ranging from 45 keV up to 3 MeV for the activity values. Afterwards, we combined the gamma spectrometry results to converge on the "best models", which represent the best knowledge we can have by performing the geometry optimization. After the optimization, the activity values of the opposite faces

were consistent using the optimal models. Based on the optimization results, we calculated the multi-count activity ratios of the reference and optimized geometry models. The results allow showing whether the average activities of uniform distribution geometry under- or overestimate the expected activity values. Application of this novel NDA technique, for massive LL/IL waste with high activity heterogeneity between faces, allowed us to conclude that the ratio between the average activity values of the optimized and reference models could be as high as a factor of 2. The activity ratio of two faces using the reference models does not accurately represent the actual activity contrast of the item, as shown by the geometry optimization results. Nevertheless, using the geometry optimization, one can define the best-known contrast distribution or the contrast values within the waste item. By comparing the reference and optimized models, one shows that performing measurements in the following conditions leads to reasonably conservative results, such as computing the average activity for the most radioactive faces of the waste and considering the reference model. However, we recommend establishing a safety factor represented as an additional systematic uncertainty of 50 % on the average activity values using the reference models. It is the first time at CERN that we have evaluated the uncertainty associated with non-homogeneous activity distribution in a waste package and been able to recommend an accurate safety factor to compensate for it.

In order to quantify the activity levels of DTM radionuclides, one needs to establish the SFs for pair of DTM and KN radionuclides. We need to collect a representative sample set from the waste population. This process might be long and challenging. During the writing of this thesis, the phase of collecting LL/IL samples was still ongoing, and the number of samples analyzed via radiochemical techniques was not yet sufficient to estimate the experimental SFs. Thus, the estimation of DTM activity values is based on the SF values estimated for VLL waste. The validation of these SFs covers over 300 samples that are measured using NDA and DA techniques, i.e. gamma spectrometry and radiochemical analysis. We focused on performing statistical test analyses, in order to investigate the VLL and LL/IL SF distributions and verify their normality. The analyses showed that the distribution of H-3/Co-60 SFs for the VLL and LL/IL may originate from the same distribution, also both follow a log-normal distribution. Subsequently, similar analyses are performed for the distribution of Fe-55/Co-60 SFs. In this case, the distributions are not identical. It might be due to the differences in the production rate of Co-60 and Fe-55 in CERN's accelerator position, as well as the impact of the cooling time on the SF values. The final list of ITM radionuclides was verified by checking whether the corresponding geometric average values (that are normalized to the average specific activity to 1 Bq/g of the KN) was above the declaration threshold of the LL/IL waste, for the maximum specific activity of 37 kBq/g, and Co-60 as the KN. However, one needs to take into account the corrective factor of 2.7 for the analytical SFs for all ITM radionuclides, due to the possible discrepancies between experimental and analytical SFs that were found for DTM radionuclides. Those discrepancies might be caused by the fact that the scenarios considered with ActiWiz have the same probability of occurrence, whereas some samples from radioactive waste follow

similar radiological history. At the same time, we find it remarkable that we could predict by analytical means the scaling factors between radionuclides produced over 30 years of beam operation, with cooling times ranging from 3 to 30 years, in a number of different metallic alloys and in machines with beam energies ranging from 160 MeV up to 7 TeV with an accuracy better than a factor of three.

Within the thesis, we developed a methodology for the radiological characterization of radioactive waste at CERN. The methodology covers a broad range of fields ranging from gamma spectrometry measurements, statistical analysis and sampling, analytical calculations. The methodology is important for defining an elimination path for LL/IL activated waste towards the French repositories. We provided an example of the output waste, which was analyzed following all steps of the developed methodology. We presented the estimated total beta-gamma specific activity of the 2.7 m^3 waste package planned to be eliminated within the scope of the MAST project. The estimated activity of the 2.7 m^3 waste package was 5500 Bq/g. In addition, we qualified the gamma spectrometry results, assuming the homogeneous activity distribution within the package. The calculations showed that the ratio between the average activity values of the optimized and reference models differs maximally by 30 % (for Co-60) for six faces, and less than 10 % if we consider four faces, bearing in mind that GURU predicts a factor 27 (or 26) of the range of the relative activity concentration variations of six (or four) faces. The result implies that the reference model is adequate to use for the purpose of waste characterization with heterogeneously distributed activity for this 2.7 m^3 waste package.

In addition, we proposed a new methodology that predicts the total beta-gamma specific activity based on the average dose rate measurements for LL/IL waste produced at CERN in an operationally efficient manner for waste package production purposes. The methodology was validated using gamma spectroscopy techniques with a geometry model optimization formalism. The expected Co-60 specific activities of the waste could range from 50 to 2000 Bq/g while the maximum contact dose rate ranges from 100 μSv/h to 1 mSv/h. The developed methodology allows for performing a preliminary quantification of the specific activities of Co-60 and other beta-gamma emitters within a waste package using the SF approach. It is based on the measured average dose rate mapping at 40 cm from the individual waste items that will be packaged inside the waste container. This methodology is valid under the assumption that Co-60 is the dominant gamma dose contributor (referred to as KN) in the waste item, where the decay time is more than 3 years. It is based on the experimental correlation between the ratio of the specific activity of Co-60 and the average dose rate as a function of apparent density of the waste item.

Further research is needed to establish LL/IL SF values, based on the sufficient number of samples to be collected and analyzed in the future. Next, we could compare the activity values of the waste package subject to melting, i.e. using the radionuclide inventory with updated SF and one that is established using the methodology presented in this thesis for the sample collected after melting, which is representative of the waste package due to homogenisation property of the melting process.

Finally, the developed methodology in this thesis can be extended in order to radiologically characterize LL/IL unitary items that will be directly eliminated at the French repository without melting. For the analytical calculations for the prediction of the radionuclide inventory one could consider materials other than steel such us copper and concrete. The geometry optimization technique could be of great interest when applied to other shapes and geometries of LL/IL unitary items. Similarly, the new methodology for predicting the total beta-gamma specific activity based on the average dose rate measurement, could also be extended to cover the needs of the LL/IL unitary waste.

Appendix A

Geometry optimization process

A.1 Impact of the envelope geometry

Table A.1: Computed efficiency curves for the long iron block originating from stochastically perturbed models for maximum and minimum geometry dimensions.

Energy (keV)	Maximum geometry	Minimum geometry	Maximum/minimum geometry
45	3.44E-08	3.51E-08	0.98
50	4.95E-08	5.05E-08	0.98
60	8.95E-08	9.12E-08	0.98
70	1.39E-07	1.42E-07	0.98
80	1.97E-07	2.01E-07	0.98
90	2.57E-07	2.62E-07	0.98
100	3.18E-07	3.24E-07	0.98
110	3.77E-07	3.84E-07	0.98
120	4.30E-07	4.38E-07	0.98
150	5.40E-07	5.49E-07	0.98
200	5.83E-07	5.93E-07	0.98

Continued on next page

Table A.1 – *Continued from previous page*

Energy (keV)	Maximum geometry	Minimum geometry	Maximum/minimum geometry
300	5.05E-07	5.13E-07	0.98
400	4.25E-07	4.32E-07	0.99
600	3.39E-07	3.44E-07	0.98
800	2.92E-07	2.96E-07	0.99
1000	2.64E-07	2.68E-07	0.99
1173	2.47E-07	2.50E-07	0.99
1332	2.34E-07	2.38E-07	0.99
1500	2.21E-07	2.24E-07	0.99
2000	1.93E-07	1.96E-07	0.99
2500	1.70E-07	1.72E-07	0.99
3000	1.49E-07	1.51E-07	0.99

4

Table A.2: Computed efficiency curves for the short iron block originating from stochastically perturbed models for maximum and minimum geometry dimensions.

Energy (keV)	Maximum geometry	Minimum geometry	Maximum/minimum geometry
45	8.84E-09	9.47E-09	0.93
50	1.27E-08	1.36E-08	0.93
60	2.30E-08	2.45E-08	0.94
70	3.57E-08	3.80E-08	0.94
80	5.06E-08	5.38E-08	0.94
90	6.63E-08	7.05E-08	0.94

Continued on next page

Table A.2 – *Continued from previous page*

Energy (keV)	Maximum geometry	Minimum geometry	Maximum/minimum geometry
100	8.23E-08	8.76E-08	0.94
110	9.76E-08	1.04E-07	0.94
120	1.11E-07	1.19E-07	0.94
150	1.39E-07	1.48E-07	0.94
200	1.50E-07	1.60E-07	0.94
300	1.29E-07	1.38E-07	0.94
400	1.09E-07	1.16E-07	0.94
600	8.67E-08	9.24E-08	0.94
800	7.46E-08	7.96E-08	0.94
1000	6.71E-08	7.16E-08	0.94
1173	6.27E-08	6.69E-08	0.94
1332	5.93E-08	6.33E-08	0.94
1500	5.64E-08	6.02E-08	0.94
2000	4.94E-08	5.28E-08	0.94
2500	4.35E-08	4.64E-08	0.94
3000	3.82E-08	4.08E-08	0.94

A.2 Activity values for different models

Figure A.1 shows the activity values for optimized perturbed models generated in GURU for opposite faces 1 and 3 or 2 and 4 for Sc-44<Ti-44. The contrast for both pair of faces ranges of [1-10] and [1-200].

The area (purple colour) where the histograms of faces 1 and 3 or 2 and 4 overlap each other represents the "best" optimized models according to the best knowledge we have of the waste item.

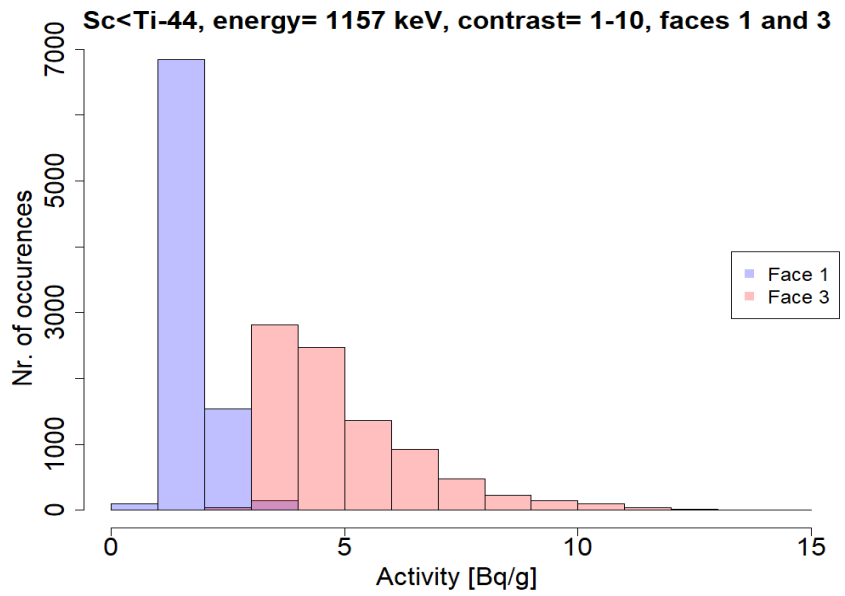

(a) Activities calculated for Sc-44<Ti-44, the relative source concentration ranges from 1 to 10, and two opposite faces measured. The purple colour represents the overlapping activities for faces 1 and 3. For activity values between 2 and 4 Bq/g, the activity ratio for opposite faces is 1, for some calculated models.

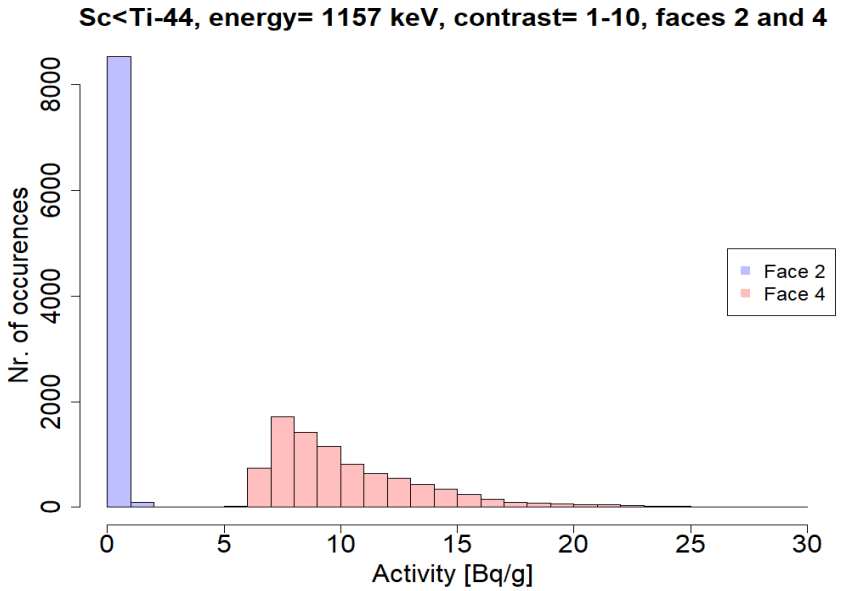

(b) For the activity contrast ranging from 1 to 10 for Sc-44<Ti-44, activities of faces 2 and 4 do not intersect.

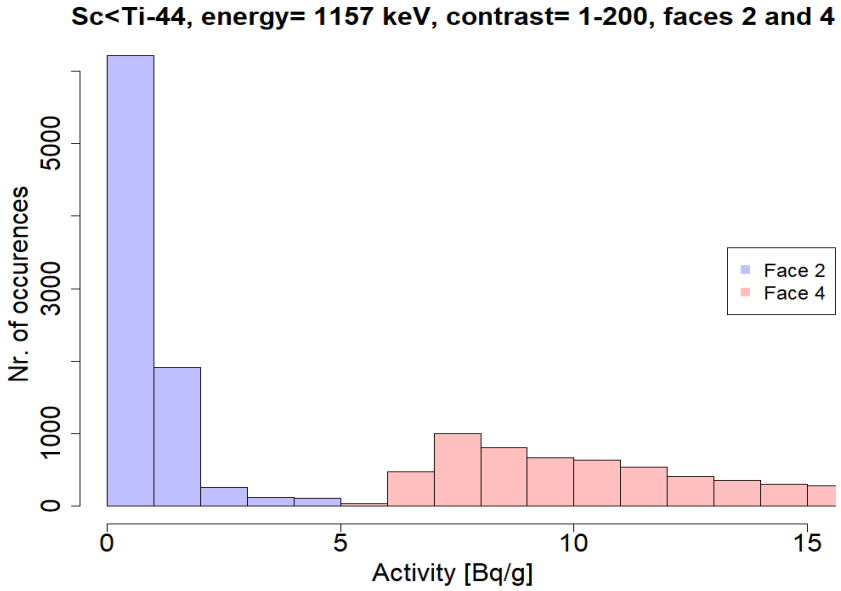

(c) For the activity ranging around 5 Bq/g with uncertainties given at 1σ, we might observe the activity ratio of faces 2 and 4 close to 1 for Sc-44<Ti-44 with the contrast [1-200].

Figure A.1: Activity ratios for two opposite faces.

Bibliography

[1] Actiwiz. http://actiwiz.web.cern.ch/. Last accessed on 2020-01-15.

[2] Spectrum Analysis. URL https://www.canberra.com/literature/fundamental-principles/pdf/Spectrum-Analysis.pdf. Last accessed on 2021-01-27.

[3] CERN HL-LHC. https://home.cern/topics/high-luminosity-lhc. Last accessed on 2020-01-07.

[4] *A Basic Toxicity Classification of Radionuclides*. Number 15 in Technical Reports Series. INTERNATIONAL ATOMIC ENERGY AGENCY, Vienna. ISBN 92-0-125063-0. URL https://www.iaea.org/publications/1110/a-basic-toxicity-classification-of-radionuclides.

[5] ISOLDE. http://isolde.web.cern.ch/. Last accessed on 2020-01-07.

[6] Technical Advantages of ISOCS/LabSOCS. URL https://mirion.s3.amazonaws.com/cms4_mirion/files/pdf/application-notes/c39530_isocs_labsocs_app_note_3.pdf?1557944467. Last accessed on 2021-01-12.

[7] CERN Brochure. https://cds.cern.ch/record/2255762/files/CERN-Brochure-2017-. Last accessed on 2020-01-07.

[8] *Particle counting in radioactivity measurement*. ICRU Report. ICRU, Bethesda, MD, 1994. URL https://cds.cern.ch/record/1163700.

[9] *The coefficient of determination in multiple regression*, pages 91–95. Springer US, Boston, MA, 1997. ISBN 978-0-585-25657-3. doi: 10.1007/978-0-585-25657-3_19. URL https://doi.org/10.1007/978-0-585-25657-3_19.

[10] *Radiological Characterization of Shut Down Nuclear Reactors for Decommissioning Purposes*. Number 389 in Technical Reports Series. INTERNATIONAL ATOMIC ENERGY AGENCY, Vienna, 1998. ISBN 92-0-103198-X. URL https://www.iaea.org/publications/5723/radiological-characterization-of-shut-down-nuclear-reactors-for-decommissioning-purposes.

[11] *Predisposal Management of Radioactive Waste, Including Decommissioning*. Number WS-R-2 in Safety Standards Series. INTERNATIONAL ATOMIC ENERGY AGENCY, Vienna, 2000. ISBN 92-0-100300-5. URL https://www.iaea.org/publications/5919/predisposal-management-of-radioactive-waste-including-decommissioning.

[12] *Management of Low and Intermediate Level Radioactive Wastes with Regard to their Chemical Toxicity*. Number 1325 in TECDOC Series. INTERNATIONAL ATOMIC ENERGY AGENCY, Vienna, 2003. ISBN 92-0-119802-7. URL https://www.iaea.org/publications/6469/management-of-low-and-intermediate-level-radioactive-wastes-with-regard-to-their-chemical-toxicity.

[13] *Application of the Concepts of Exclusion, Exemption and Clearance*. Number RS-G-1.7 in General Safety Guides. INTERNATIONAL ATOMIC ENERGY AGENCY, Vienna, 2004. ISBN 92-0-109404-3. URL https://www.iaea.org/publications/7118/application-of-the-concepts-of-exclusion-exemption-and-clearance.

[14] *Strategy and Methodology for Radioactive Waste Characterization*. Number 1537 in TECDOC Series. INTERNATIONAL ATOMIC ENERGY AGENCY, Vienna, 2007. ISBN 92-0-100207-6. URL https://www.iaea.org/publications/7655/strategy-and-methodology-for-radioactive-waste-characterization.

[15] *Categorizing Operational Radioactive Wastes*. Number 1538 in TECDOC Series. INTERNATIONAL ATOMIC ENERGY AGENCY, Vienna, 2007. ISBN 92-0-102807-5. URL https://www.iaea.org/publications/7679/categorizing-operational-radioactive-wastes.

[16] Ordonnance sur la radioprotection (ORaP) du 26 avril 2017 (Etat le 1er janvier 2021). 814.501, 2007.

[17] *Classification of Radioactive Waste*. Number GSG-1 in General Safety Guides. INTERNATIONAL ATOMIC ENERGY AGENCY, Vienna, 2009. ISBN 978-92-0-109209-0. URL https://www.iaea.org/publications/8154/classification-of-radioactive-waste.

[18] *Use of Scaling Factors for Waste Characterization in Nuclear Power Plants*. Number NW-T-1.18 in Nuclear Energy Series. INTERNATIONAL ATOMIC ENERGY AGENCY, Vienna, 2009. ISBN 978-92-0-110808-1. URL https://www.iaea

.org/publications/7985/determination-and-use-of-scaling-factors-for-waste-characterization-in-nuclear-power-plants.

[19] Mesurage de libération de matériaux et de secteurs de zone contrôlées.Directive IFSN-B04/f en collaboration avec l'Office fédéral se la santé publique (OFSP) et de la Caisse nationale suisse d'assurance en cas d'accidents (Suva), 2009.

[20] *Advanced ISOCS Uncertainty Estimator (A-IUE)* , 2009.

[21] *Accord entre le Conseil Fédéral Suisse, le Gouvernement de la République Française, et l'Organisation Européenne pour la Recherche Nucléaire relatif à la Protection contre les rayonnements ionisants et à la Sûreté des Installations de l'Organisation Européenne pour la Recherche Nucléaire, conclu le 15 novembre 2010, entré en vigueur par échange de notes le 16 septembre 2011.* Number RS 0.814.592.2, Recueil Officiel n. 34 du 23 août 2011, page 3825. Décret n. 2011-1024 du 24 août 2011, JORF n. 0199 du 28 août 2011 page 14594. 2011.

[22] ANDRA. Specification d 'acceptance des colis de dechets radioactifs au CSFMA. INB N 149.ACO.SP.ASRE.99.0002.D. Technical report, 2013.

[23] ANDRA. Critères radiologiques d'acceptation des déchets TFA. SUR.SP.AMES.02.0007. Technical report, 2013.

[24] *CANBERRA. Genie 2000. Spectroscopy Software. Customization tools manual, v.3.4.* 2013.

[25] ASTM A276 / A276M-17, Standard Specification for Stainless Steel Bars and Shapes . Standard, International Organization for Standardization, West Conshohocken, PA, 2017.

[26] *Selection of Technical Solutions for the Management of Radioactive Waste*. Number 1817 in TECDOC Series. INTERNATIONAL ATOMIC ENERGY AGENCY, Vienna, 2017. ISBN 978-92-0-104717-5. URL https://www.iaea.org/publications/12217/selection-of-technical-solutions-for-the-management-of-radioactive-waste.

[27] Lynx® Digital Signal Analyzer, 2018. https://mirion.s3.amazonaws.com/cms4_mirion/files/pdf/application-notes/c36663_lynx_application_note_mirion_2.pdf?1557944574. Last accessed on 2021-02-24.

[28] *IAEA Safety Glossary: 2018 Edition*. Non-serial Publications. INTERNATIONAL ATOMIC ENERGY AGENCY, Vienna, 2019. ISBN 978-92-0-104718-2. URL https://www.iaea.org/publications/11098/iaea-safety-glossary-2018-edition.

[29] Activation and Decay of Radioactive Nuclides, 2020. URL https://tu-dresden.de/ing/maschinenwesen/iet/wket/ressourcen/dateien/akr2/Lehrmaterialien/buz_e.pdf?lang=en. Last accessed on 2020-01-21.

[30] CERN accelerators, 2020. https://home.cern/science/accelerators. Last accessed on 2020-01-07.

[31] Portable HPGe-Based Radionuclide Identifier, 2020. https://mirion.s3.amazonaws.com/cms4_mirion/files/pdf/spec-sheets/falcon-portable-hpge-based-identifier.pdf?1557257239. Last accessed on 2021-02-10.

[32] Germanium detector types, 2020. https://www.mirion.com/learning-center/radiation-detector-types/germanium-detector-types. Last accessed on 2021-02-11.

[33] Analytical Report for CERN. Radiometric and Radiochemical Analysis of Metallic and Liquid Hydrocarbon Sample . Technical Report EDMS 2471524, CERN, 2021.

[34] Y. Algoet, L. Bruno, M. Magistris, R. Michaud, B. Zaffora, and F. P. La Torre. SHERPA (SHEaR Process Assessment). Technical Report EDMS 1428178, CERN, 2015.

[35] M. Barbier. *Induced radioactivity*. North-Holland Pub. Co., 1969.

[36] H Bateman. Solution of a system of differential equationsoccurring in the theory of radioactive transformations. Proc. Cam-bridge Philos. Soc. 15, 1910.

[37] G. Battistoni, F. Cerutti, A. Fasso, A. Ferrari, J. Ranft S. Muraro, S. Roesler, and P.R.Sala. *The FLUKA code: Description and benchmarking. In Hadronic Shower Simulation Workshop*. Fermilab 6-8 September 2006, M. Albrow, R. Raja eds., AIP Conference Proceeding 896, 31-49, 2006.

[38] Giuseppe Battistoni et al. The Application of the Monte Carlo Code FLUKA in Radiation Protection Studies for the Large Hadron Collider. *Prog. Nucl. Sci. Tech.*, 2:358–364, 2011. doi: 10.15669/pnst.2.358.

[39] Giuseppe Battistoni et al. Overview of the FLUKA code. *Annals Nucl. Energy*, 82: 10–18, 2015. doi: 10.1016/j.anucene.2014.11.007.

[40] Hans Bichsel and Heinrich Schindler. *The Interaction of Radiation with Matter*, pages 5–44. Springer International Publishing, Cham, 2020. ISBN 978-3-030-35318-6. doi: 10.1007/978-3-030-35318-6_2. URL https://doi.org/10.1007/978-3-030-35318-6_2.

[41] T. T. Böhlen, F. Cerutti, M. P. W. Chin, A. Fassò, A. Ferrari, P. G. Ortega, A. Mairani, P. R. Sala, G. Smirnov, and V. Vlachoudis. The FLUKA Code: Developments and Challenges for High Energy and Medical Applications. *Nucl. Data Sheets*, 120:211–214, 2014. doi: 10.1016/j.nds.2014.07.049.

[42] H. Borras and M. Widorski. Test of Thermo Scientific RadEye radiation detectorsin a magnetic field. Technical Report EDMS 1586505, CERN, 2016.

[43] A. Bosko, N. Menaa, T. Spillane, F. Bronson, R. Venkataraman, W.R. Russ, W. Mueller, and V. Nizhnik. Efficiency optimization employing random and smart search using multiple counts and line activity consistency benchmarks. Proceedings of WM2011 Conference, February 27-March 3 , 2011, 2011.

[44] R. Brennetot, M. Giuliani, S. Guégan, P. Fichet, L. Chiri, P. Deloffre, A. Masset, C. Mougel, and F. Bachelet. H-3 measurement in radioactive wastes: Efficiency of the pyrolysis method to extract tritium from aqueous effluent, oil, and concrete. *Fusion Science and Technology*, 71(3):397–402, 2017. doi: 10.1080/15361055.2017.1291242. URL `https://doi.org/10.1080/15361055.2017.1291242`.

[45] F. Bronson. ISOCS, a Laboratory Quality Ge Gamma Spectroscopy system you can take to the Source for Immediate High Quality Results. Proceedings of the Rapid Radioactivity Measurements in Emergency and Routine Situations Conference, UK, October 1997.

[46] F. Bronson. Uncertainty of gamma-ray spectrometry measurement of environmental samples due to uncertainties in matrix composition, density and sample geometry. *Applied Radiation and Isotopes*, 276:589–594, 2008. ISSN 0969-8043. doi: https://doi.org/10.1007/s10967-008-0604-z. URL `https://link.springer.com/article/10.1007%2Fs10967-008-0604-z#article-info`.

[47] M. Brugger, A. Ferrari, M. Magistris, S. Roesler, J. Vollaire Cern, Geneva, and Switzerland. Calculation of radioactive isotope production cross-sections with FLUKA and their application to radiological studies. In *Proceedings, 8th Meeting on Shielding Aspects of Accelerators, Targets and Irradiation Facilities (SATIF-8): Pohang, Korea, May 22-24, 2006*, pages 125–144, 2006.

[48] L. Bruno. MAST - Technical specification. Technical Report EDMS 2114037 v.1.0, CERN, 2020.

[49] L. Bruno, C. Delamare, M. Magistris, L. Ulrici, and J.Mueth. FMA Waste Program . Technical Report EDMS 1907015, CERN, 2018.

[50] A. Capella, U. Sukhatme, C-I Tan, and J. Tran Thanh Van. Dual parton model. *Phys. Rept.*, 236:225–329, 1994. doi: 10.1016/0370-1573(94)90064-7.

[51] Jerzy Cetnar. General solution of bateman equations for nuclear transmutations. *Annals of Nuclear Energy*, 33(7):640–645, 2006. ISSN 0306-4549. doi: https://doi.org/10.1016/j.anucene.2006.02.004. URL https://www.sciencedirect.com/science/article/pii/S0306454906000284.

[52] Christopher Clapham and James (James R.) Nicholson. *The concise Oxford dictionary of mathematics*. Oxford paperback reference. Oxford University Press, Oxford, 4th ed. / Christopher Clapham and James Nicholson. edition, 2009. ISBN 0-19-923594-5.

[53] L A Currie. LIMITS FOR QUALITATIVE DETECTION AND QUANTITATIVE DETERMINATION. APPLICATION TO RADIOCHEMISTRY. *Anal. Chem., 40: 586-93 (Mar. 1968).* doi: 10.1021/ac60259a007. URL https://www.osti.gov/biblio/4553230.

[54] J. Durbin. *Distribution Theory for Tests Based on the Sample Distribution Function*. Society for Industrial and Applied Mathematics, 1973. doi: 10.1137/1.9781611970586. URL https://epubs.siam.org/doi/abs/10.1137/1.9781611970586.

[55] Patrycja Dyrcz, Thomas Frosio, Nabil Menaa, Matteo Magistris, and Chris Theis. Qualification of the activities measured by gamma spectrometry on unitary items of intermediate-level radioactive waste from particle accelerators. *Appl. Radiat. Isot.*, 167: 109431, 2021. doi: 10.1016/j.apradiso.2020.109431.

[56] A. Fasso and S. Rokni. Operational radiation protection in high-energy physics accelerators: Implementation of ALARA in design and operation of accelerators. *Radiat. Prot. Dosim.*, 137:94–99, 2009. doi: 10.1093/rpd/ncp189.

[57] A. Fasso et al. The FLUKA code: Present applications and future developments. *eConf*, C0303241:MOMT004, 2003.

[58] A. Ferrari and R.P. Sala, editors. *Physics of showers induced by accelerator beams. Proc. 1995 "Frédéric Joliot" Summer School in Reactor Physics, Cadarache, France, August 22-30, 1995. Ed. CEA, Vol. 1, lecture 5b (1996)*, 1995.

[59] Alfredo Ferrari, Paola R. Sala, Alberto Fasso, and Johannes Ranft. FLUKA: A multi-particle transport code (Program version 2005). 10 2005. doi: 10.2172/877507.

[60] Doris Forkel-Wirth, Stefan Roesler, Marco Silari, Marilena Streit-Bianchi, Christian Theis, Heinz Vincke, and Helmut Vincke. Radiation protection at CERN. In *CERN Accelerator School on High Power Hadron Machines*, 3 2013. doi: 10.5170/CERN-2013-001.415.

[61] R. Froeschl, C. Theis, F. La Torre, H. Vincke, N. Walter, and S. Sgobba. Radiological Hazard classification of material in CERN's accelerators . Technical Report EDMS 1184236, CERN, 2012.

[62] R. Froeschl, M. Magistris, F. Leite Pereira, and C. Theis. Computation of radioactivity in particle accelerators and propagation of uncertainties with the JEREMY code . Technical Report EDMS 1406467, CERN, 2014.

[63] Thomas Frosio, Nabil Menaa, Philippe Bertreix, Maeva Rimlinger, and Chris Theis. A novel technique for the optimization and reduction of gamma spectroscopy geometry uncertainties. *Applied Radiation and Isotopes*, 156:108953, 2020. ISSN 0969-8043. doi: https://doi.org/10.1016/j.apradiso.2019.108953. URL https://www.sciencedirect.com/science/article/pii/S0969804319306852.

[64] Thomas Frosio, Nabil Menaa, Charlotte Duchemin, Nicolas Riggaz, and Chris Theis. A new gamma spectroscopy methodology based on probabilistic uncertainty estimation and conservative approach. *Applied Radiation and Isotopes*, 155:108929, 2020. ISSN 0969-8043. doi: https://doi.org/10.1016/j.apradiso.2019.108929. URL https://www.sciencedirect.com/science/article/pii/S0969804319308759.

[65] Asghar Ghasemi and Saleh Zahediasl. Normality tests for statistical analysis: A guide for non-statisticians. *International journal of endocrinology and metabolism*, 10:486–489, 12 2012. doi: 10.5812/ijem.3505.

[66] Simone Gilardoni et al. Long-term Beam Losses in the CERN Injector Chain, 2015. URL http://jacow.org/HB2014/papers/tho1lr01.pdf. Last accessed on 2020-01-07.

[67] G. Gilmore. *Practical gamma-ray spectrometry*. John Wiley and Sons, 2008.

[68] Ayman Ibrahim Hawari. *High accuracy determination of relative full energy peak efficiencies for high resolution gamma-ray spectrometry*. PhD thesis, 1995.

[69] B. Holzer. Introduction to transverse beam dynamics. CERN, 2013. Last accessed on 2020-01-07.

[70] Xiaolin Hou and Xiongxin Dai. Chapter 2 - environmental liquid scintillation analysis11previous authors are laina salonen (retired) radiation and nuclear safety authority, fin-00,881 helsinki, finland; lauri kaihola (retired), perkinelmer, inc., fin-20,101 turku, finland; brian carter, ontario power generation inc., whitby, ontario l1n 1e4, canada; gordon t. cook, suerc radiocarbon dating laboratory, east kilbride g75 0qf, scotland, and charles j. passo, jr., perkinelmer, inc.,downers grove, illinois 60,515, usa. In Michael F. L'Annunziata, editor, *Handbook of Radioactivity Analysis: Volume 2 (Fourth Edition)*,

pages 41 – 136. Academic Press, fourth edition edition, 2020. ISBN 978-0-12-814395-7. doi: https://doi.org/10.1016/B978-0-12-814395-7.00002-7. URL http://www.sciencedirect.com/science/article/pii/B9780128143957000027. Last accessed on 2020-09-24.

[71] ISO 14850:20074(E). Nuclear energy- waste-packages activity measurement- part 1: High-resolution gamma spectrometry in integral mode with open geometry. Standard, International Organization for Standardization, Geneva, CH, May 2004.

[72] ISO 16966:2013(E). Nuclear energy- nuclear fuel technology- theoretical activation calculation method to evaluate the radioactivity of activated waste generated at nuclear reactors. Standard, International Organization for Standardization, Geneva, CH, December 2013.

[73] ISO 21238:2007(E). Nuclear energy- nuclear fuel technology- scaling factor method to determine the radioactivity of low- and intermediate-level radioactive waste packages generated at nuclear power plants. Standard, International Organization for Standardization, Geneva, CH, April 2007.

[74] ISO/IEC 17025:2017 (E). General requirements for the competence of testing and calibration laboratories. Standard, International Organization for Standardization, Geneva, CH, November 2017.

[75] JCGM100:2008. Evaluation of measurement data- Guide to the expression of uncertainty in measurement . Technical report, BIPM Joint Committee for Guides in Metrology, Paris, September 2008.

[76] JCGM101:2008. Supplement 1 of the Evaluation of measurement data – Guide to the expression of uncertainty in measurement . Technical report, BIPM Joint Committee for Guides in Metrology, Paris, September 2008.

[77] S. Jensen. SPS. 2019. URL https://wikis.cern.ch/display/BEBI/BLM+for+SPS. Last accessed on 2020-01-07.

[78] D. N. Joanes and C. A. Gill. Comparing measures of sample skewness and kurtosis. *Journal of the Royal Statistical Society. Series D (The Statistician)*, 47(1):183–189, 1998. ISSN 00390526, 14679884. URL http://www.jstor.org/stable/2988433.

[79] V. Kain. Beam dynamics and beam losses-circular machines. *CERN Yellow Reports*, 2 (0):21, 2016. URL https://e-publishing.cern.ch/index.php/CYR/article/view/228. Last accessed on 2020-01-07.

[80] S. Kaminski, A. Jakobi, and Chr. Wilhelm. Uncertainty of gamma-ray spectrometry measurement of environmental samples due to uncertainties in matrix composition, density and sample geometry. *Applied Radiation and Isotopes*, 94:306–313, 2014. ISSN 0969-8043. doi: https://doi.org/10.1016/j.apradiso.2014.08.008. URL https://www.sciencedirect.com/science/article/pii/S0969804314003091.

[81] J. M. Kirkpatrick, R. Venkataraman, and B. M. Young. Minimum detectable activity, systematic uncertainties, and the iso 11929 standard. *Journal of Radioanalytical and Nuclear Chemistry*, 296(2):1005–1010, 2013. doi: 10.1007/s10967-012-2083-5.

[82] G.F. Knoll. *Radiation detection and measurements*. John Wiley and Sons, 2010.

[83] M. Krammer. Calorimeters. 2019. URL https://www.hephy.at/fileadmin/user_upload/VO-6-Calorimeters.pdf. Last accessed on 2020-01-15.

[84] M Lamont. Estimates of Annual Proton Doses in the LHC. Technical Report LHC-Project-Note-375. CERN-LHC-Project-Note-375, CERN, Geneva, Jun 2005. URL https://cds.cern.ch/record/893060. Last accessed on 2020-01-07.

[85] Anton Lechner. Particle interactions with matter. *CERN Yellow Rep. School Proc.*, 5:47. 22 p, 2018. doi: 10.23730/CYRSP-2018-005.47. URL https://cds.cern.ch/record/2674116.

[86] Michele Livan and Richard Wigmans. *Interactions of Particles with Matter*, pages 31–51. Springer International Publishing, Cham, 2019. ISBN 978-3-030-23653-3. doi: 10.1007/978-3-030-23653-3_2. URL https://doi.org/10.1007/978-3-030-23653-3_2.

[87] M. Magistris. *Radiological characterization of radioactive waste at CERN*. PhD thesis, 2008.

[88] M. Magistris. Stored and estimated future radioactive waste at CERN (until 2100) INPUT to AGNEB. Technical Report EDMS 1811619, CERN, 2017.

[89] M. Magistris and B. Zaffora. Parameters of radiological interest for the computation of fair-share factors. Technical Report EDMS 1749065, CERN, 2017.

[90] M. Magistris and B. Zaffora. Radionuclide inventory and scaling factors of metallic, TFA radioactive waste. Technical Report EDMS 1501107, CERN, 2020.

[91] Hosam M. Mahmoud. *Shell Sort*, chapter 3, pages 103–128. John Wiley & Sons, Ltd, 2000. ISBN 9781118032886. doi: https://doi.org/10.1002/9781118032886.ch3. URL https://onlinelibrary.wiley.com/doi/abs/10.1002/9781118032886.ch3.

[92] Luca Martino, David Luengo, and Joaquín Míguez. *Introduction*. Springer International Publishing, Cham, 2018. ISBN 978-3-319-72634-2. doi: 10.1007/978-3-319-72634-2_1. URL https://doi.org/10.1007/978-3-319-72634-2_1.

[93] N. Menaa. Specification and Performance Data for Falcon 2 detector . Technical Report EDMS 2398405, CERN, 2020.

[94] N. Menaa. RP Radioanalytical facilities Upgrade - Gamma Spectroscopy . Technical Report EDMS 2454530, CERN, 2020.

[95] N. Menaa, A. Bosko, F. Bronson, R. Venkataraman, W. R. Russ, W. Mueller, V. Nizhnik, and L. Mirolo. Mathematical efficiency calibration with uncertain source geometries using smart optimization. In *2011 2nd International Conference on Advancements in Nuclear Instrumentation, Measurement Methods and their Applications*, pages 1–7, 2011. doi: 10.1109/ANIMMA.2011.6172913.

[96] N. Menaa, P. D'Agostino, B. Zakrzewski, and V.T. Jordanov. Evaluation of real-time digital pulse shapers with various HPGe and silicon radiation detectors. *Nuclear Instruments and Methods in Physics Research Section A: Accelerators, Spectrometers, Detectors and Associated Equipment*, 652(1):512–515, 2011. ISSN 0168-9002. doi: https://doi.org/10.1016/j.nima.2010.08.095. URL https://www.sciencedirect.com/science/article/pii/S0168900210018826. Symposium on Radiation Measurements and Applications (SORMA) XII 2010.

[97] Esma Mobs. The CERN accelerator complex. Complexe des accélérateurs du CERN. Jul 2016. URL https://cds.cern.ch/record/2197559. General Photo. Last accessed on 2020-01-07.

[98] Hun Myoung Park. Univariate Analysis and Normality Test Using SAS, Stata, and SPS. Working paper, The University Information Technology Services (UITS) Center for Statistical and Mathematical Computing, Indiana University, 2008. URL http://www.indiana.edu/~statmath/stat/all/normality/index.html. Last accessed on 2021-06-24.

[99] F. Pereira, C. Theis, and H. Vincke. Development of an inter-process communication framework for Python based web applications - the ActiWiz core as a proof-of-concept . Technical Report EDMS 1343712, CERN, 2014.

[100] Donald Hill Perkins. *Introduction to high energy physics; 4th ed.* Cambridge Univ. Press, Cambridge, 2000.

[101] M.A. Plum. Beam loss mechanisms in high intensity linacs. In *In HB2012: Proceedings of the 52nd ICFA Advanced Beam Dynamics Workshop on High-Intensity and High-Brightness Hadron Beams.*, 2012.

[102] Ervin B. Podgoršak. *Interactions of Charged Particles with Matter*, pages 227–275. Springer Berlin Heidelberg, Berlin, Heidelberg, 2010. ISBN 978-3-642-00875-7. doi: 10.1007/978-3-642-00875-7_6. URL https://doi.org/10.1007/978-3-642-00875-7_6.

[103] Ervin B. Podgoršak. *Interactions of Photons with Matter*, pages 277–375. Springer Berlin Heidelberg, Berlin, Heidelberg, 2010. ISBN 978-3-642-00875-7. doi: 10.1007/978-3-642-00875-7_7. URL https://doi.org/10.1007/978-3-642-00875-7_7.

[104] John W. Pratt and Jean D. Gibbons. *Kolmogorov-Smirnov Two-Sample Tests*, pages 318–344. Springer New York, New York, NY, 1981. ISBN 978-1-4612-5931-2. doi: 10.1007/978-1-4612-5931-2_7. URL https://doi.org/10.1007/978-1-4612-5931-2_7.

[105] Stefan Roesler, Ralph Engel, and Johannes Ranft. The Monte Carlo event generator DPMJET-III. In *International Conference on Advanced Monte Carlo for Radiation Physics, Particle Transport Simulation and Applications (MC 2000)*, 12 2000. doi: 10.1007/978-3-642-18211-2_166.

[106] P. Royston. Approximating the shapiro-wilk w-test for non-normality. *Statistics and Computing*, 2:117–119, 1992.

[107] S. S. Shapiro and M. B. Wilk. An analysis of variance test for normality (complete samples). *Biometrika*, 52(3/4):591–611, 1965. ISSN 00063444. URL http://www.jstor.org/stable/2333709. Last accessed on 2020-06-09.

[108] T. Spillane, N. Menaa, V. Atrashkevich, A. Bosko, F. Bronson, D. Nakazawa, W.R. Russ, and R. Venkataraman. An adaptive approach to mathematical efficiency calibration with uncertain source geometries. Proceedings of the American Nuclear Society Topical Meeting on Decommissioning, Decontamication and reutilization, August 2010, 2010.

[109] Michael G. Stabin, editor. *Interaction of Radiation with Matter*, pages 43–66. Springer New York, New York, NY, 2007. ISBN 978-0-387-49983-3. doi: 10.1007/978-0-387-49983-3_4. URL https://doi.org/10.1007/978-0-387-49983-3_4.

[110] A.H. Sullivan. *A guide to radiation and radioactivity levels near high energy particle accelerators*. 1992.

[111] F. Tecker. Longitudinal beam dynamics. Basics of Accelerator Science and Technology at CERN Chavannes de Bogis, 4-8 November 2013, 2013. URL https://indico.cern.ch/event/226938/contributions/478805/attachments/3

73732/519907/Longitudinal-Basic-2013-1-3.pdf. Last accessed on 2020-01-07.

[112] Lester G. Telser. The lognormal distribution, j. aitchison and j. a. c. brown, cambridge, england: Cambridge university press, 1957, pp. xviii, 176. $6.50. *American Journal of Agricultural Economics*, 41(1):161–162, 1959. doi: https://doi.org/10.2307/1235218. URL https://onlinelibrary.wiley.com/doi/abs/10.2307/1235218.

[113] Christian Theis and Helmut Vincke. The use of ActiWiz in operational radiation protection. In *Proceedings, 12th Meeting of Task-Force on Shielding Aspects of Accelerators, Targets and Irradiation Facilities (SATIF-12): Batavia, IL, USA, April 28-30, 2014*, pages 88–98, 8 2016.

[114] James Thomson and Simon Temple. Chapter 7 - sample preparation techniques for liquid scintillation analysis. In Michael F. L'Annunziata, editor, *Handbook of Radioactivity Analysis (Fourth Edition)*, pages 803–860. Academic Press, fourth edition edition, 2020. ISBN 978-0-12-814397-1. doi: https://doi.org/10.1016/B978-0-12-814397-1.00007-8. URL https://www.sciencedirect.com/science/article/pii/B9780128143971000078.

[115] H Vincke and C Theis. ActiWiz 3- an overview of the latest developments and their application. *J. Phys. : Conf. Ser.*, 1046(1):012007. 10 p, 2018. URL https://cds.cern.ch/record/2636327. Last accessed on 2020-01-15.

[116] Xiang Wan, Wenqian Wang, Jiming Liu, and Tiejun Tong. Estimating the sample mean and standard deviation from the sample size, median, range and/or interquartile range. *BMC medical research methodology*, 14, 12 2014. doi: 10.1186/1471-2288-14-135.

[117] B. L. Welch. The generalization of 'student's' problem when several different population variances are involved. *Biometrika*, 34(1/2):28–35, 1947. ISSN 00063444. URL http://www.jstor.org/stable/2332510.

[118] H. Wiedemann. *Particle Accelerator Physics*. Graduate Texts in Physics. Springer International Publishing, 2015. ISBN 9783319183166.

[119] R. Wigmans. *Calorimetry: Energy Measurement in Particle Physics*. International Series of Monographs on Physics. OUP Oxford, 2017. URL https://www.oxfordscholarship.com/view/10.1093/oso/9780198786351.001.0001/oso-9780198786351-chapter-2. Chapter 2. Last accessed on 2020-01-13.

[120] E. Wilson and E.J.N. Wilson. *An Introduction to Particle Accelerators*. An Introduction to Particle Accelerators. Oxford University Press, 2001. ISBN 019850829.

[121] B. Zaffora. Statistical analysis for the radiological characterization of radioactive waste in particle accelerators, Jul 2017. URL https://cds.cern.ch/record/2290521. Presented 08 Sep 2017.

[122] B. Zaffora, M. Magistris, G. Saporta, and J.-P. Chevalier. Uncertainty quantification applied to the radiological characterization of radioactive waste. *Applied Radiation and Isotopes*, 127:142 – 149, 2017. ISSN 0969-8043. doi: https://doi.org/10.1016/j.apradiso.2017.06.001. URL http://www.sciencedirect.com/science/article/pii/S0969804317300593.

[123] Biagio Zaffora, Severine Demeyer, Matteo Magistris, Elvezio Ronchetti, Gilbert Saporta, and Chris Theis. A bayesian framework to update scaling factors for radioactive waste characterization. *Applied Radiation and Isotopes*, 159:109092, 2020. ISSN 0969-8043. doi: https://doi.org/10.1016/j.apradiso.2020.109092. URL https://www.sciencedirect.com/science/article/pii/S0969804320300178.